1-1-2016

X-Ray Beam Characteristics And Radiation Dose Deposition To Soft Tissue From Fluoroscopic X-Ray Beams Incorporating Copper Filtration

Kevin Arthur Wunderle
Wayne State University,

Recommended Citation

Wunderle, Kevin Arthur, "X-Ray Beam Characteristics And Radiation Dose Deposition To Soft Tissue From Fluoroscopic X-Ray Beams Incorporating Copper Filtration" (2016). *Wayne State University Dissertations*. 1671.
http://digitalcommons.wayne.edu/oa_dissertations/1671

X-RAY BEAM CHARACTERISTICS AND RADIATION DOSE DEPOSITION TO SOFT TISSUE FROM FLUOROSCOPIC X-RAY BEAMS INCORPORATING COPPER FILTRATION

by

KEVIN A. WUNDERLE

DISSERTATION

Submitted to the Graduate School

of Wayne State University,

Detroit, Michigan

in partial fulfillment of the requirements

for the degree of

DOCTOR OF PHILOSOPHY

2016

MAJOR: MEDICAL PHYSICS

Approved By:

Advisor Date

DEDICATION

This work is dedicated to my loving family—my wife Rebecca, son Luke, and daughter Gwendolyn—for all of their support and sacrifice.

ACKNOWLEDGEMENTS

To my mentors—Drs. Frank Dong, Otto Muzik, William Davros and Pejavar Rao—my sincere gratitude for your guidance and friendship.

TABLE OF CONTENTS

LIST OF TABLES

LIST OF FIGURES

CHAPTER 1 INTRODUCTION

Within the classification of diagnostic imaging equipment, fluoroscopes stand alone in their broad application for diagnostic and therapeutic real-time image guidance. They provide temporally dynamic X-ray images used in a vast array of procedure types, including angiography (body, neurologic, cardiac), gastrointestinal and genitourinary diagnosis and therapy, intravascular oncologic therapies (bland embolization, chemoembolization, radioembolization), orthopedics, pain management, and bronchoscopy, to mention only a few.

Fluoroscope configurations vary widely based on their clinical application. This work focuses entirely on fluoroscopes used for image guidance during interventional procedures in which high radiation doses can be delivered to patients, doses sufficient to induce radiogenic tissue reactions. Generally, large C-arm type fluoroscopes are for fluoroscopically guided interventions (FGIs) (Figure 1-1.).

Figure 1-1. Example of a C-arm fluoroscope used for FGI procedures.

The following two sections of this chapter are excerpts from previous publications. The first, in section 1.1, describes fluoroscope components and operating parameters. It was previously published as part of a book chapter titled “Radiation safety in the cardiac catheterization laboratory” in *Cardiovascular Intervention: A Companion to Braunwald’s Heart Disease* edited by Deepak L. Bhatt.[1] The present author contributed substantially in the writing of the book chapter, and the first author and publisher granted permission to reproduce content from the book chapter in the present work. The second section, 1.2, describes background information and radiation dose terminology commonly encountered in reference to FGIs. The content in section 1.2 is from a first-authored paper entitled “Radiation-related injuries and their management: an update” published in Seminars in Interventional Radiology.[2] Permission from the publisher to reproduce content from the publication was granted. The purpose for including these sections in the current work is to provide background information regarding fluoroscopes and fluoroscopic terminology useful in understanding the context of the research performed and described in the subsequent chapters.

1.1 Fluoroscope components and function

A fluoroscope is an X-ray–generating device that provides real-time radiographic imaging. Fluoroscopic equipment in an interventional imaging suite characteristically consists of a large C-arm, X-ray tube, image receptor, generator, and operating console. The radiographic images are subsequently processed and displayed on a high-performance image display monitor.[3]

C-arm

A C-arm consists of an X-ray tube and image receptor affixed to opposite ends of the C-arm. The X-ray tube is mounted in a fixed orientation on the C-arm, typically positioned below the procedure table. The image receptor is mounted on a movable suspension above the table. This suspension permits the operator to raise or lower the image receptor in relation to the patient. The entire C-arm support system may be mounted directly on the floor, ceiling, or on a robotically controlled device.

Most C-arms are capable of rotation speeds of up to 35 degrees/s, and up to 100 degrees/s for CT angiography and rotational angiography. Movement of a C-arm is commonly limited by proximity sensors that slow or stop rotation at a certain distance from the patient or the X-ray table.

X-ray tube

The X-ray tube consists of an evacuated glass- or metal-enclosed assembly that contains a circular anode (positive electrode) and a cathode with one or more filaments (negative electrode). When an electric current is passed through the filament, its temperature increases and electrons are released through thermionic emission. These electrons are accelerated through a potential difference, focused on a small area of the anode known as the focal spot track. The X-rays produced have a heterogeneous energy distribution dependent on the anode material and tube voltage. Typically, less than 1% of the energy applied to an X-ray tube is converted into X-rays; the majority is lost to heat.

Management of this heat production is a major consideration in the design of X-ray tubes.

Characteristics of X-ray tube quantities include:

1. **mA (milliamperes):** the tube current, or the number of electrons traveling across the anode-cathode gap, per second. The X-ray output is linearly proportional to the tube current.
2. **Pulse width:** the duration of time that X-rays are used to create a single fluoroscopic image. A shorter pulse width can better capture an image of a moving object. The pulse width for cardiac angiographic procedures varies from approximately 6 to 10 ms. X-ray output is linearly proportional to pulse width.
3. **mAs (milliamperes*s):** measure of total charge, the product of the tube current (mA) and the pulse width (in seconds) for a given fluoroscopic image; linearly proportional to X-ray output.
4. **kVp (peak kilovoltage):** measure of voltage applied across the anode-cathode gap that characterizes the distribution of photon energies within an X-ray beam. Increasing the kVp increases the mean photon energy of an X-ray spectrum, resulting in a more penetrating beam. The tube voltage has a complex relationship to X-ray output, which can be approximated as a power $[(kVp1/kVp2)^2]$ relationship. For example, doubling the peak kilovoltage approximately quadruples the X-ray output.

5. **Focal spot:** a well-defined region on the anode where the accelerated electrons are focused and X-rays are produced. Most X-ray tubes have two or more focal spots, each paired with a dedicated cathode filament. The long dimension of the focal spot can vary from approximately 0.3 mm to 1.0 mm for cardiac angiographic systems. The limited heat capacity of the anode dictates that when the total heat deposited exceeds a certain threshold, the focal spot must change to a larger size to distribute the electrons over a cooler and larger area in order to prevent anode damage.
6. **X-ray filtration:** The X-ray beam passes through numerous materials before reaching the patient, including the tube with housing (glass/metal assembly, oil, exit port) and added spectral shaping filters (aluminum [Al] and/or copper [Cu] sheets) contained within the collimator. Modern systems allow for variable filtration that can be changed within a procedure or between protocols. This added filtration proportionally reduces the number of lower-energy photons, therefore increasing the average photon energy. This process is referred to as “beam hardening,” which can reduce skin exposure for a given detector dose.

Image receptor

Digital flat-panel image receptors have replaced the older image intensifier technology in virtually all modern interventional suites. The vast majority of these detectors use an amorphous silicon detector coupled to a two-dimensional thin-film transistor array. The physical size of the detector elements (pixels) ranges from 80 to 200 microns, or one-twelfth to one-fifth of a millimeter.

1. **Image receptor function:** Digital flat-panel image receptors convert X-ray energy into a digital signal via a process that converts the X-ray into light, which is then converted into an electric signal via photodiodes. The fluoroscopic image information is sampled, amplified, digitized, and processed before display.
2. **Automatic dose rate control:** In all fluoroscopy systems, the image receptor acts as the critical component of a feedback loop that regulates the output of X-rays (mA, kVp, pulse width, filtration, and focal spot size). Automatic dose rate control (ADRC) ensures that the dose to the detector is sufficient to provide adequate image quality, accounting for changes in patient size, thickness, and presence of highly attenuating structures. The ADRC increases output parameters to ensure that the image quality is similar to that of previously obtained images.

Operator console

Angiographers employ bedside controls to manipulate the C-arm, procedure table, field of view (FOV), magnification mode, and clinical protocol/techniques. A foot pedal is used to control the duration of X-ray exposure and the type of image that is desired (fluoroscopy/acquisition). The operating console in the nearby control room provides the interface between the operator and the imaging and patient monitoring systems. The console communicates with the image display system, the picture archiving and communication system, and the electronic medical record.

Image display monitor

Visualization of images on the overhead monitor is an integral part of all angiographic procedures. Monitors vary in size from 40 cm to 150 cm and should be routinely evaluated to ensure appropriate luminance, grayscale performance, contrast, resolution, spatial linearity, and absence of artifacts. Any issue that impairs the ability of the angiographer to evaluate fluoroscopic images may prolong the procedure and unnecessarily increase the radiation dose. It is not only the monitor that is important, but also the display environment, including the following variables:

1. **Distance:** The optimal viewing distance between the angiographer and the monitor is a factor of 1.5 to 2.0 of the diagonal. For instance, using a 48-cm display, this distance is about 1 meter, or approximately arm's length.
2. **Viewing conditions:** Bright lights within the angiographic suite increase the ambient light in the interventional suite, which decreases the ability of the angiographer to visualize differences in shades of gray. Also, glare and reflections from lighting near the operator have the potential to interfere with image evaluation.

Fluoroscopic imaging modes

Historically, the terms “fluoro” and “cine” have been used to denote two different modes of radiographic image observation and/or recording. “Fluoro” has been used to describe real-time observation of lower-dose radiographic temporal imaging without recording. “Cine” has been used to describe the recording of higher-dose and image quality radiographic temporal imaging. However, the term cine implies the use of motion picture film in the recording of the radiographically produced images. Modern systems no longer employ film; recording is exclusively digital and available for all operational modes, including fluoroscopy.

To minimize confusion, the following terms will be used:

1. **“Fluoro” (or “fluoroscopic observation”):** describes the real-time temporal imaging performed at or below radiation output limits established by regulatory agencies. Fluoro typically defaults to nonrecorded imaging; however, an operator can choose to save either a single fluoro image or an image sequence at the operator controls.
2. **“Acquisition”:** describes the mode of operation that requires recording of the real-time imaging, employing increased radiation output that is needed for high-quality images. This mode of imaging is not governed by regulatory limits and is limited only by hardware capability or by design parameters established by the vendor and not typically accessible to the end user without service support.

Within the fluoroscopic mode of operation, there are typically three radiation output/image quality levels selectable by the operator. These settings are customizable and can vary greatly among fluoroscopic units. Generally, there is a “low-dose” fluoro level that is nominally set at 50% of the “standard dose” and a “high-dose” level set at 200% of the standard dose. In the United States, federal regulations pertaining to manufacturers limit the radiation output for the fluoroscopic imaging modes under specific conditions. For the standard- and low-dose fluoroscopic imaging modes, the air kerma limit is 88 mGy/min (10 R/min in traditional units). The high-dose fluoro mode may, given certain additional requirements, extend the air kerma limit to 176 mGy/min (20 R/min exposure). For C-arm fluoroscopes, these limitations are defined at 30 cm from the face of the image receptor regardless of the source-to-image distance (SID). Again, the acquisition imaging mode of operation does not include regulatory radiation output limitations. Acquisition rates can range from approximately 10 to 3000 mGy/min and under most circumstances fall between 100 and 300 mGy/min.

Fluoroscopic image quality

The basic purpose of fluoroscopic imaging is to obtain adequate image quality in order to make a diagnosis or conduct an intervention. Reductions in radiation dose have the potential to decrease image quality. Therefore, we cannot institute broad measures to reduce radiation dose without taking into account the effects that these changes will have on image quality.[4] The following are key characteristics of fluoroscopic image quality:

1. **Spatial resolution:** the ability to differentiate fine detail within an image. The “limiting” spatial resolution is the smallest distance in space by which two objects can be separated and still appear distinct. This is important in cardiac angiography for the perception and delineation of small vessels, fine wires, and anatomical boundaries. Factors that can significantly influence the achievable spatial resolution include the focal spot size, geometric magnification, and presence of motion. Because the focal spot has a finite size, it causes the edges of objects to appear blurred within a projected image. This phenomenon, called a “penumbra,” is linearly proportional to the size of the focal spot. The penumbra is also influenced by the location of the imaged object relative to the tube and detector. As the geometric magnification increases (object moves closer to the source), the blur increases. An object moving within the duration of a single pulse width will also appear blurred; this is referred to as “motion blur.”
2. **Contrast resolution:** the ability of a system to resolve differences in signal intensity (pixel values), or shades of gray. Contrast resolution is important in cardiac angiography for detecting small differences in attenuation (eg, a contrast-filled artery overlying the spine or diaphragm). Contrast can be divided into three categories: subject, image receptor, and display. Subject contrast is dependent on the object being imaged (composition, size) and the X-ray beam quality

(kVp, filtration). Image receptor contrast is dependent on the type of image receptor and its response to radiation. Display contrast is influenced by ambient lighting, monitor brightness and linearity, matrix size, and bit depth. Typically, cardiovascular images are displayed in 256 shades of gray.

3. **Temporal resolution:** the ability to resolve two events separated in time. This is directly dependent on fluoroscopic pulse width and the time between pulses, as temporal resolution is assessed over multiple images. For instance, an acquisition acquired at 3 frames/s will have a temporal resolution ten times poorer than one acquired at 30 frames/s. This is irrespective of spatial resolution, which occurs within a pulse width and is assessed in a single image. To reduce noise and/or dose, frame averaging is often used at the cost of temporal resolution.
4. **Noise:** broadly defined as information contained within an image that is not useful or interferes with the clinical task. Typically, noise is divided into three main categories: quantum, detector, and anatomical noise.
    a. **Quantum noise:** The most familiar form of noise, quantum noise or “mottle” is an inherent property of X-ray imaging. This type of noise is proportional to the number of quanta (X-rays) used to form the image, and decreases as the dose to the detector is increased. The relationship between relative image

noise and detector dose is approximately a square-root function. To reduce the proportion of noise by a factor of two, the detector dose must be increased by a factor of four. Spatial and temporal filtering can be used to reduce quantum noise in an image; however, these methods may decrease spatial and temporal resolution.

b. **Detector noise:** Flat-panel detectors are not flawless, and they contain various nonuniformities. Unlike quantum noise, these nonuniformities are structured and random in nature. Structured noise is due to fixed nonuniformities in detector response resulting in sensitivity and linearity variations. Random noise includes electronic noise and sporadic noise from malfunctioning individual detector elements or electronics. Structured detector noise can be addressed through calibration and image processing.

c. **Anatomical noise:** Anatomical noise is radiographic information that is unimportant for the diagnostic or therapeutic task. In cardiac interventions, the most common form of anatomical noise is the presence of bony anatomy. At very high image receptor doses, anatomical noise dominates over quantum and detector noise.

d. **Subtraction angiography:** Subtraction angiography creates a special situation with respect to noise. The process of subtracting one image from another can significantly reduce anatomical noise and some forms of image receptor noise. However, subtraction angiography does not decrease quantum mottle, because this form of noise is randomly distributed in both images. This produces increased noise in the subtracted image if standard radiation doses are used. To maintain similar noise characteristics, subtracted images require an increased detector dose compared to unsubtracted images. This increase may be as much as 10 to 20 times the dose/frame of standard-dose acquisition images. Angiographers usually employ low frame rates with subtraction angiography to conserve radiation dose.

1.2 Overview of radiation dose from FGI procedures

Radiation is ubiquitous in its various forms throughout our environment (eg, microwaves, radio waves, light, heat) without causing significant hazard. However, ionizing radiation, which includes X-rays, presents a significant potential for detrimental biological effects. Ionizing radiation damages cellular DNA either directly (resulting in the ionization of a DNA molecule) or indirectly from chemical reactions involving radiation-generated free radicals.[5] In theory, damage to even a single cell could result in mutated DNA with retained mitotic capability, potentially leading to stochastic effects such as carcinogenesis. More extensive damage leading to large-scale cellular death may result in a reduction of tissue integrity or function, termed “tissue reactions” (formerly referred to as “deterministic effects”). Tissue reactions are defined by a threshold dose below which a reaction would not occur and above which a reaction increases in severity proportional to the increased dose. Stochastic effects, conversely, are based on the statistical probability of inducing an effect. They do not have an associated threshold, and increasing dose increases the probability of inducing an effect but not the severity.[6]

Numerous quantities are used to define radiation energy deposition and radiation dose (Table 1-1).[7] The primary quantity of interest for patients undergoing an FGI is the peak skin dose ($D_{skin,max}$), which best represents the potential for a tissue reaction. Unfortunately, $D_{skin,max}$ is not available on most modern fluoroscopic systems; the air kerma at the interventional reference plane ($K_{a,r}$) is generally provided and is commonly used as a surrogate for $D_{skin,max}$. However, $K_{a,r}$ can differ significantly from $D_{skin,max}$ for several reasons. Most fluoroscopic systems measure $K_{a,r}$ using an ionization chamber mounted on top of the X-ray collimator. The International Electrotechnical Commission (IEC)-allowable tolerance for this device is ±35%. An additional uncertainty of approximately ±35% arises from factors such as variations in the geometric orientation of the fluoroscope in relation to the patient, attenuation by the procedure table and pad, the tissue backscatter factor, and differences in the X-ray absorption characteristics of air and soft tissue, all of which affect $D_{skin,max}$ but are not accounted for in $K_{a,r}$.[8] Figure 1-2 illustrates the effect of variations in the geometric orientation of the fluoroscope with respect to the 2-dimensional dose distribution at the skin entrance for a fenestrated and branched endovascular repair. The film darkness correlates to radiation dose at each location and demonstrates the contribution of the discrete X-ray fields to $D_{skin,max}$. $K_{a,r}$ is not capable of differentiating among discrete X-ray fields; it is simply the integral of all exposures irrespective of their contribution to $D_{skin,max}$. Although $K_{a,r}$ is often used by clinicians as a surrogate for patient dose, it must be understood that this value likely differs substantially from $D_{skin,max}$.

Table 1-1. Radiation quantities with their associated units and definitions.

Radiation quantity	SI, traditional unit	Definition
Exposure (X)	Coulomb/kg (C/kg), roentgen (R)	The amount of charge liberated per unit mass of air
Absorbed dose (D)	Gray (Gy), radiation absorbed dose (rad)	The amount of energy absorbed per unit mass of the absorbing medium
Equivalent dose (H_T)	Sievert (Sv), roentgen equivalent man (rem)	The absorbed dose equivalent, accounting for the type of radiation: absorbed dose multiplied by a radiation weighting factor (W_R), accounting for differences in biologic effect per unit of absorbed dose. For photons and electrons, W_R is 1
Effective dose (H_E)	Sievert (Sv), roentgen equivalent man (rem)	A calculated quantity used to express and compare risk. $\sum_T (H_T x W_T)$, where W_T is the assigned tissue weighting factor representing the relative radiation sensitivity of that tissue. Current W_T values can be found in International Commission on Radiological Protection Report 103[7]
Air kerma	Gray (Gy)	The kinetic energy released in air; at photon energies used for diagnostic imaging, this quantity is very close to the absorbed dose in air
Air kerma at the interventional reference plane ($K_{a,r}$)	Gray (Gy)	The air kerma determined at the interventional reference plane, defined as 15 cm toward the X-ray tube from the isocenter of the fluoroscope c-arm gantry. This is the quantity displayed on most modern fluoroscopes
Peak skin dose ($D_{skin,max}$)	Gray (Gy)	The highest absorbed dose to the skin

Figure 1-2. Radiochromic film (14 inches × 17 inches) from a fenestrated and branched endovascular repair showing the 2-dimensional radiation dose distribution. Film darkness correlates to increased radiation dose.

Tissue reactions

For kilovoltage energy X-ray beams such as those used for fluoroscopic imaging, the maximum radiation dose resides at the skin surface, making the skin the primary organ of concern for tissue reactions.[9] Although uncommon in diagnostic and interventional radiology, tissue reactions are generally well understood, with a known temporal and symptomatic progression based on radiation dose (Table 1-2).[10] The X-ray beam skin entrance location is the primary area of concern; for most interventional radiology procedures, this area will reside on the patient's back. These reactions can affect dermal (including hair), subcutaneous, and muscle tissues, and have also been documented in cranial bone from neurointerventional procedures.[11]

Table 1-2. Skin reaction progression with dose.

Single irradiation peak skin dose	Predicted NCI skin reaction grade*	Approximate reaction latency			
		Prompt (hours to 2 weeks)	Early (2-8 weeks)	Mid (6-40 weeks)	Late (>40 weeks)
<2 Gy	Not applicable	No effect predicted			
2-5 Gy	1	Mild pruritus, transient erythema		No effect predicted	
5-10 Gy	1-2	Intense pruritus, transient erythema	Dyspigmentation (hyper or hypo, potentially permanent), edema, epilation, erythema		Dermal atrophy, telangiectasia
10-15 Gy	2-3		Dyspigmentation (hyper or hypo, potentially permanent), desquamation (wet or dry), edema, epilation, erythema, necrosis, ulceration		
>15 Gy	3-4 (surgical repair likely required)	Desquamation (wet or dry), edema, pruritus, transient erythema			Dermal atrophy, necrosis, telangiectasia, ulceration

*Based on the National Cancer Institute (NCI) Common Terminology Criteria for Adverse Events.[12]

The radiation doses and latency periods identified in Table 1-2 are approximate and do not represent rigid thresholds. Numerous factors may exacerbate these reactions, including patient-specific factors such as smoking, obesity, the presence of overlapping skin folds, poor nutrition, and pre-existing skin degradation in the irradiated area; genetic disorders such as ataxia telangiectasia, Gorlin syndrome, Fanconi anemia, Bloom syndrome, xeroderma pigmentosum, familial polyposis, Gardner syndrome, hereditary malignant melanoma, and dysplastic nevus syndrome; diseases such as scleroderma, systemic lupus erythematosus, rheumatoid arthritis, hyperthyroidism, and diabetes mellitus; and the concurrent use of certain drugs such as doxorubicin, tamoxifen, methotrexate, bleomycin, 5-fluorouracil, and actinomycin D.[13-15] The location of the irradiated skin is also important, with locations listed in order of decreasing radiation sensitivity: anterior surface of the neck, flexor surfaces of the extremities, the trunk, the back, extensor surfaces of the extremities, the scalp, and the palms of the hands and soles of the feet.[16] Patients with light-colored hair and skin are most sensitive to radiation. All of the potential factors indicated above complicate the prediction of a reaction based solely on an estimated $D_{skin,max}$.

Radiation recall, a tissue reaction precipitated by the presence of a catalyst drug potentially years after radiation exposure, has also been documented from an FGI irradiation,[17] indicating the need for review of patient medications should a suspected radiation-induced tissue reaction present in greater severity than expected or outside of the typical time course for expression.

1.3 Research overview, aim, and context

Although the skin is the primary organ of interest when considering radiogenic tissue reactions from FGIs, there are circumstances in which estimating the absorbed dose at depth may be necessary, including cases of patients requiring multiple FGIs (possible for complex procedures), cases of patients requiring FGI procedures in temporal proximity of either radionuclide or external beam radiation therapy, and cases requiring fetal dose estimation in pregnant patients undergoing FGIs. For these situations, there is currently inadequate knowledge to perform proper radiation dose estimations.

The present body of work is intended to address existing deficiencies preventing adequate radiation dosimetry in soft tissue from X-ray beam qualities encountered on state-of-the-art fluoroscopes. This effort is structured within the present thesis as follows:

1. Chapter 2 presents a manuscript titled “Approaches to interventional fluoroscopic dose curves,” published in the Journal of Applied Clinical Medical Physics (JACMP).[18] The article describes how various parameters affecting radiation dose rates and X-ray beam spectra are modulated with changing patient-equivalent thicknesses on several state-of-the-art fluoroscopes from multiple vendors. This chapter defines the typical and possible range of X-ray beam qualities that may be encountered clinically and the differences in approach to manipulating the X-ray beam qualities by the ADRC. This knowledge was used to guide the subsequent work that has a principal dependence on the X-ray beam quality.
2. Chapter 3 presents a manuscript titled “Effect of fluoroscopic X-ray beam spectrum on air-kerma measurement accuracy: implications for establishing correction coefficients on interventional fluoroscopes with KAP meters,” also published in the JACMP.[19] The article presents an investigation of the fluoroscope-reported $K_{a,r}$ accuracy over a broad

range of X-ray beam spectra (those defined using the knowledge discussed in chapter 2). Most fluoroscope manufactures measure $K_{a,r}$ using an ionization chamber integrated into the X-ray beam collimator. These ionization chambers are allowed an uncertainty of ±35% by regulatory bodies (IEC and the Food and Drug Administration [FDA]), which is impractical for dosimetry. This chapter investigates this uncertainty and evaluates a calibration process proposed by the American Association of Physicists in Medicine (AAPM) Task Group 190 (TG190) for a full range of X-ray beam qualities.

3. Chapter 4 presents a manuscript titled “Percent depth doses and X-ray beam characterizations for fluoroscopic X-ray beam spectra incorporating copper filtration,” submitted and currently under review for publication with the journal Medical Physics. The manuscript presents percent depth dose (PDD) curves and X-ray beam characteristics over a full range of X-ray beam qualities and X-ray field sizes. Using these PDDs, with the research presented in chapters 1 and 2, it is possible to estimate the dose in water at depth from X-ray beam spectra encountered on state-of-the-art fluoroscopes.
4. Chapter 5 presents the beginning of a manuscript from work in progress that investigates X-ray beam profiles at various depths in water across the full range of X-ray beam qualities and X-ray field sizes from a state-of-the-art interventional fluoroscope. An abstract

describing this work was published in Medical Physics.[20] This work is intended to address out-of-field radiation exposure at depth in soft tissue, such as that potentially encountered in fetal radiation exposures.

Collectively, these 4 chapters represent a cohesive body of work intended to address an existing lack of knowledge regarding fluoroscopic X-ray beam qualities and dose deposition from those X-ray beams. This work became necessary following the introduction of X-ray spectral filtration (primarily Cu) used during fluoroscopic imaging in the 1990s with broad, nearly universal adoption over the last 2 decades.[21] By design, spectral filters change the X-ray beam spectrum and hence the beam quality, substantially affecting the radiation dose deposition and distribution.

CHAPTER 2 APPROACHES TO INTERVENTIONAL FLUOROSCOPIC DOSE CURVES

2.1 Introduction

Modern fluoroscopes used for real-time, image-based guidance in interventional procedures are complex X-ray machines, with advanced image acquisition and processing systems capable of automatically controlling numerous parameters based on defined protocol settings.[22] Advances in X-ray generation have allowed for the production of nearly constant applied voltage and X-ray tubes capable of greater radiation output; this is evident with the newest generation of X-ray tubes used in interventional fluoroscopes from GE (Waukesha, WI) and Siemens (Erlangen, Germany), which have 100 kVp power ratings of up to 100 kW and 90 kW, respectively.[23] These advances in X-ray generation, combined with advances such as cone-beam computed tomography (CBCT) and 3D fluoroscopic road-mapping, have facilitated the expansion of the vascular interventional clinical repertoire to include diseases and disease states previously only treatable with surgery.[24] Although these FGI procedures are generally safer and offer outcomes similar to or better than their surgical alternatives, many are capable of inducing radiogenic tissue reactions.[24] To limit the risk of tissue reactions, other technological advances have been implemented and refined over the last 20 years, including pulsed only X-ray beams, ADRC, and variable Cu filtration to lower skin entrance dose and potentially preserve contrast by allowing for lower kVps.[21]

The purpose of this study was to evaluate and compare dose rate curves and approaches to technique factor modulation (controlled by the ADRC) in response to simulated patient thickness variations for several state-of-the-art fluoroscope models. The ADRC is the vendor-specific, software-based operational logic that controls the X-ray generation system and associated parameters, such as kVp, mA, ms, and Cu filtration thickness. In general, the goal of the ADRC is to maintain a specified radiation dose to the image receptor within regulatory or X-ray tube power limitations, based on the imaging protocol chosen by the operator. As stated by the AAPM Task Group 125 (TG125), knowledge of the operational logic driving ADRC for fluoroscopic systems is essential to assess whether the units are functioning properly; proper functioning affects both image quality and patient radiation dose.[25] Understanding how the fluoroscopic technique factors are modulated also provides knowledge of vendor-specific image acquisition approaches, which may provide insight into opportunities for optimization based on the clinical procedure's or operator's imaging requirements.

The operational logic of fluoroscopes incorporating ADRC has been investigated for various generations of fluoroscopic equipment over the last three decades.[21,22,25,26] Increases in computing power and speed have advanced these capabilities to include numerous parameters on the image acquisition and processing systems.[22] The AAPM TG125 report defined and summarized existing fluoroscopic data, and the current work attempts to add information regarding newer-generation fluoroscopic approaches to this knowledge base.

For the purpose of this study, imaging protocols shall refer to the selected examination set on the fluoroscope workstation that specifies the parameters used for X-ray generation and image processing. Vendor-default protocols were evaluated in this study, which generally represent a starting point for clinically used protocols. Imaging protocols should be optimized for the particular clinical task; procedures requiring high spatial resolution or visualization of subtle differences in contrast may necessitate higher radiation dose rates, whereas the clinical requirements for other procedures may allow for reduced radiation dose rates. Any modifications to the imaging protocols must be done in consultation with the clinical team and with a proficient understanding of the vendor-specific imaging protocols and parameters.

2.2 Materials and methods

Four state-of-the-art and one previous-generation interventional C-arm fluoroscopes (still on the market) from three manufacturers were evaluated, including a GE Discovery IGS 730 (Waukesha, WI), Philips Allura FD 20 with Clarity (Best, Netherlands), and Siemens Artis Q, Artis Q.zen and Artis Zee systems (Erlangen, Germany). All testing was performed using the vendors' default abdomen or body imaging protocols with the exception of the GE system, which does not provide default organ-based programs. GE offers the choice of several default dose curves that can be selected and applied to clinical protocols, affecting both the fluoroscopic and acquisition modes of imaging. For the GE unit, the dose curves chosen were the ones clinically used and representative of a probable default abdomen protocol.

All $\dot{K}_{a,r}$ (air kerma rate at the interventional reference point [IRP]) values reported in this study were determined and displayed by each of the fluoroscopes during irradiation. With the exception of the GE Discovery unit, all $\dot{K}_{a,r}$ values were measured by a kerma-area-product meter (KAP-meter) integrated into the fluoroscope assembly to monitor X-ray tube output. The GE Discovery used factory preprogrammed lookup tables (LUTs) based on the system geometry and technique factors to determine the KAP (the product of air kerma and the X-ray beam field size on the same plane as the measurement of the air kerma), $K_{a,r}$ (air kerma at the IRP), and $\dot{K}_{a,r}$. Accuracy of the displayed $K_{a,r}$ for all fluoroscopes was determined by comparing displayed values to measurements made with a calibrated Radcal Accu-Pro dosimeter (Monrovia, CA) with a Radcal 10 × 6-6 ionization chamber placed free-in-air at the IRP (the point [or plane] in space where the $K_{a,r}$ is calculated; the IEC definition is 15 cm toward the X-ray tube from the isocenter of the C-arm gantry; all fluoroscopes tested use this definition). Because the allowed deviation of the displayed $K_{a,r}$ and KAP, per the IEC and FDA, is ±35%, correction factors (CFs) were determined using the external ionization chamber as a reference. With lead in the beam, measurements were made to determine CFs (Table 2-1) for the fluoroscopic and acquisition modes of operation in the chosen imaging protocol, which were then applied to their respective data:

$$\boldsymbol{CF = \frac{K_{a,r,ex}}{K_{a,r,in}}}$$

where $K_{a,r,ex}$ is the cumulative air kerma at the IRP as measured with the external calibrated ionization chamber, and $K_{a,r,in}$ is the cumulative air kerma at the IRP as determined with the integrated KAP-meter or LUT.

For this study, all reported $\dot{K}_{a,r}$ values were those reported at the IRP for each fluoroscope. However, because of geometric differences among the fluoroscope gantries, the focal-spot-to-IRP distances, the floor-to-focal-spot distances, and the floor-to-IRP distances are different among the fluoroscopes evaluated (Table 2-2). However, if the assumption is made regarding fluoroscope geometry that most clinical imaging will be performed at an operator-preferred table height (floor-to-procedure-table height), these geometric differences result in a relatively small deviation in $\dot{K}_{a,r}$ when the procedure table is placed at the respective IRP. If the $\dot{K}_{a,r}$ from the largest floor-to-table height is adjusted to match that of the smallest floor-to-table height, the deviation is approximately 5% (see Appendix A for further explanation of this deviation). Therefore, the $\dot{K}_{a,r}$ from each fluoroscope was used without geometric normalizing.

Table 2-1. Calculated correction factors applied to the displayed air kerma rates.

Vendor make and model	CF for fluoroscopic mode	CF for acquisition mode
GE Discovery IGS	1.03	1.09
Philips Allura with Clarity	1.16	1.16
Siemens Artis Q	1.13	1.06
Siemens Artis Q.zen	1.03	1.09
Siemens Artis Zee	1.21	1.12

Table 2-2. IRP distances from focal spot.

Vendor make and model	IRP (cm distance from focal spot)	Floor-to-focal-spot distance (cm)	Measurement plane from floor (cm)
GE Discovery IGS	67	25	92
Philips Allura w/ Clarity	61.5	29.5	91
Siemens Artis Q	63.5	30.5	93.5
Siemens Artis Q.zen	60	30	90
Siemens Artis Zee	63.5	31	94.5

For each fluoroscope, with the table pad removed, the surface of the procedure table was placed at the respective IRP with 35.56 cm (14 inches) of polymethyl methacrylate (PMMA) placed on top. The image receptor was lowered as close as possible to the PMMA. The X-ray field of view closest to 40 cm was used for all measurements, with the manufacturers' standard antiscatter grid in place. The $\dot{K}_{a,r}$, X-ray tube potential (kVp), X-ray tube current (mA), and Cu filtration (mm Cu) were recorded for each PMMA thickness evaluated.

Measurements were made in the vendors' default abdomen or body protocols for 4-frames/s (fps) acquisition irradiation and 15-pulses/s (pps) fluoroscopic irradiations in the low-, normal- and high-dose modes, as applicable. This process was repeated for PMMA thicknesses ranging from 2.54 to 35.56 cm

(1-14 inches) in 2.54-cm (1-inch) increments, while maintaining the initial SID and object-to-image distance (OID).

2.3 Results

Figures 2-1 through 2-4 were generated with data from the vendors' default abdomen or body protocols in a 4-fps acquisition. Figure 2-1 illustrates $\dot{K}_{a,r}$ with respect to phantom thickness, with thicknesses ranging from 2.54 to 35.56 (1-14 inches). For this same acquisition protocol, variation of the X-ray tube potential with phantom thickness is shown in Figure 2-2, variation of tube current with phantom thickness is shown in Figure 2-3, and variation of the Cu filter thickness with phantom thickness is shown in Figure 2-4. Note that some vendors choose to report a time-averaged X-ray tube current, whereas others report a maximum instantaneous value; both are represented in the two-axes mA figures.

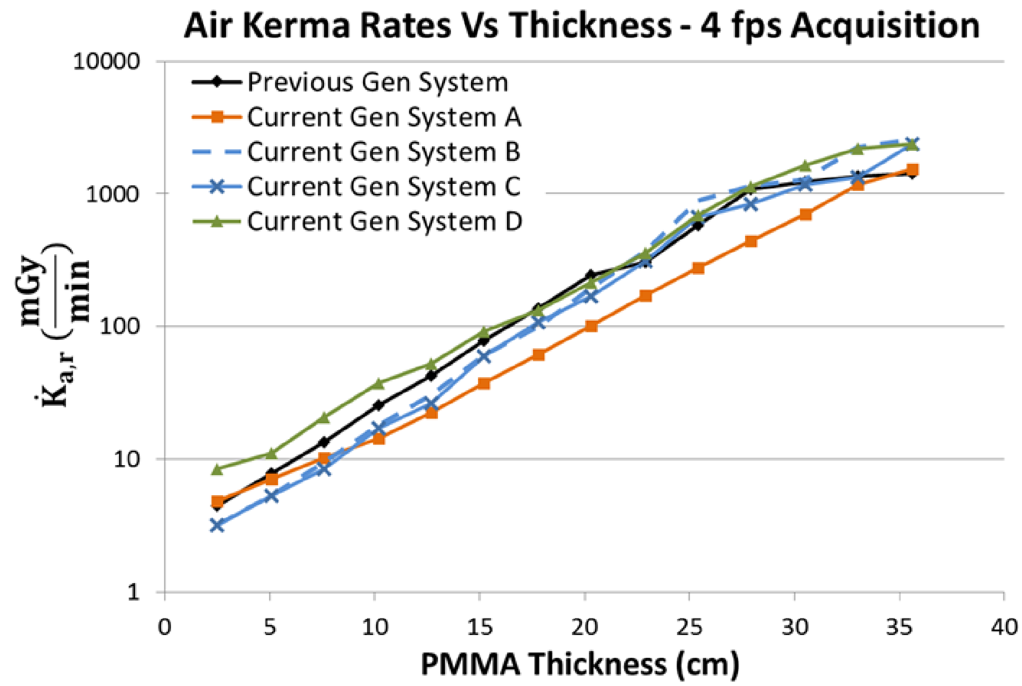

Figure 2-1. $\dot{\mathbf{K}}_{\mathbf{a,r}}$ versus PMMA phantom thickness for a 4-fps acquisition.

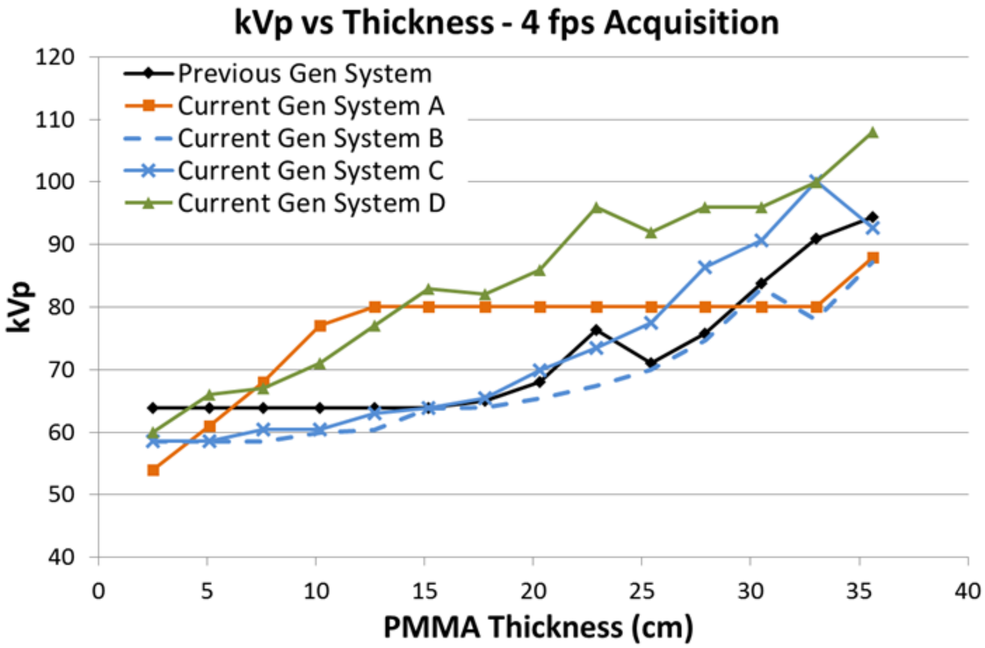

Figure 2-2. kVp versus PMMA phantom thickness for a 4-fps acquisition.

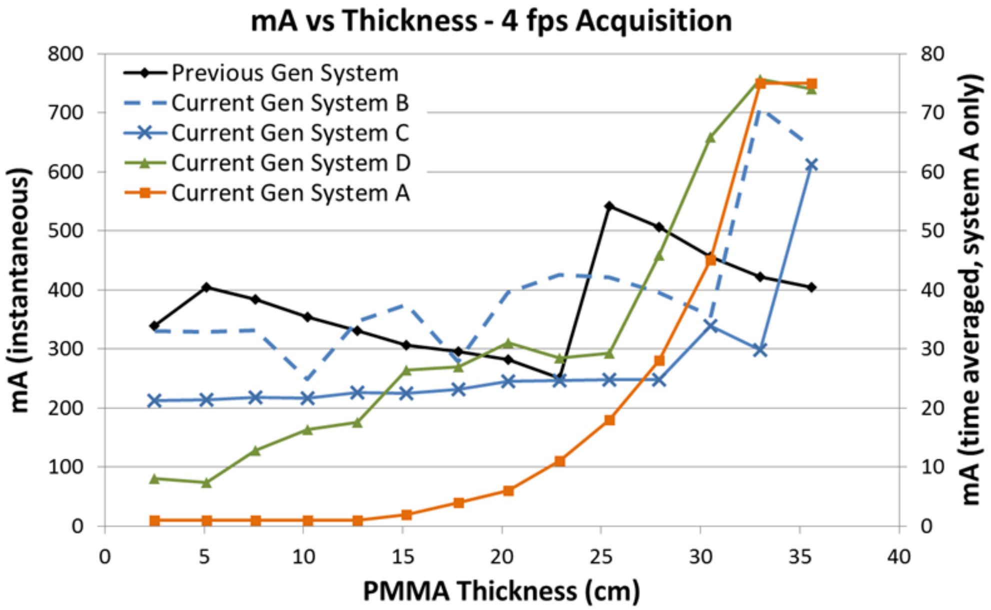

Figure 2-3. mA versus PMMA phantom thickness for a 4-fps acquisition.

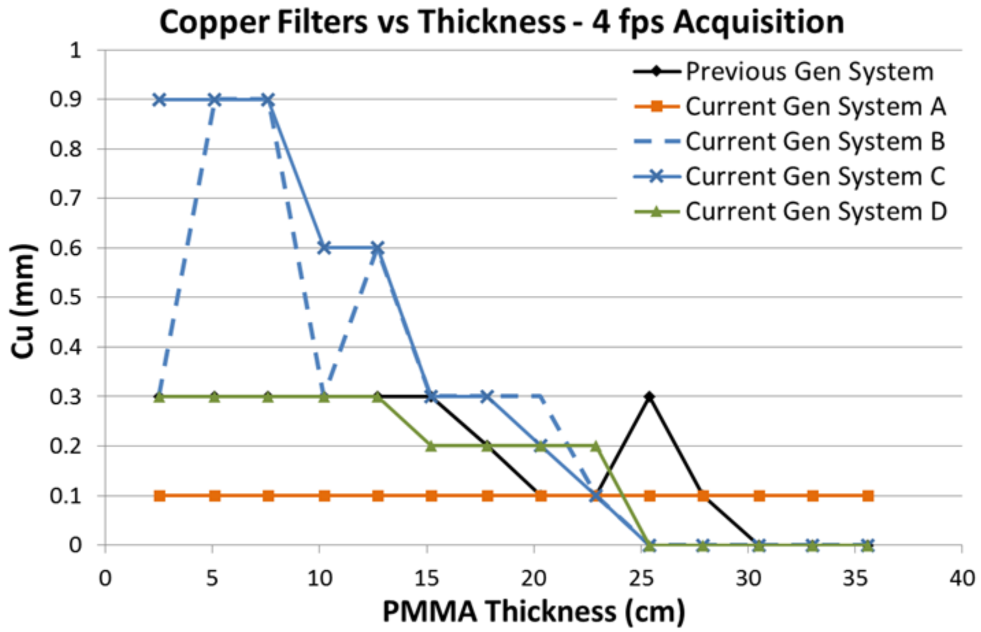

Figure 2-4. Cu thickness versus PMMA phantom thickness for a 4-fps acquisition.

Data used to generate Figures 2-5 through 2-8 were acquired with the vendors' default abdomen or body protocols in a 15-pps fluoroscopic low-dose mode. Figure 2-5 illustrates $\dot{K}_{a,r}$ with respect to phantom thickness, with thicknesses ranging from 2.54 to 35.56 cm. For this same fluoroscopic protocol, variation of the X-ray tube potential with phantom thickness is shown in Figure 2-6, variation of tube current with phantom thickness is shown in Figure 2-7, and variation of the Cu filter thickness with phantom thickness is shown in Figure 2-8.

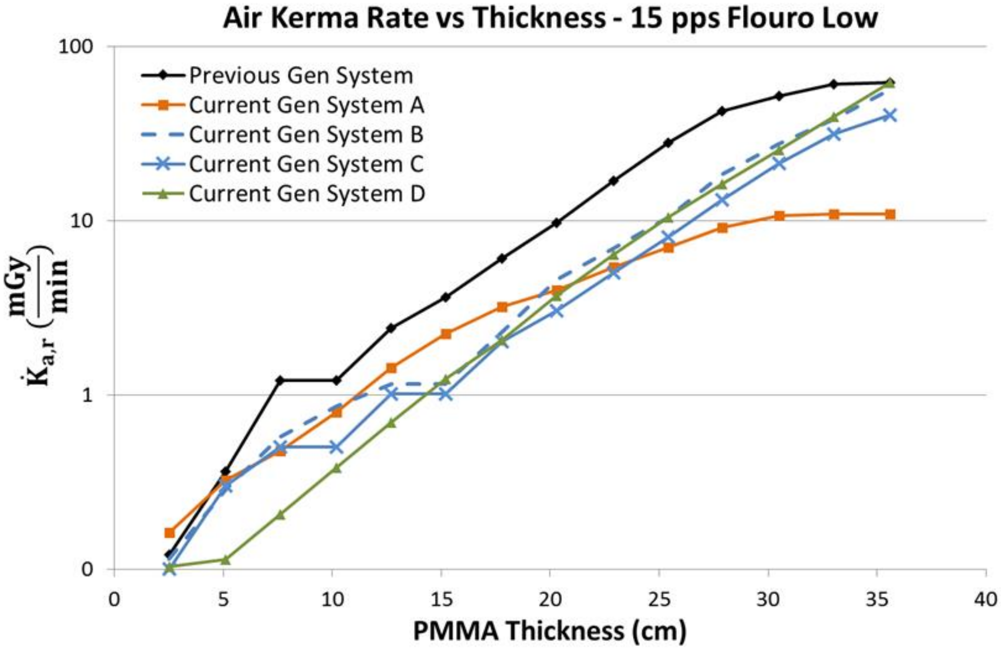

Figure 2-5. $\dot{\mathbf{K}}_{\mathbf{a,r}}$ versus PMMA phantom thickness in the fluoroscopic low-dose mode at 15 pps.

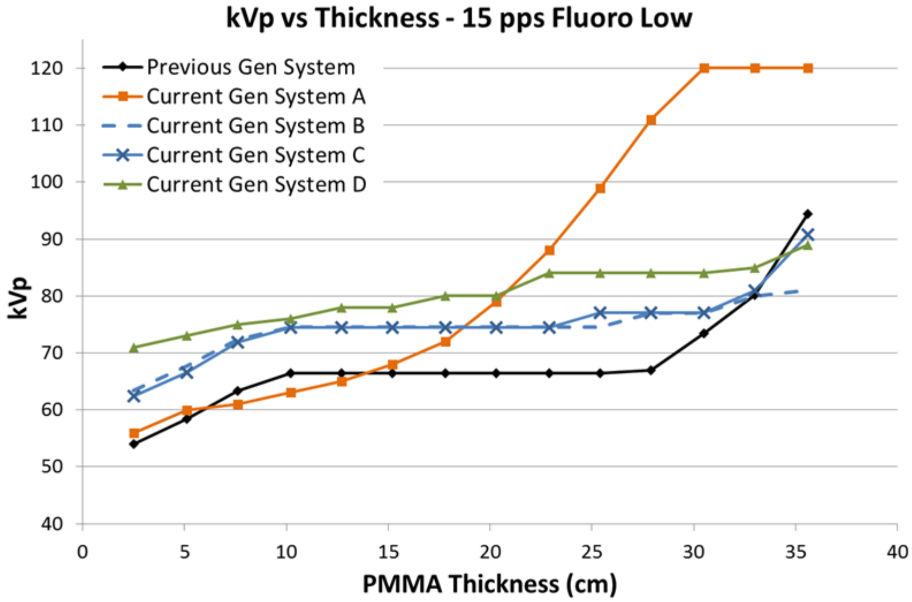

Figure 2-6. kVp versus PMMA phantom thickness in the fluoroscopic low-dose mode at 15 pps.

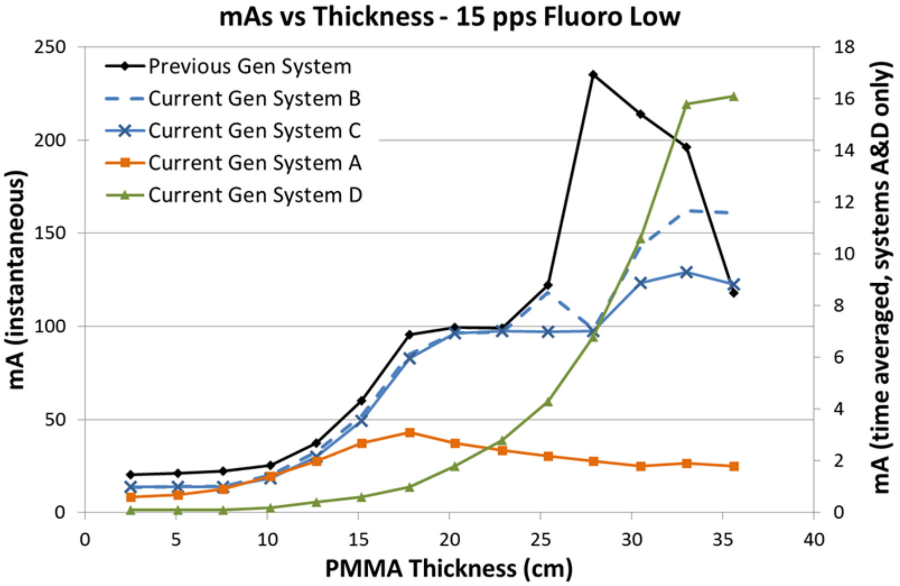

Figure 2-7. mA versus PMMA phantom thickness in the fluoroscopic low-dose mode at 15 pps.

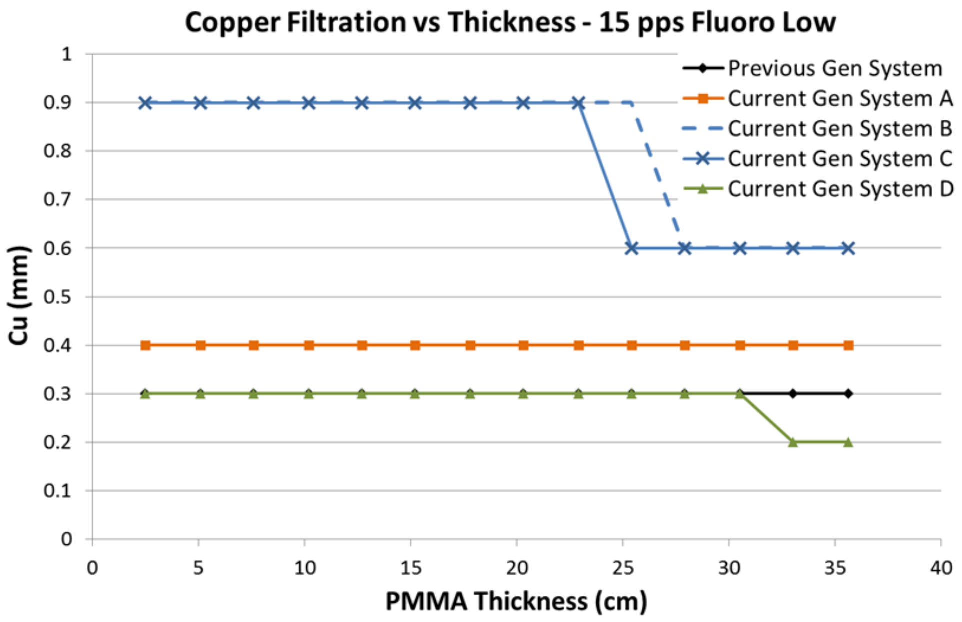

Figure 2-8. Cu thickness versus PMMA phantom thickness in the fluoroscopic low-dose mode at 15 pps.

Data used to generate Figures 2-9 through 2-12 were acquired with the vendors' default abdomen or body protocols in a 15-pps fluoroscopic normal-dose mode. Figure 2-9 illustrates $\dot{K}_{a,r}$ with respect to phantom thickness, with thicknesses ranging from 2.54 to 35.56 cm. For this same fluoroscopic protocol, variation of the X-ray tube potential with phantom thickness is shown in Figure 2-10, variation of the mA with phantom thickness is shown in Figure 2-11, and variation of the Cu filter thickness with phantom thickness is shown in Figure 2-12.

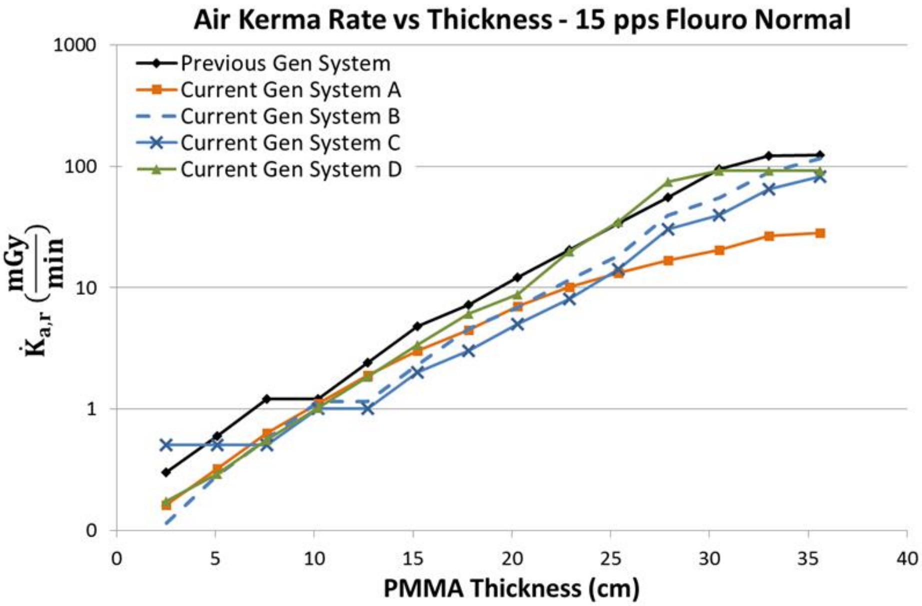

Figure 2-9. $\dot{\mathbf{K}}_{\mathbf{a,r}}$ versus PMMA phantom thickness in the fluoroscopic normal-dose mode at 15 pps.

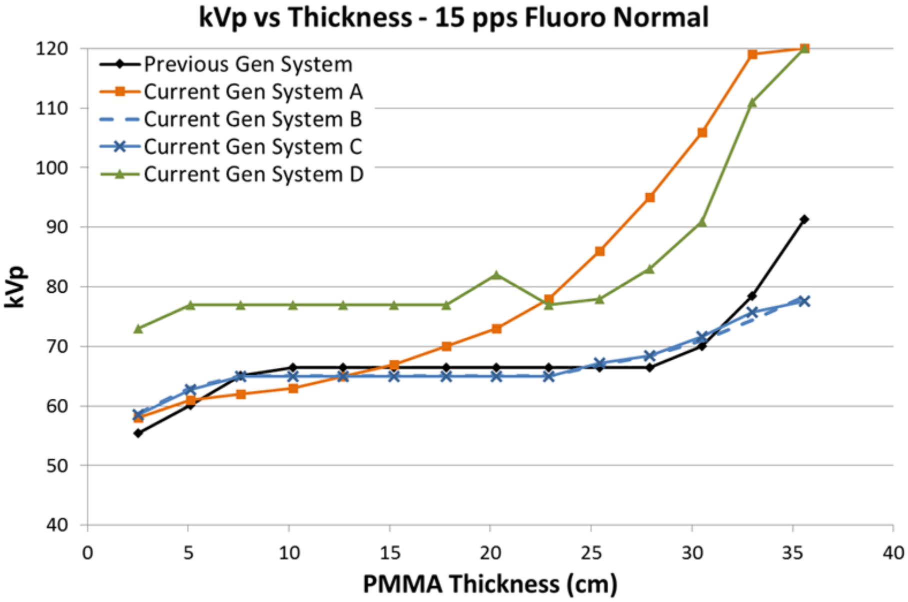

Figure 2-10. kVp versus PMMA phantom thickness in the fluoroscopic normal-dose mode at 15 pps.

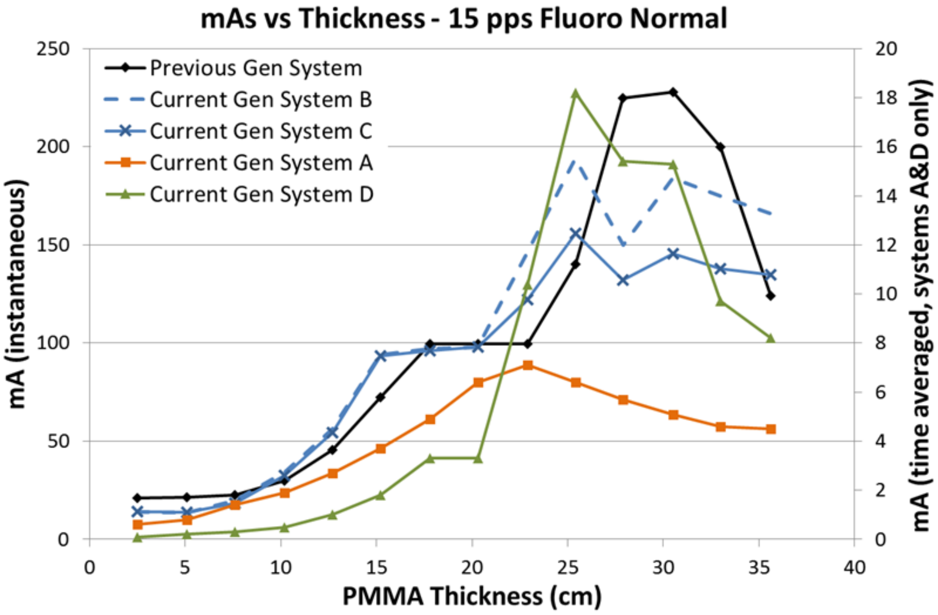

Figure 2-11. mA versus PMMA phantom thickness in the fluoroscopic normal-dose mode at 15 pps.

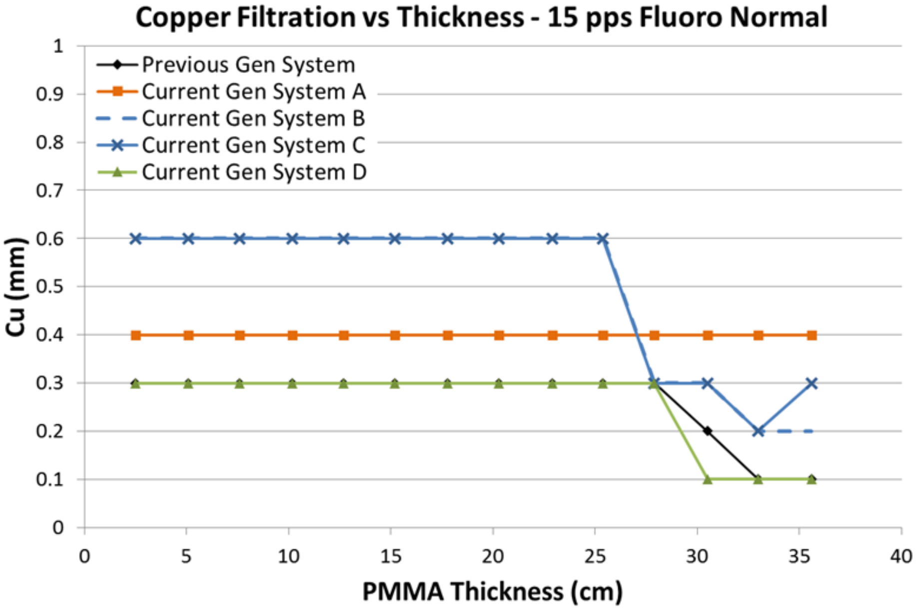

Figure 2-12. Cu thickness versus PMMA phantom thickness in the fluoroscopic normal-dose mode at 15 pps.

Data used to generate Figures 2-13 through 2-16 were acquired with the vendors' default abdomen or body protocols in a 15-pps fluoroscopic high-dose mode. Figure 2-13 illustrates $\dot{K}_{a,r}$ with respect to phantom thickness, with thicknesses ranging from 2.54 to 35.56. For this same fluoroscopic protocol, variation of the X-ray tube potential with phantom thickness is shown in Figure 2-14, variation of mA with phantom thickness is shown in Figure 2-15, and variation of the Cu filter thickness with phantom thickness is shown in Figure 2-16.

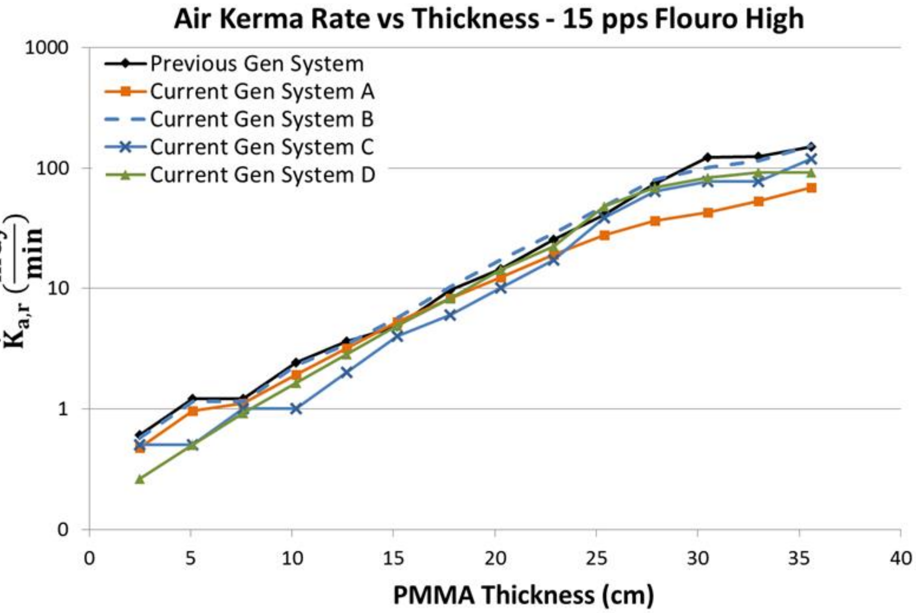

Figure 2-13. $\mathbf{\dot{K}_{a,r}}$ for PMMA phantom thickness in the fluoroscopic high-dose mode at 15 pps.

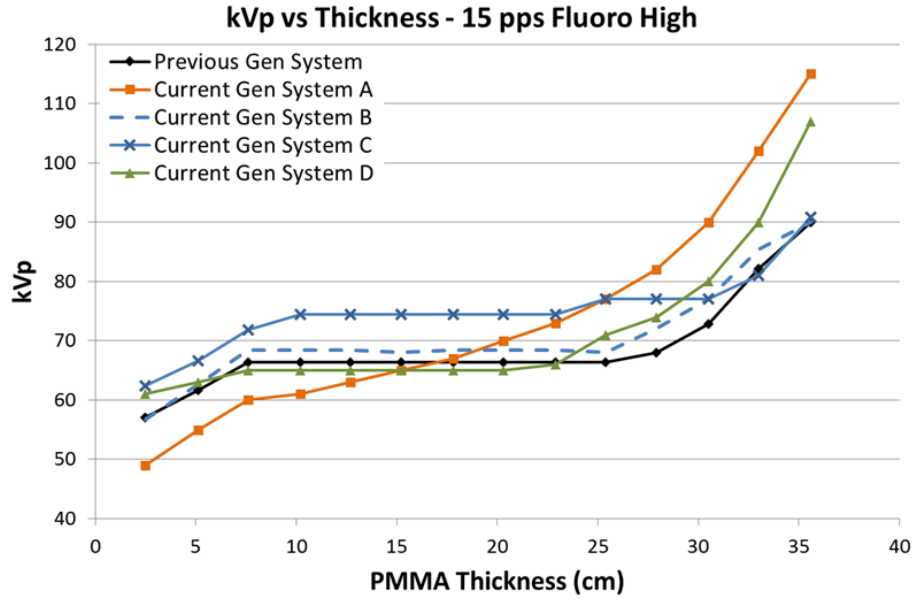

Figure 2-14. kVp versus PMMA phantom thickness in the fluoroscopic high-dose mode at 15 pps.

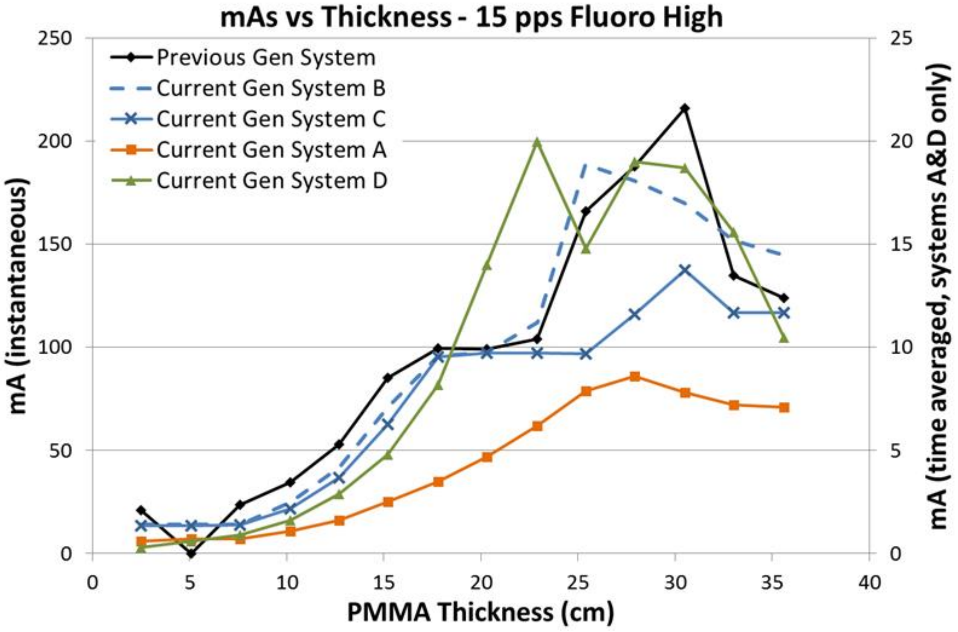

Figure 2-15. mA versus PMMA phantom thickness in the fluoroscopic high-dose mode at 15 pps.

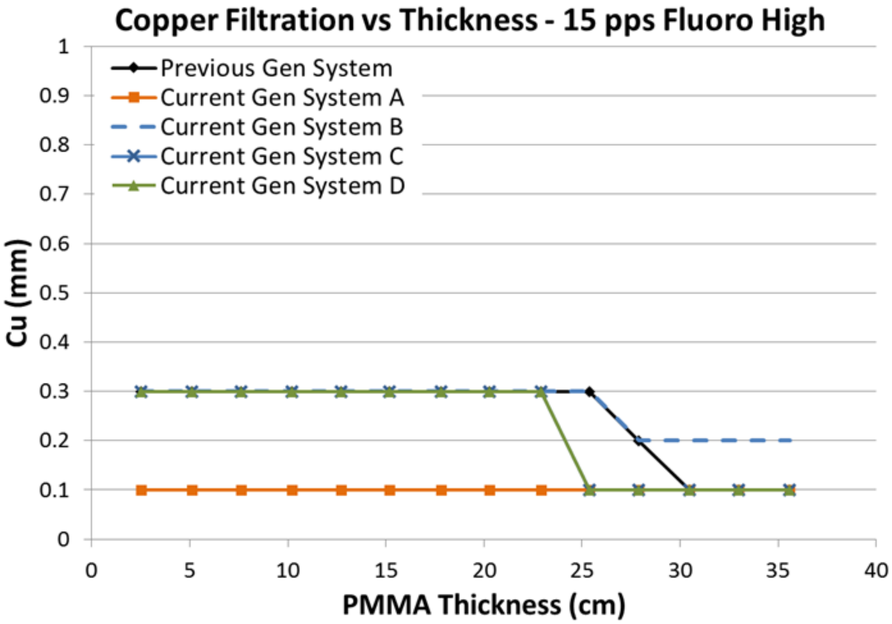

Figure 2-16. Cu thickness versus PMMA phantom thickness in the fluoroscopic high-dose mode at 15 pps.

2.4 Discussion

Air kerma rates $(\dot{K}_{a,r})$

All $\dot{K}_{a,r}$ values reported in this study were provided by the fluoroscope with a CF applied for accuracy that was determined by direct measurement with a calibrated ion chamber. The calibration factor was determined at a single beam quality with an ionization chamber that was calibrated for diagnostic energies. However, no calibration lab currently offers a calibration that covers the complete beam quality spectrum encountered on interventional fluoroscopes employing Cu filtration. The uncertainty in the CF, based on energy dependence, is approximately ±3% as reported by the ionization chamber manufacturer. As previously stated, there are also slight geometric differences between the fluoroscopes that result in an approximately 5% or less variation in the $\dot{K}_{a,r}$ due to the plane of measurement.

As evidenced in Figure 2-1, the radiation output capability for several of the current-generation systems has provided for potentially higher acquisition $\dot{K}_{a,r}$, exceeding 2.5 Gy/min for some systems. These $\dot{K}_{a,r}$ values, under certain circumstances, may be necessary for anatomic or procedural visualization, especially for complex procedures in morbidly obese patients. However, great caution must be used when allowing $\dot{K}_{a,r}$ to reach these levels, as tissue reactions could be triggered with only a few short acquisitions. There are currently no regulatory limits for the acquisition imaging mode; therefore, these $\dot{K}_{a,r}$ values are allowable. Fluoroscope operators and persons training those operators must understand that these substantial air kerma rates are possible and under what circumstances they may be realized.

As shown in Figures 2-2 through 2-5, the low-dose fluoroscopic mode of operation for all four of the newest-generation fluoroscopes yielded substantially lower $\dot{K}_{a,r}$ than the previous-generation unit evaluated. This is the imaging mode that fluoroscopes should default to, requiring operators to choose a higher dose-rate mode if needed. Figure 2-5 shows that system A has capped the $\dot{K}_{a,r}$ in this mode of operation at a level corresponding to 8.8 mGy/min (1 R/min) under standard testing geometry (ie, 30 cm from the image receptor with lead in the beam, which differs from the geometry of Figure 2-5). Although most vendors choose to cap the output in the low-dose fluoroscopic mode at approximately

50% of the allowable 88 mGy/min US limit (ie, 44 mGy/min at 30 cm from the image receptor), capping the output at 10% of the limit likely leads to operators prematurely transitioning to higher-dose rate fluoroscopic imaging modes. In Figure 2-5, the maximum $\dot{K}_{a,r}$ on system A was reached at approximately 30 cm of PMMA, and in that imaging mode, additional amounts of attenuation reduced the dose to the image receptor instead of increasing the X-ray output. If sufficient image quality can be achieved at further reduced image receptor doses, then a reduced image receptor dose should be employed throughout the curve to the maximum permissible exposure rate limit. Otherwise, allowing a reduced dose to the image receptor at such an artificially low cap may prematurely prompt an operator to choose a higher dose setting (with associated higher image receptor dose rates), defeating the benefit of the low-dose mode.

kVp modulation

In general, the current generation systems use higher kVps in the fluoroscopic and acquisition curves (Figures 2-2, 2-6, 2-10, 2-14) while maintaining Cu filtration thickness as compared to the previous-generation system. This results in higher beam quality and a reduced skin entrance dose for a given patient-fluoroscope geometry and image receptor dose, but could also adversely affect image contrast. System A increases kVp and reaches a maximum value more quickly than most of the other systems; however, this system also uses lower amounts of Cu filtration and does not dynamically change the filter thickness within a given protocol.

Tube current (mA) modulation

The modulation of the X-ray tube current is reported in different ways by the vendors. Time-averaged mA is reported by vendor A in the acquisition mode of imaging and by A and D in the fluoroscopic mode. Inflection points can be seen in the mA curves where the Cu filtration thicknesses change for the units that employ dynamic filters. In general, the mA curves tend toward higher values as phantom thickness increases, until a phantom thickness is used that drives the X-ray tube to approach its power limitations. At that point, the ADRC must decrease the mA for the higher kVp values, which is evident in all of the mA curves in Figures 2-2 through 2-15 for the high-dose fluoroscopic curve.

Use of Cu filters

The use of Cu X-ray beam filters was ubiquitous among the vendors evaluated, although all of the manufacturers have different approaches to how the filters are employed. Two vendors offer up to 0.9 mm of Cu filtration; however, for the testing performed, only one vendor employed that amount during fluoroscopic imaging. The use of 0.9 mm of Cu occurred at low kVps, suggesting that the greatest benefit is likely limited to pediatric FGI procedures. All but one system had a dynamic approach to changing the Cu filtration within a given imaging protocol; this one system used a static filtration thickness determined by the chosen imaging protocol. All of the current-generation systems have transitioned to using Cu filters during acquisition imaging, something not typically seen on older-generation systems. The inclusion of Cu allows for a substantial reduction in skin entrance dose during acquisitions, which is the imaging mode that delivers the highest fractional radiation dose for many FGI procedures.

Fluoroscopic operational characteristics: a team approach

The overall approach to imaging protocol optimization and the logic determining when to transition to higher dose imaging modes must be considered so that the end user can be presented with a full spectrum of dose rates (and image quality) optimized to the clinical task. To achieve this goal, all parties involved must diligently work together. Clinicians must understand the complexity of state-of-the-art equipment and that optimizing an imaging protocol necessitates identifying the lowest image quality possible to successfully complete a clinical task; high image quality is not always necessary and comes at the cost of radiation dose to the patient and occupational dose to the clinical team. Physicists must understand the vendor-specific approaches to the imaging protocol parameters and the ways in which they can be manipulated to achieve a clinically optimized imaging protocol. Equipment vendors must be forthright regarding the parameters they use for image acquisition and processing and how those parameters may be modified to achieve a desired change in radiation dose rate or image quality, something currently lacking from most vendors.

CHAPTER 3 EFFECT OF FLUOROSCOPIC X-RAY BEAM SPECTRUM ON AIR KERMA MEASUREMENT ACCURACY: IMPLICATIONS FOR ESTABLISHING CORRECTION COEFFICIENTS ON INTERVENTIONAL FLUOROSCOPES WITH KAP-METERS

3.1 Introduction

The allowable tolerance for the displayed reference plane air kerma ($K_{a,r}$) or air-kerma-area-product ($P_{k,a}$) on interventional C-arm fluoroscopes is ±35% per IEC and FDA requirements.[27] Large deviations in the accuracy of the displayed air kerma are therefore possible, even for properly functioning calibrated fluoroscopic systems. Inaccuracies of this magnitude are untenable for the purposes of estimating patient radiation dose or establishing and comparing clinical procedure reference dose levels, as suggested by the National Council on Radiation Protection and Measurements in Report 168.[28,29] The International Commission on Radiation Units and Measurements (ICRU) has recommended that uncertainty should be within 7% for radiation dose quantities in diagnostic imaging, a seemingly impossible task without correcting for the allowed deviations in the accuracy of the displayed $K_{a,r}$.[30]

The accuracy and variability of stand-alone air KAP-meters have been investigated by various groups since these meters came into common use a couple of decades ago.[31-34] Toroi et al investigated the response of various standalone KAP-meters over a range of X-ray beam qualities, varying both the kVp and filtration.[34] The results indicated that the correction coefficients (CCs) decrease as a function of increasing kVp from 40 kVp through 90 kVp; beyond that, the coefficient response was generally flat. The coefficients also decreased with increasing beam hardness (larger amounts of filtration) at a given kVp. These reports suggest that the standalone KAP-meters evaluated generally have a higher response (lower calibration coefficient) as the beam quality is increased. However, these investigations were performed on standalone KAP-meters that functioned independently of the fluoroscopic systems. Over the last decade, KAP-meters have been integrated into the fluoroscopic assembly, with their measurements displayed alongside other fluoroscopic technical parameters. How these measurements are integrated and the effect of no longer maintaining a fully independent measuring system have not been investigated.

Additionally, the AAPM established TG190 to define a protocol for determining and implementing CCs for a wide variety of X-ray equipment, including C-arm fluoroscopes used for interventional procedures. The TG190 report, titled "Accuracy and Calibration of Integrated Radiation Output Indicators in Diagnostic Radiology: A Report of the AAPM Imaging Physics Committee Task Group 190," provides standardized protocols including system geometry and recommended fluoroscope settings for determining a CC.[35] Specifically for C-arm fluoroscopes used for interventional procedures, TG 190 recommends:

1. Free-in-air geometry
2. Measurement by an external dosimeter situated at the isocenter of the C-arm
3. Testing of acquisition and fluoroscopy modes within a routine clinical examination set

4. 100 ± 10 kVp as the reference kVp
5. Maximum SID

For the present study, there were 2 primary purposes. The first was to determine the accuracy of the displayed $K_{a,r}$ or $P_{k,a}$ over a broad spectrum of X-ray beam qualities on clinically used interventional fluoroscopes with integrated KAP-meters to measure X-ray output. The second purpose was to investigate the accuracy of using a CC determined at a single beam quality and applying that CC to a broad spectrum of beam qualities, as suggested by TG190.

3.2 Materials and methods

This investigation was limited to interventional C-arm fluoroscopes using KAP-meters (also known as DAP-meters, AKAP-meters, or diamentors) to measure $P_{k,a}$ and/or $K_{a,r}$. Eleven state-of-the-art interventional fluoroscopes were evaluated, including Siemens (Erlangen, Germany) Artis Zee and Artis Q systems and Philips (Best, Netherlands) Allura FD systems. All units evaluated were fixed C-arm type fluoroscopes with flat-panel digital image receptors. A Radcal (Monrovia, CA) Accupro dosimeter with calibrated Radcal 10 × 6-60 (60 cc) ionization chamber (external chamber) was used to evaluate the accuracy of the KAP-meter. The C-arm was positioned with the X-ray tube near the floor and the image receptor above, the typical orientation for posteroanterior projections with a supine patient. No objects (including the procedure table and pad) were in the path of the X-ray beam; the IEC standard for the indicated air kerma or air-kerma-area-product of these fluoroscopes specifies free-in-air geometry without the procedure table present. The external chamber was mounted off the end of the procedure table, at or near the isocenter of the C-arm, with an SID of 100 cm or greater (Figure 3-1). A lead plate was used to cover and protect the image receptor during irradiation, but this plate was located sufficiently far away from the external chamber to prevent scatter radiation from affecting the measurements. A radiopaque ruler was used to measure the linear dimensions of a collimated square X-ray field, which was set to approximately 10 × 10 cm in the plane of the external chamber.

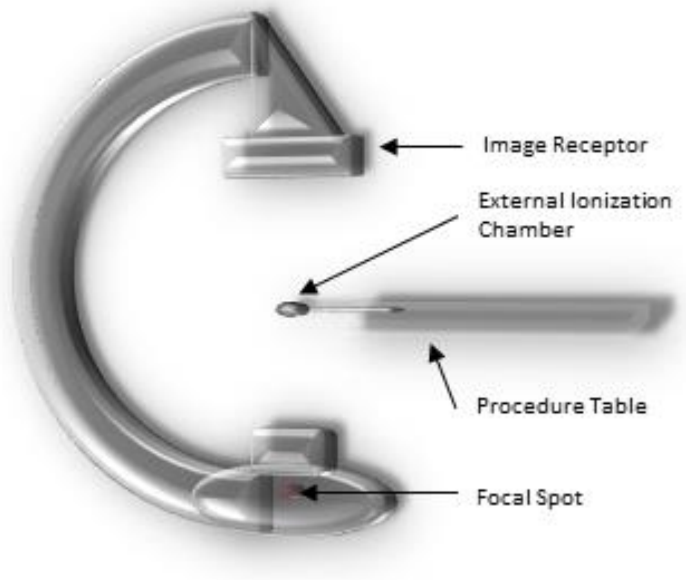

Figure 3-1. Setup for C-arm and external ionization chamber.

On each fluoroscopic system, 3 measurements were made at each available spectral filter (Cu) thickness for kVps ranging from 55 through 125 in 10-kVp increments and at 100 kVp (the TG190 reference kVp). To accomplish this, the vendor service mode (Siemens) or service assistance (Philips) was required to set fixed radiographic techniques. The $P_{k,a}$ measured by the KAP-meter and the incident air kerma ($K_{a,i}$) measured by the external chamber were recorded for each exposure. The $K_{a,i}$ measurements from the external chamber were multiplied by the X-ray beam area, yielding a $P_{k,a,ex}$ that was divided by the $P_{k,a}$ measured by the KAP-meter, providing a CC:

$$\boldsymbol{CC = \frac{K_{a,i} * A}{P_{k,a}}}$$

where $K_{a,i}$ is the incident air kerma measured by the external ion chamber, A is the area of the X-ray beam in the plane of the external ion chamber, and $P_{k,a}$ is the air-kerma-area-product reported by the fluoroscope.

In addition to CCs, normalized correction coefficients (NCCs) were determined by taking the CCs at each beam quality and normalizing them to one of the CCs determined at 100 kVp (the TG190 reference kVp) with different filtration thicknesses:

$$\boldsymbol{NCC_{100,0}(i,j) = \frac{CC_{i,j}}{CC_{100,0}}}$$

$$\boldsymbol{NCC_{100,0.1}(i,j) = \frac{CC_{i,j}}{CC_{100,0.1}}}$$

$$\boldsymbol{NCC_{100,0.9}(i,j) = \frac{CC_{i,j}}{CC_{100,0.9}}}$$

where i and j represent the kVp and Cu filtration thickness (mm), respectively. The NCCs provide an estimated deviation for using the 100 kVp CC instead of the CC at each specific beam quality.

3.3 Results

Figures 3-2 and 3-3 show the average CCs for each of the vendors at each beam quality. The reported values should not be used for any quantitative or clinical application; they are provided strictly to portray the trend of the CCs at each kVp as filtration is increased. There was significant intersystem variability in the CCs; Figure 3-4 shows this variability for the 8 Siemens systems at 55 kVp. However, as illustrated by the error bars in Figure 3-4, the intrasystem variability of the 3 measurements made at each beam quality was very small, and the trend of CCs for each vendor with increasing beam quality was consistent. Although not shown, the Philips systems exhibited similar inter- and intrasystem variability.

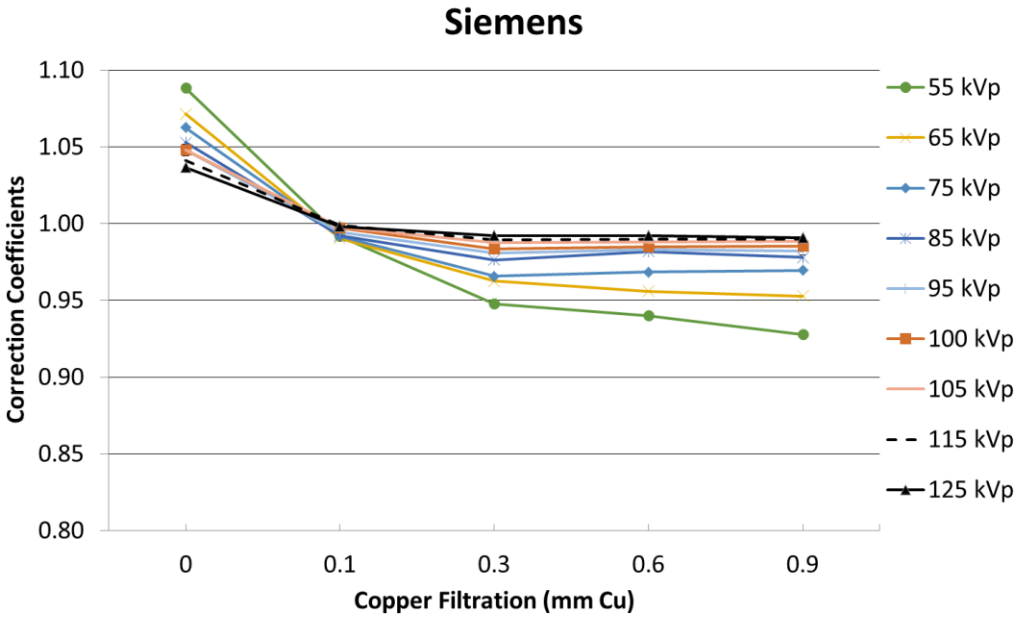

Figure 3-2. Averaged CCs for the Siemens units.

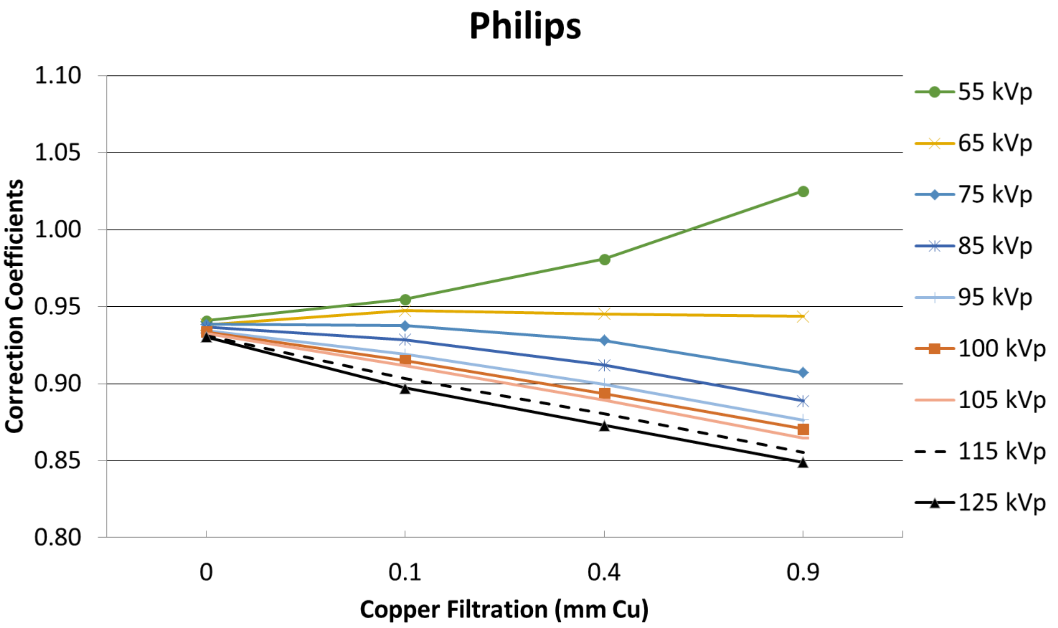

Figure 3-3. Averaged CCs for the Philips units.

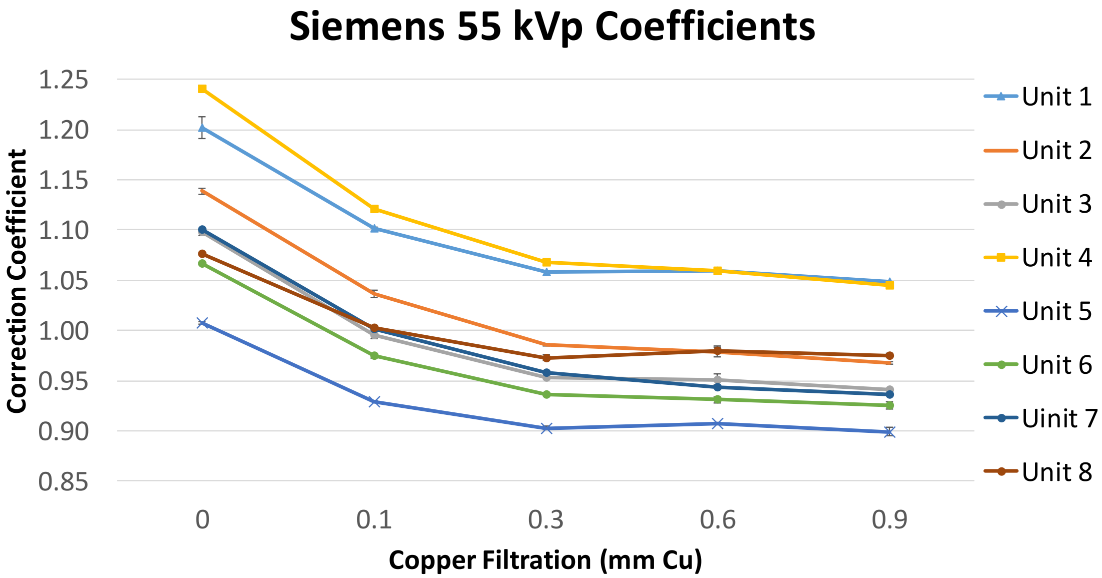

Figure 3-4. CCs at 55 kVp for the Siemens units.

Figures 3-5 and 3-6 illustrate the CC at each beam quality normalized to the CC at 100 kVp without additional filtration ($NCC_{100,0}$[i,j]) for Siemens and

Philips, respectively. Figures 3-7 and 3-8 illustrate the CC at each beam quality normalized to the CC at 100 kVp with 0.1 mm of additional filtration ($NCC_{100,0.1}[i,j]$). Figures 3-9 and 3-10 illustrate the CC at each beam quality normalized to the CC at 100 kVp with 0.9 mm of Cu filtration ($NCC_{100,0.9}[i,j]$).

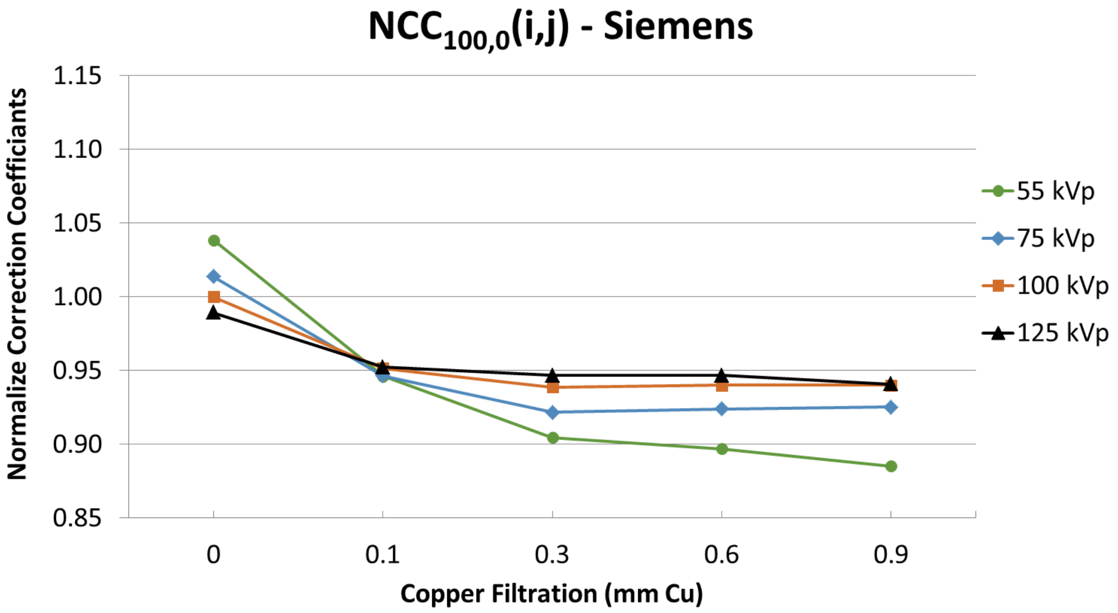

Figure 3-5. NCCs for the Siemens units, normalized to the CC at 100 kVp with no filtration.

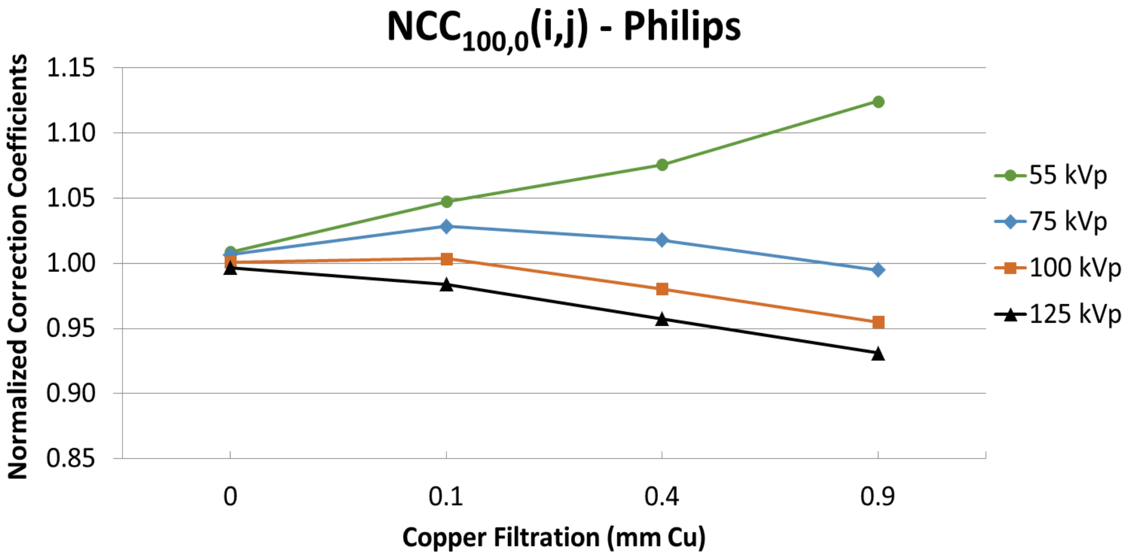

Figure 3-6. NCCs for the Philips units, normalized to the CC at 100 kVp with no filtration.

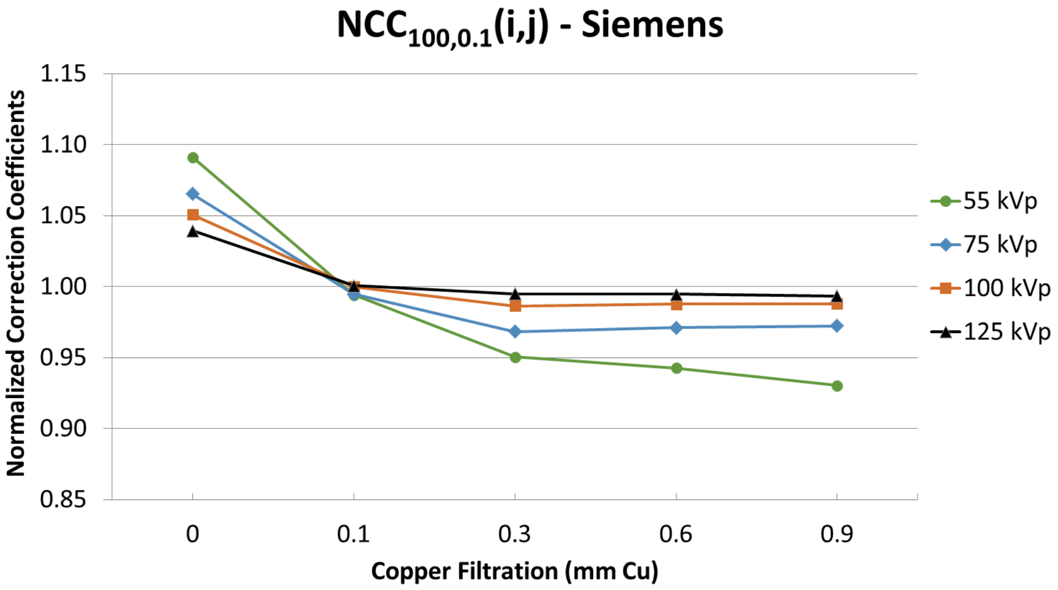

Figure 3-7. NCCs for the Siemens units, normalized to the CC at 100 kVp with 0.1 mm of filtration.

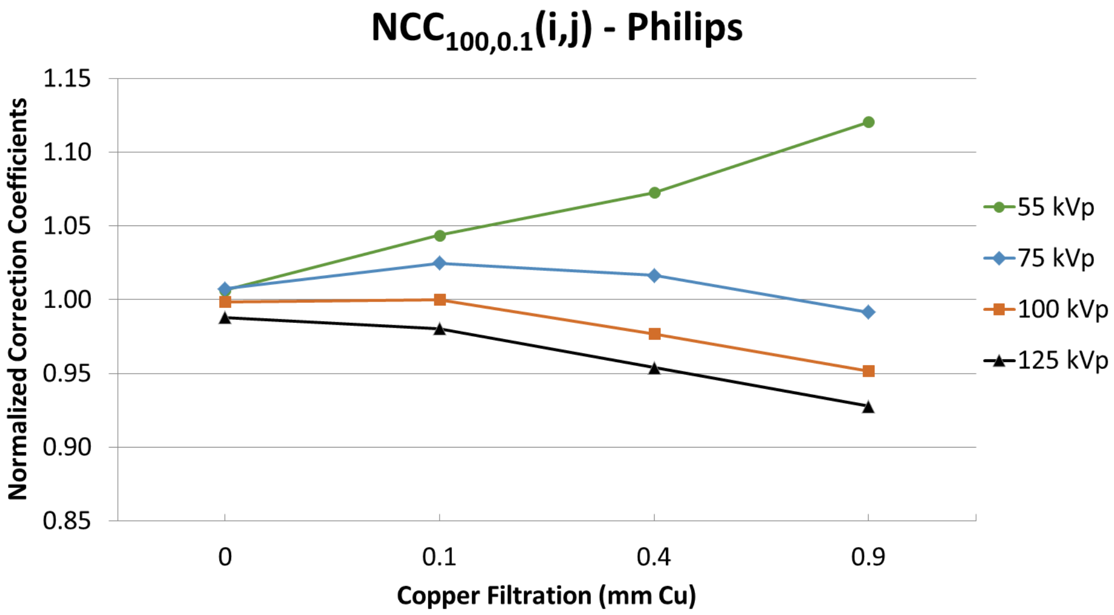

Figure 3-8. NCCs for the Philips units, normalized to the CC at 100 kVp with 0.1 mm of filtration.

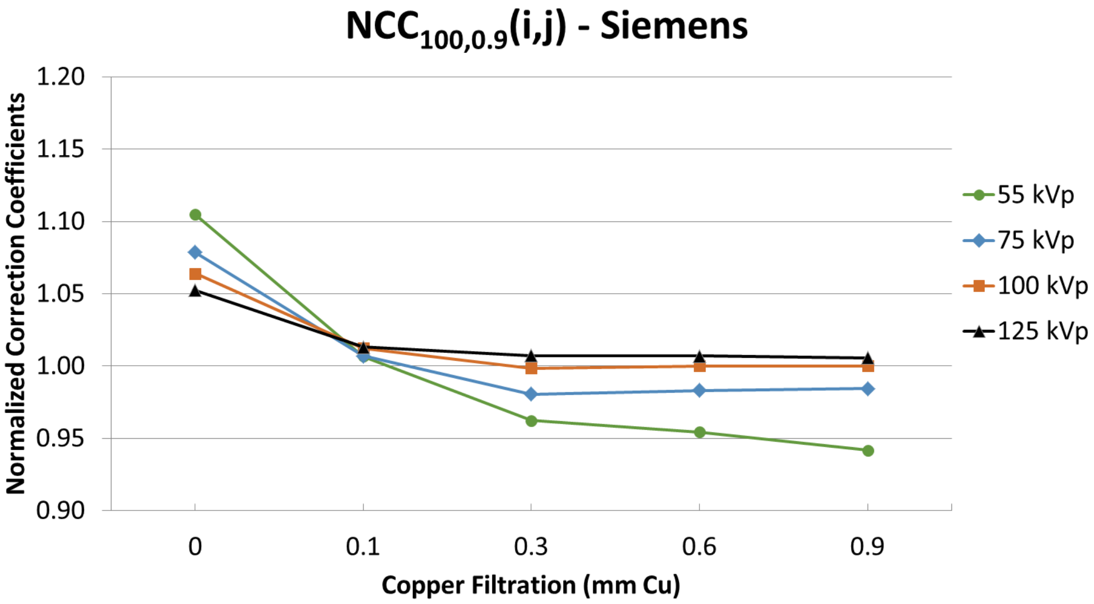

Figure 3-9. NCCs for the Siemens units, normalized to the CC at 100 kVp with 0.9 mm of filtration.

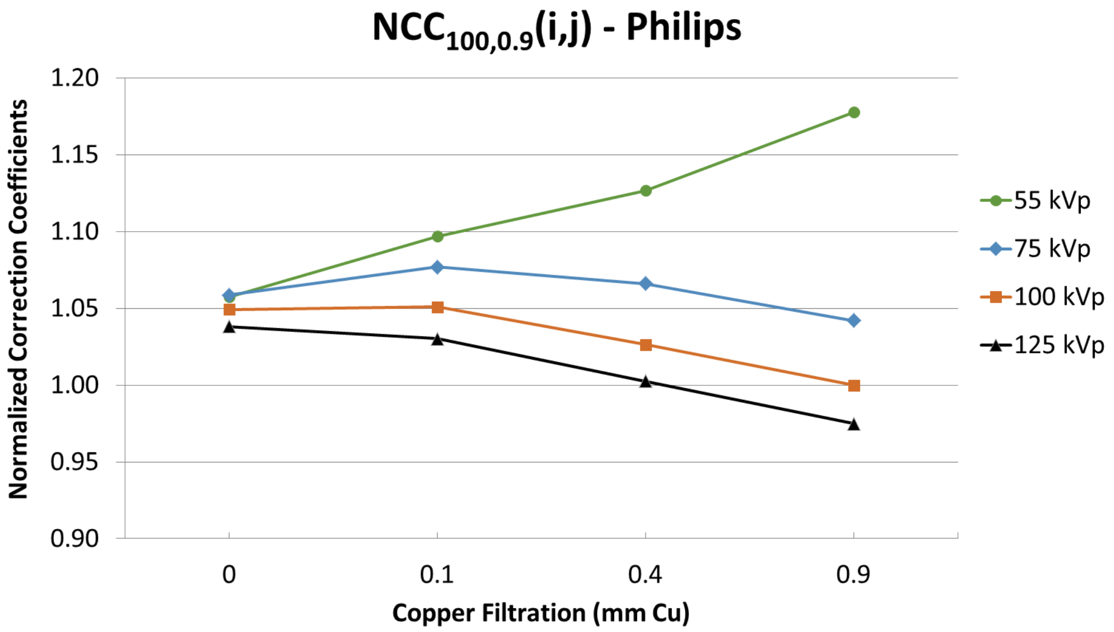

Figure 3-10. NCCs for the Philips units, normalized to the CC at 100 kVp with 0.9 mm of filtration.

3.4 Discussion

A primary goal of this study was to investigate the accuracy of applying a CC determined at a single beam quality, such as that established by AAPM TG190, to a broad spectrum of beam qualities on interventional C-arm fluoroscopes. In this regard, two primary conclusions can be drawn from the data acquired. First, for typical adult beam qualities, applying a single CC determined at 100 kVp with Cu in the beam results in a deviation of less than 5% due to beam quality variation. Figures 3-11 and 3-12 illustrate the $NCC_{100,0.1}(i,j)$ for a typical range of beam qualities used during adult fluoroscopic imaging (65-105 kVp; 0.1-0.6 mm of Cu). This indicates that applying a CC determined using the

TG190 (or similar) protocol provides very good accuracy as compared to the allowed ±35% deviation of the KAP-meter in this limited beam quality range.

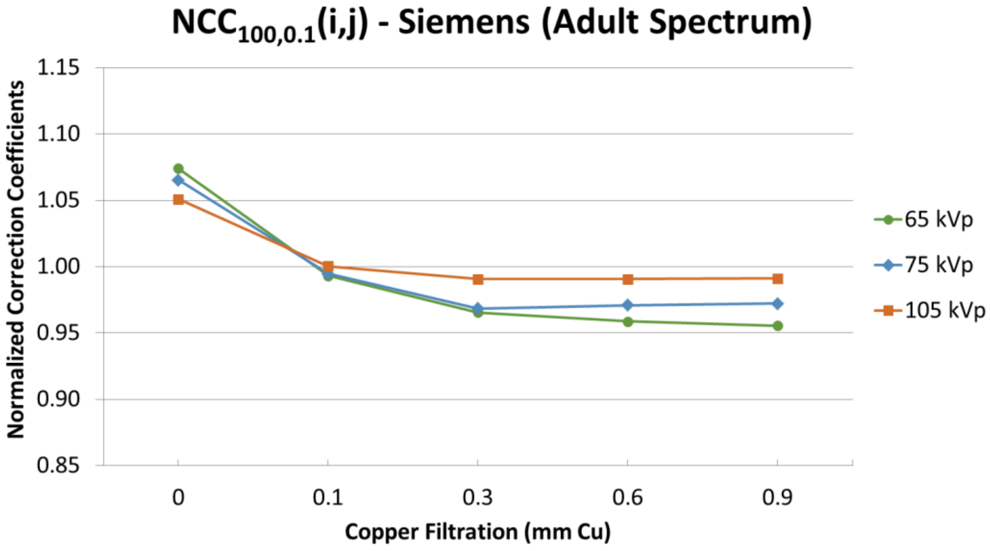

Figure 3-11. NCCs for the Siemens units over a typical beam quality range for adult fluoroscopic imaging, normalized to the CC at 100 kVp with 0.1 mm of filtration.

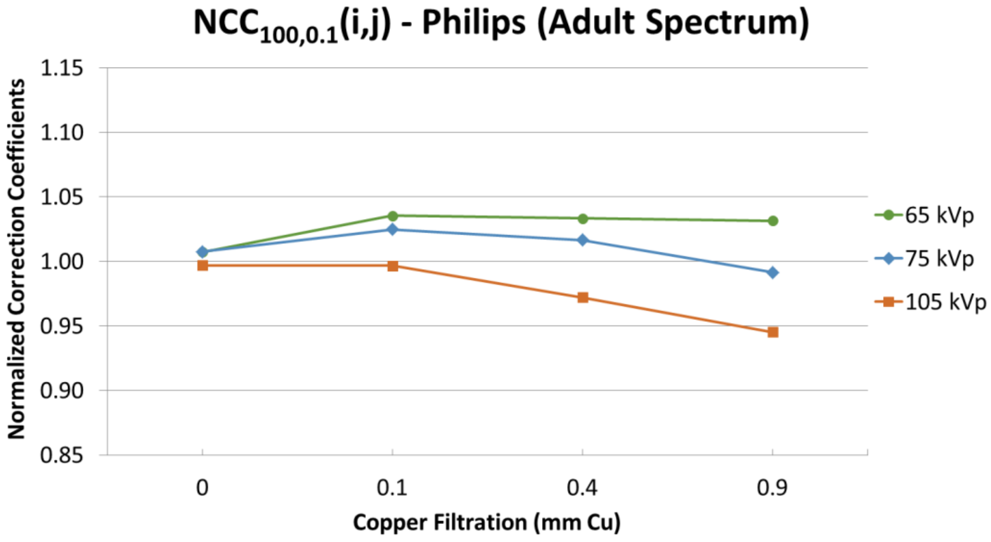

Figure 3-12. NCCs for the Philips units over a typical beam quality range for adult fluoroscopic imaging, normalized to the CC at 100 kVp with 0.1 mm of filtration.

Secondly, for pediatric interventions in children without an adult body habitus, typical beam qualities incorporate low kVp values (~55 kVp) and large amounts of spectral filtration (0.4-0.9 mm of Cu). Figures 3-8 and 3-9 indicate that for these beam qualities, the $NCC_{100,0.1}(i,j)$ deviates an average of 7% and 12% for the Siemens and Philips units, respectively. For interventional fluoroscopes dedicated to or routinely performing pediatric interventions, using a CC established with a low kVp (~55-60 kVp) and large amount of Cu filtration (~0.6-0.9 mm) may result in better accuracy as compared to using a CC determined at 100 kVp.

The stark difference in CCs for the 2 vendors (Figures 3-2 and 3-3) is surprising, as the KAP-meters used by Siemens and Philips for the fluoroscopes evaluated were manufactured by the same vendor, PTW (Freiburg, Germany). In fact, the change in CCs with increasing beam quality (for beam qualities incorporating Cu) was inverse between Philips and Siemens. For the Philips systems, the CCs decreased with increasing beam quality (similar to previous reports),[34] whereas for the Siemens systems, the CCs increased with increasing beam quality. The Philips and Siemens systems exhibited a convergence of the CCs at a given beam quality, something not reported by others who have investigated standalone KAP-meter responses.[31-34] These results indicate that the fluoroscope vendors are likely normalizing or otherwise influencing the KAP-meter output data. Even if the purpose is to increase the accuracy of the reported radiation quantities, modification of the KAP-meter measurements presents opportunities for large isolated deviations, which could easily go undetected. The authors have seen, in unrelated fluoroscope testing, a fluoroscope on which an individual protocol setting resulted in a deviation of approximately 80% compared to all other settings (deviation only occurred during a 30-pps acquisition, and no other setting produced a similar magnitude of error); this appeared to be a LUT-based error and was only discovered by chance. Modification of the KAP-meter data by the fluoroscope vendor allows for potentially large discrete errors to occur, and these errors may be nearly impossible for the end-user or clinical physicist to identify. Vendors should clearly state what correction factors are being applied to the KAP-meter (or provide access to view the LUTs) so that erroneous values may be identified more readily.

The use of a single CC across a wide spectrum of beam qualities can be successfully achieved, greatly improving the accuracy of the displayed $K_{a,r}$ as compared to the ±35% deviation allowed by regulations. The CCs are necessary for calculating peak skin dose estimates or for determining and comparing procedure reference dose levels. Without accounting for these deviations, it should be assumed that there is significant variability in the procedure $K_{a,r}$ or $P_{k,a}$. The AAPM TG190 protocol should be widely adopted and included as part of all fluoroscope acceptance and annual testing, with the resultant CCs included in all fluoroscopic testing reports.

CHAPTER 4 X-RAY BEAM CHARACTERIZATION AND AN APPROACH TO SOFT-TISSUE DOSE ESTIMATION FOR FLUOROSCOPIC X-RAY BEAM QUALITIES INCORPORATING COPPER FILTRATION

4.1 Introduction

FGIs, a class of clinical procedures typically performed in interventional radiology (body and neurology), cardiology (catheterization and electrophysiology), and vascular surgery departments, have grown in number and complexity over the last few decades.[9,10,24,29] On occasion, these interventions (either single procedures or multiple procedures over a relatively short period of time) can deliver radiation doses capable of inducing tissue reactions.[9,10,24,29] Although the skin is typically considered the primary organ at risk for diagnostic energy X-ray beams such as those used in FGIs, radiation doses to other organs may need to be considered. For instance, when FGIs are performed in pregnant patients, the radiation dose to the fetus should be estimated after the procedure.

One approach to obtaining the radiation dose at depth in tissue is to use PDD charts, which provide the fractional dose delivered at depth in water (soft tissue) relative to the depth of the maximum dose, which, at diagnostic energies, is typically at the X-ray beam entrance surface.[30,36-39] PDDs rely on several technical parameters, including a principal dependence on the X-ray beam quality. Most of the existing PDD data for diagnostic energy X-ray beams are decades old; the most recent published PDD data specific to fluoroscopic X-ray beams were reported by Fetterly et al in 2001.[37,40] However, many advances have been made in fluoroscope technology over the last few decades, and these advances substantially affect the X-ray beam qualities used during FGIs. In particular, fluoroscopic X-ray beam qualities from many current-generation interventional fluoroscopes apply Cu filtration in both the fluoroscopic and acquisition modes of imaging.[18,26] These X-ray beam qualities are very different from previous-generation fluoroscopic systems that did not include Cu filtration. Furthermore, in 2006, the FDA increased the required minimum half-value layer (HVL) for X-ray beams used by radiographic and fluoroscopic X-ray machines.[41] These changes have affected the X-ray beam qualities and the PDDs associated with them, requiring research into X-ray beam characterizations and PDDs for these modernized X-ray beam qualities.

The aim of this study was to investigate the X-ray beam qualities of first HVL, second HVL, homogeneity coefficients (HCs), backscatter factors (BSFs), and PDDs across a wide range of beam qualities from a state-of-the-art fluoroscope using Cu filtration. There are three intended applications of the results from this study. First, these results can be used to determine organ or point doses in soft tissue from high-dose FGIs, in which tissue reactions at depth may be of concern. This is primarily limited to adult interventions within the chest, abdomen, and pelvis. Secondly, the results can be used in fetal dose estimates from interventional procedures required in pregnant patients. Thirdly, our results can be compared to Monte Carlo simulations or other dose-modeling applications for their validation.

4.2 Materials and methods

Two separate sets of data were collected as part of this study, each with different materials and methods. First, X-ray beam characterization parameters of HVLs, HCs, and BSFs data were acquired to characterize the X-ray beam qualities used throughout the study. Second, central axis PDD data were acquired to define the dose at depth in soft tissue for the characterized X-ray beam qualities.

All measurements were acquired on a Siemens (Erlangen, Germany) Artis ZeeGo interventional C-arm fluoroscope. The fluoroscope was operated in the service mode for manual control of X-ray tube kVp, Cu filtration thickness, and mAs or mA depending on the mode of operation (radiographic vs fluoroscopic), which differed between the X-ray beam characterization measurements (HVLs and BSFs) and PDD measurements, respectively. All measurements were acquired using the large focal spot of the X-ray tube, which was required for the output necessary to measure second HVLs and PDDs at depth to 150 mm.

Fluoroscopic X-ray beam characterization

Fluoroscopic X-ray beam characteristics including kVp accuracy and precision, first HVLs, second HVLs, and HCs were determined using a calibrated Radcal (Monrovia, CA) AccuPro dosimeter with a 40 × 12-W diagnostic kV sensor for the kVp measurements and a 10 × 6-6 ionization chamber for air kerma measurements. To ensure proper calibration of the X-ray generator, the kVp accuracy and precision were determined from three repeated measurements each at 60, 80, 100, and 120 kVp without Cu filtration. For the HVL measurements, the ionization chamber was secured to the procedure table such that the active area of the chamber extended well beyond the end of the table and was centered in the X-ray beam free-in-air. The procedure table was elevated, placing the center of the ionization chamber at 72 cm from the focal spot (3 cm below the isocenter of the C-arm gantry), with a SID of 120 cm. The collimators were introduced to limit the X-ray field size to approximately 5 cm × 5 cm in the measurement plane of the ionization chamber. Air kerma was measured with varying amounts of type-1100 Al filters in the X-ray beam, ranging from 0 (no external Al filter) to within 0.5 mm below and above the first and second HVLs. The Al sheets were placed on top of the collimator housing, which was located approximately 40 cm below the ionization chamber. Measurements for the determination of HVLs were carried out in the service mode of the fluoroscope using fixed radiographic exposures at 60, 80, 100, and 120 kVp; Cu filtration thicknesses of 0, 0.1, 0.3, 0.6, and 0.9 mm; and fixed mAs values at a given kVp. Two calculation methods were used to determine the HVLs: the commonly used log-linear interpolation and the Lambert-W interpolation as described by Mathieu et al.[42]

BSFs were determined for all of the X-ray beam qualities described above in nominal FOVs of 11 cm, 22 cm, and 42 cm. The BSFs were determined by taking the average of three entrance air kerma ($K_{a,e}$) measurements in PMMA and dividing that by the average of three incident air kerma ($K_{a,i}$) measurements acquired free-in-air at the same distance from the focal spot and location within the X-ray field (with $K_{a,e}$ and $K_{a,i}$ quantities defined by the ICRU in publication 74).[30] All measurements were acquired with a Radcal 10 × 6-0.6 Farmer style ionization chamber. A PMMA sheet was machined to allow insertion of a moldable Aquaplast (therapy bolus) material to partially surround and hold the ionization chamber such that the chamber's plane of measurement was precisely at the surface of the PMMA. The fluoroscope was inverted from the normal orientation, allowing for an X-ray beam originating from above the patient table. PMMA of approximately 25 × 25 cm and 18 cm thick provided scatter medium underneath the 2.5-cm thick sheet holding the ionization chamber. The PMMA was stacked on the patient table and the table was raised so that the surface of the PMMA was located at 60 cm from the focal spot of the inverted fluoroscope.

PDDs

As shown in Figure 4-1, PDD measurements were acquired using a PTW (Freiburg, Germany) MP3 water tank with a Standard Imaging (Middleton, WI) Exradin Model P11 Spokas Chamber. The Spokas chamber used was a waterproof circular parallel-plate style ionization chamber with a collecting volume of 0.62 cm^3. This chamber has been identified as a good choice for relative measurements of kilovoltage X-ray beams in water.[43] An independent free-in-air reference chamber (PTW TN31010) was placed in the periphery of the X-ray field and used to normalize the water tank data to any fluctuations in fluoroscope output. Measurements were acquired from a water depth of 0 to 150 mm; however, the chosen ionization chamber’s effective point of measurement is 1 mm depth in water. Therefore, the data collected are reported at depths from 1 mm to 151 mm in water. Central axis X-ray beam PDD curves were measured for 60-, 80-, 100-, and 120-kVp X-ray beams with Cu filtration thicknesses of 0.0, 0.1, 0.3, 0.6, and 0.9 mm. A limited data set was acquired at 70 kVp for the purpose of validating interpolation between the other PDD data sets. The PDD measurements were acquired with the fluoroscope operated in the service mode, providing a continuous fluoroscopy X-ray beam. The fluoroscope was inverted from the typical orientation, providing an X-ray beam originating from above the water tank (Figure 4-1). The water tank was positioned and leveled so that the water surface was located at 60 cm from the focal spot, which represents the focal spot to IRP distance for the Artis ZeeGo fluoroscope. The IRP (defined by the IEC as 15 cm toward the X-ray tube from the isocenter of the C-arm gantry) is, given various assumptions, a good approximation of the skin entrance for most 2D and 3D fluoroscopic imaging applications. The PDD measurements were acquired at nominal FOVs of 11 cm, 22 cm, and 42 cm, resulting in X-ray beam field sizes at the water surface of approximately 4 cm × 4 cm, 8 cm × 8 cm, and 16 cm × 16 cm, respectively. The water surface area was approximately 60 cm × 50 cm, with a total water depth of approximately 30 cm. The SID was constant at 120 cm for all PDD measurements.

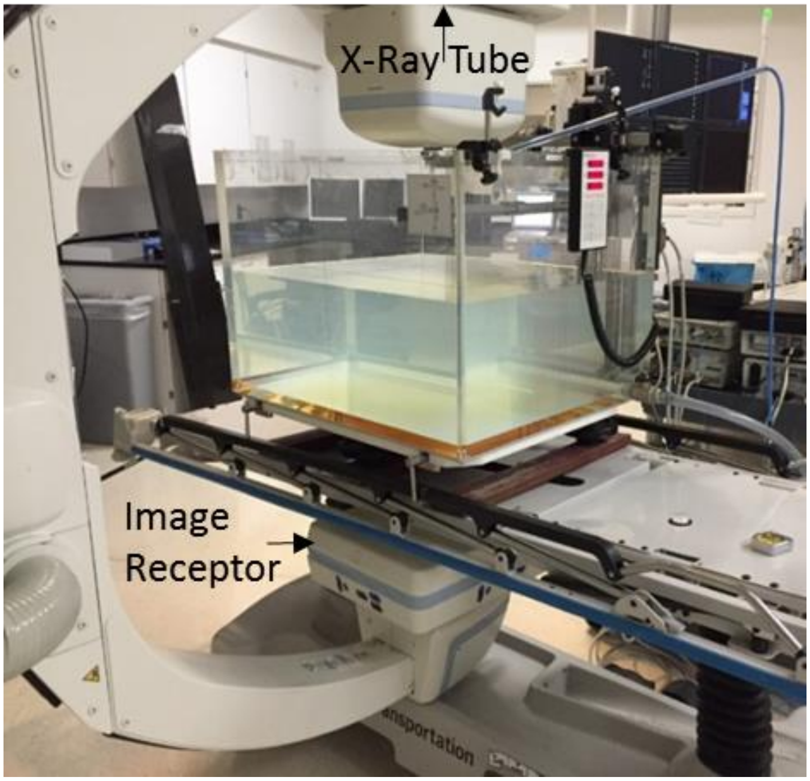

Figure 4-1. Fluoroscope and water tank setup for PDD measurements.

4.3 Results

Fluoroscopic X-ray beam characterization (HVLs, HCs, and BSFs)

Table 4-1 illustrates the accuracy and precision of the kVp measurements investigated in this study. The results indicate sound accuracy and precision, with deviations of less than 2% and a maximum standard deviation of 0.06 kVp. The accuracy of the noninvasive kV meter is ±1kV or 1% of the kV, whichever is greater, which, for the present study, results in a maximum potential deviation of 1.2 kV at 120 kV. In the remainder of this work, all references to kVp will therefore refer to the nominal set kVp without regard to these minor deviations.

Table 4-1. kVp precision and accuracy for beam spectra without Cu filtration.

Set kVp	Average kVp	Standard deviation	Percent deviation
60	58.8	0.06	1.9
80	79.7	0.00	0.4
100	98.7	0.06	1.3
120	118.3	0.06	1.4

First HVLs, second HVLs, HCs, and BSFs are shown in Table 4-2. The two interpolation methods used to calculate first and second HVLs yielded essentially identical results. In this table, the column labeled “Cu” indicates only the added filtration, not the total beam filtration (which would include inherent filtration).

Table 4-2. HVLs, HCs, and BSFs for a range of fluoroscopic X-ray beam qualities.

kVp	**Cu (mm)***	**HVL1 (mm Al)**	**HVL2 (mm Al)**	**HC**	**BSFs 4 × 4 cm FOV**	**BSFs 8 × 8 cm FOV**	**BSFs 16 × 16 cm FOV**
60	0	2.19	3.00	0.73	1.18	1.28	1.35
60	0.1	3.41	4.07	0.84	1.21	1.34	1.44
60	0.3	4.65	5.28	0.88	1.23	1.39	1.51
60	0.6	5.61	6.06	0.93	1.24	1.41	1.54
60	0.9	6.25	6.49	0.96	1.23	1.41	1.56
80	0	2.89	4.31	0.67	1.19	1.32	1.40
80	0.1	4.56	5.95	0.77	1.21	1.37	1.49
80	0.3	6.33	7.21	0.88	1.23	1.40	1.55
80	0.6	7.62	8.26	0.92	1.23	1.41	1.58
80	0.9	8.35	8.96	0.93	1.23	1.42	1.58
100	0	3.62	5.78	0.63	1.19	1.33	1.44
100	0.1	5.61	7.45	0.75	1.21	1.38	1.51
100	0.3	7.61	8.80	0.86	1.22	1.39	1.55
100	0.6	8.90	9.73	0.92	1.22	1.40	1.57
100	0.9	9.83	10.29	0.96	1.21	1.39	1.56
120	0	4.37	7.09	0.62	1.20	1.34	1.45
120	0.1	6.55	8.39	0.78	1.21	1.37	1.51
120	0.3	8.56	9.79	0.87	1.21	1.38	1.54
120	0.6	9.95	10.85	0.92	1.20	1.38	1.54
120	0.9	10.82	11.62	0.93	1.20	1.37	1.54

PDDs

Figures 4-2 through 4-5 illustrate the PDDs for 60, 80, 100, and 120 kVp at various Cu filtration thicknesses, from the water surface to a depth of 150 mm (effective depths of 1 mm-151 mm) for the three X-ray field sizes. See supplemental material in Appendix B for the complete PDD data sets.

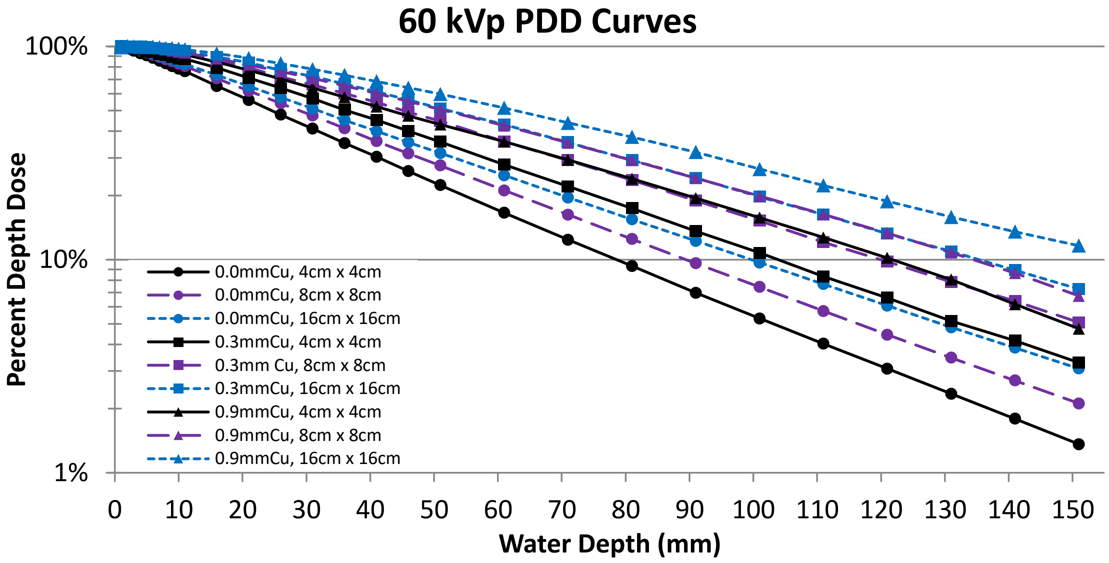

Figure 4-2. Semilog plot of 60 kVp PDDs for three Cu filtration thicknesses and three FOVs.

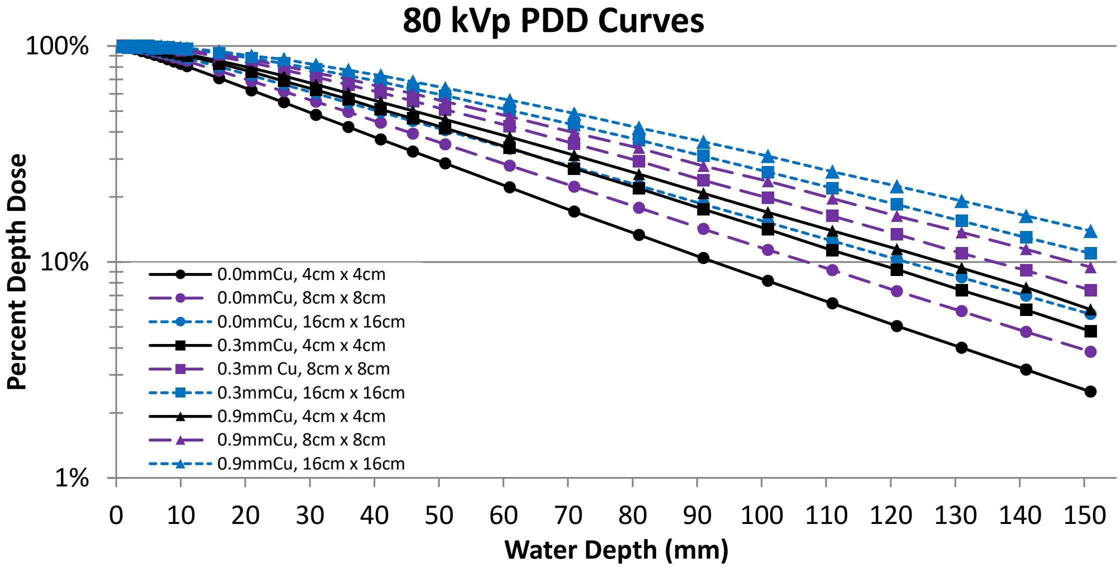

Figure 4-3. Semilog plot of 80 kVp PDDs for three Cu filtration thicknesses and three FOVs.

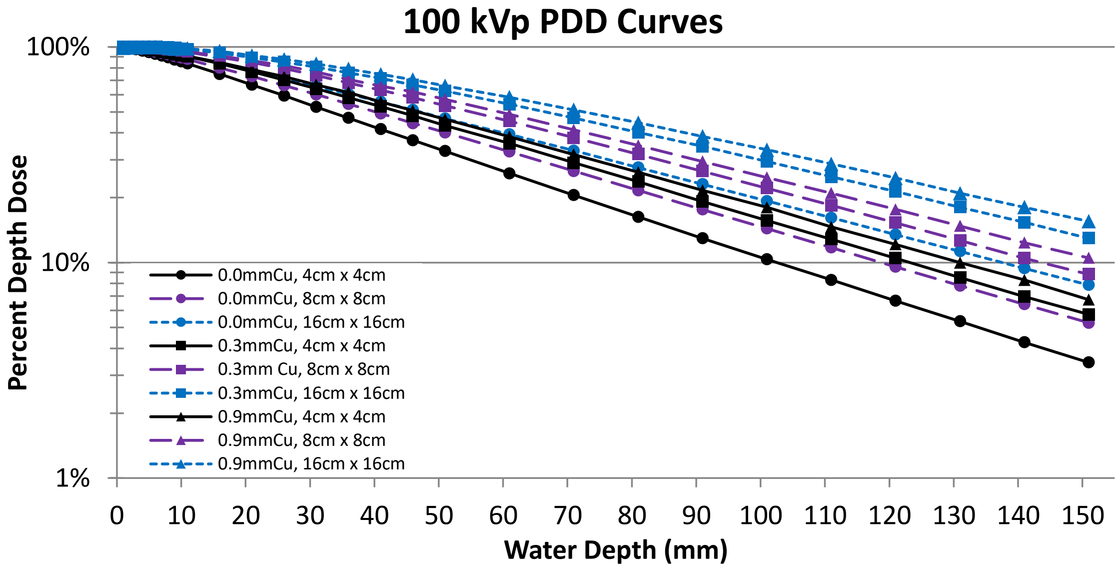

Figure 4-4. Semilog plot of 100 kVp PDDs for three Cu filtration thicknesses and three FOVs.

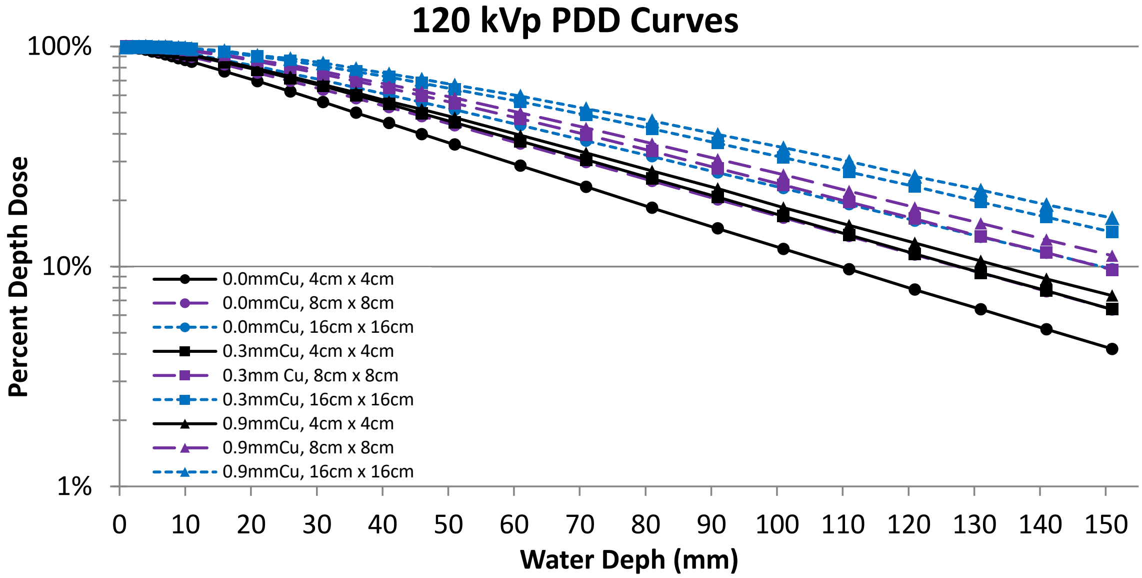

Figure 4-5. Semilog plot of 120 kVp PDDs for three Cu filtration thicknesses and three FOVs.

In Figures 4-2 and 4-3, for the PDDs at 0.9 mm Cu 60 kVp (all FOVs) and 0.9 mm Cu 80 kVp (smallest FOV), a 3-point smoothing algorithm was used to reduce the magnitude of the noise because of the low dose rates encountered. The smoothing algorithm is a built-in feature of the PTW MEDPHYSTO mc^2 software used to operate the water tank and analyze the acquired data. Figure 4-6 illustrates the PDDs for all acquired Cu filtration thicknesses at 80 kVp in the intermediate FOV and provides a comparison of the PDD without Cu filtration to that of the same kVp without Cu filtration from the previous publication by Fetterly et al.[40]

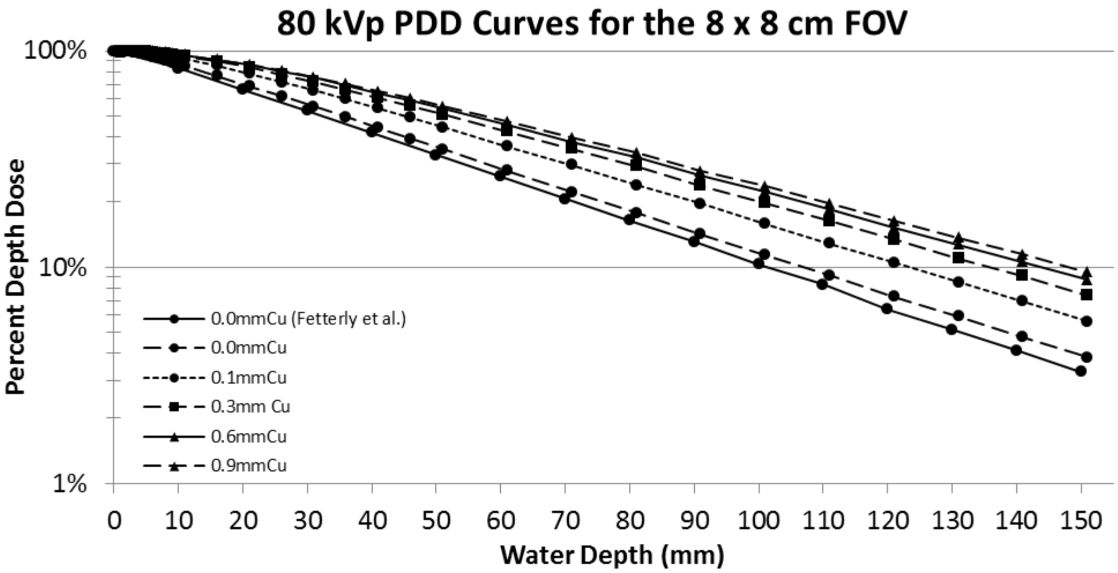

Figure 4-6. Semilog plot of 80 kVp PDDs for all five acquired Cu filtration thicknesses at the intermediate X-ray field size.

Figure 4-7 provides a comparison among the three field sizes at the lowest and highest beam qualities evaluated, 60 kVp without Cu filtration and 120 kVp with 0.9 mm Cu filtration.

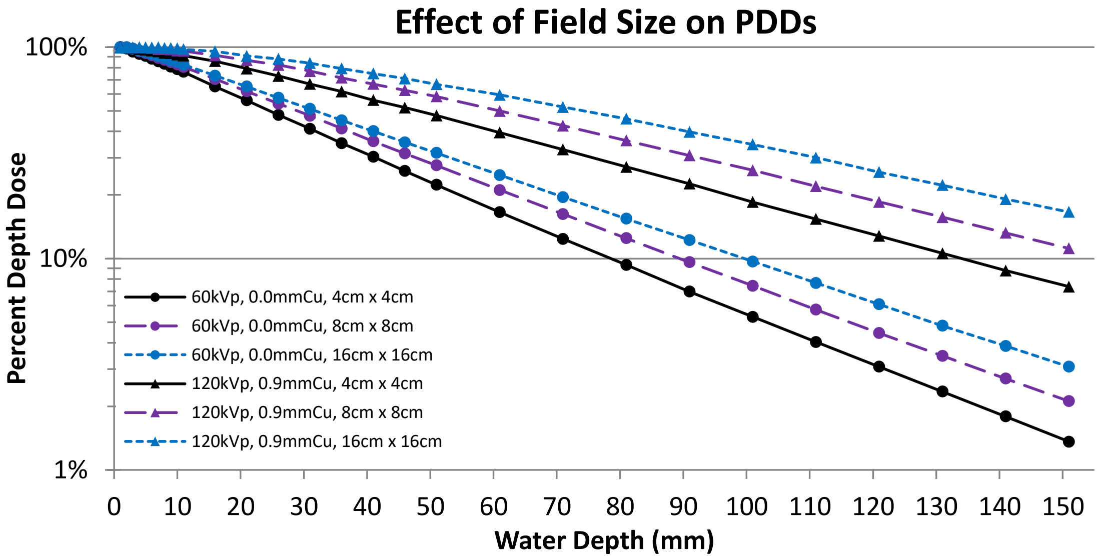

Figure 4-7. PDDs for all three field sizes at the lowest and highest X-ray beam qualities.

4.4 Discussion

Fluoroscopic X-ray beam characterization (HVLs, HCs, and BSFs)

For the X-ray beam qualities without Cu filtration, we observed 7% to 16% higher first HVL thicknesses as compared to the previously published data by Fetterly et al.[40] Several factors may account for these differences. First, the minimum HVL requirements of the FDA changed since that publication, requiring larger HVLs on X-ray equipment manufactured as of June 2006; as an example, the required minimum HVL at 100 kVp changed from 2.7 to 3.6 mm of Al.[41] Additionally, X-ray generator and tube architecture have changed over the past

15 years. The previously reported data were acquired on a fluoroscope using a three-phase X-ray generator, whereas the fluoroscope in the present study uses a high-frequency generator with a nearly constant potential, resulting in higher X-ray beam quality.

As illustrated in Table 4-2, HCs tend to increase for a fixed kVp with increasing filtration and tend to decrease for a fixed filtration with increasing kVp; these same trends were reported by Harrison[44] over a range of 60 to 100 kVp with total filtration ranging from 0.9 to 2.9 mm of Al. However, the study by Fetterly et al[40] indicated nearly constant HCs across all kVps evaluated; intra-kVp comparison was not available, as only a single filtration level was available for each kVp. In the AAPM TG125 report, there is a graphical representation of first HVL data from a fluoroscope with Cu filtration; the trends of the first HVLs with respect to X-ray beam quality (as defined by the kVp and added Cu filtration) compare well with the trends from the current study.[25] Direct comparison of the data is limited because only a graphical representation of the data is provided in the report from TG125; however, it appears that the first HVL data in the present study are generally slightly lower than that reported by TG125.

Second HVLs and HCs for fluoroscopic X-ray beam spectra incorporating Cu filtration have not been previously reported. These values further define the X-ray beam spectra used to acquire the PDDs reported in this study and are necessary for applying the PDD results to other fluoroscopic X-ray beams. As indicated by the ICRU in publication 74, the X-ray beam quality may not be adequately described by only the kVp and first HVL.[30]

For similar X-ray beam qualities and field sizes, the BSFs reported in Table 4-2 are in good agreement with previously published data.[30,39,45-47] A majority of the X-ray beam qualities and FOVs investigated in the present study have not been previously reported. These BSFs can be used to convert $K_{a,i}$ to $K_{a,e}$ given agreement with the X-ray beam quality and FOV or accounting for dissimilarities.[30]

PDDs

As illustrated in Figure 4-6, for 80 kVp PDDs at the intermediate X-ray field size, the PDDs for the X-ray beam spectra without Cu filtration compared well to previously published data, given various differences in geometry and equipment. The data in the present study were acquired at a source-to-surface distance (SSD) of 60 cm, whereas the previous data from Fetterly et al were acquired at an SSD of 50 cm.[40,43,44] The X-ray field sizes were the same for the intermediate field size (8 cm × 8 cm at SSD) and slightly larger in the present study (16 cm × 16 cm vs 15 cm × 15 cm at SSD). Additionally, the fluoroscope used in the present study allowed for an anteroposterior projection (Figure 4-1), whereas the PDD data in the previous study were acquired with a lateral projection, requiring a water tank with a thin Mylar side window. The use of such a water tank presents two potential sources of uncertainty, which were discussed by the authors. First, the presence of the Mylar window may cause energy fluence changes. Second, the thin window can deflect under the water pressure, causing uncertainty in the surface location. The setup used in the present study avoided these uncertainties.

The uncertainty in the measurements acquired with the Spokas chamber are likely within 3%. Li et al[43] evaluated various dosimeters for use in kilovoltage therapy beams and determined that the Spokas parallel-plate chamber yielded good results, estimating the uncertainty based on the energy dependence of the chamber to be less than 3% at 100 kVp with a first HVL of 2.43 mm Al and an HC of 0.72.

A limited PDD data set at 70 kVp (included in Appendix B) was also acquired at the intermediate X-ray field size to validate the use of linear interpolation between the 60 kVp and 80 kVp PDD data sets, as a large number of clinical procedures are performed within this range of kVps. The error in the linearly interpolated PDD values between the 60 kVp and 80 kVp PDD data sets as compared to the measured PDDs at 70 kVp was less than 4%. Therefore, the use of linear interpolation between the data sets for kVp values other than those acquired can be expected to provide accurate results.

Figure 4-7 illustrates an interesting phenomenon whereby the distance between PDD points of different field sizes (for a given kVp at a given depth) is nearly identical, irrespective of the beam spectra (as defined by the kVp and Cu filtration). In Figure 4-7, the lowest and highest X-ray beam qualities are graphed at all three X-ray field sizes acquired. A nearly constant distance between the

PDDs of different field sizes at a given depth is apparent, and that distance is maintained without regard to the X-ray beam quality. This implies that interpolation between X-ray beam areas is also possible assuming that the X-ray beam areas are two-dimensionally symmetric, as was the case in the present study.

Although these data were acquired on a fluoroscope, the X-ray beam spectra evaluated could be encountered on other X-ray modalities, specifically on radiographic or CT units. The PDD data sets may be applicable to these modalities provided that care is taken to account for potential differences in X-ray field inhomogeneities (specifically for CT, in which beam-shaping [bowtie] filters provide a nonuniform 2D dose and beam quality distribution) and geometric factors.

Cu filtration

In general, the effects of spectral filtration on the HVLs, HCs, BSFs, and PDDs in this study were as theory would predict: the quantities were all shifted higher with increasing Cu filtration for a given kVp. For all kVps and FOVs, PDDs at 0.6 and 0.9 mm Cu were very similar, with the curves getting closer with increasing kVp (see Figure 4-6 for an example at one kVp and X-ray field size). For these same beam qualities, the HCs were also very similar and in all instances exceeded 0.9. This signifies that there are few lower energy photons remaining in the X-ray beam to attenuate, and additional filtration primarily increases X-ray tube loading without substantially affecting the X-ray beam quality for a given kVp. Thus, there are diminished benefits to using more than 0.6 mm of Cu at any of the kVps evaluated and little to no benefit to using more than 0.3 mm of Cu beyond 80 kVp.

Application of results for soft-tissue dose estimations

With data commonly available on interventional fluoroscopes through the Digital Imaging and Communications in Medicine (DICOM) Radiation Dose Structured Report, the results of this study can be applied to soft-tissue dosimetry. First the dose at the patient's skin entrance must be determined. Methodology for determining the dose to the skin entrance from fluoroscopic procedures has been reported by Jones et al.[28] The DICOM Radiation Dose Structured Report contains the $K_{a,r,}$ kVp, Cu filtration, procedure table height, and the air-kerma-area-product for every radiation event from a fluoroscopic procedure. Caution should be exercised to ensure adequate accuracy in the $K_{a,r}$. A calibration factor should be applied to the raw $K_{a,r}$ to account for potential deviations and, if necessary, beam quality dependence.[19,35] If the X-ray beam field size is not directly available, the X-ray beam area in the plane of the reference point could be estimated by dividing the air-kerma-area-product by the $K_{a,r}$; beam area corrections could be made knowing the focal-spot-to-patient distance and the SID. Assuming a posteroanterior X-ray beam projection, the $K_{a,r}$ can be corrected by inverse-square-law to the plane of the patient (table height) yielding the $K_{a,i}$. Dose in soft tissue at depth "d" from an X-ray beam with area "A" at the patient skin entrance can be estimated by:

$$D(d,A,E) = K_{a,i} * BSF(A,E) * f`factor * PDD(d,A,E)$$

F-factors for the majority of the X-ray beam qualities are available in either ICRU report 44 or from Benmakhlouf et al, although an f-factor of 1.06 is commonly applied.[28,46,48] BSFs and PDDs reported in the present study can be interpolated between energies. BSFs can also be interpolated between X-ray beam areas. PDDs, being relative measurements, have a more complicated relationship with beam area and depth, but interpolation between X-ray beam areas at a given depth is consistent across all beam energies evaluated and would be expected to yield accurate results.

Estimation of uncertainty

The uncertainty in a dose estimate calculated as described above results in uncertainty from several factors. First, there is an uncertainty in the $K_{a,i}$ of 4% from the external ionization chamber used to perform the measurements. Second, there is an uncertainty in the BSFs from the in-air and in-phantom measurements used to calculate the BSF; each with an uncertainty of 4% resulting in a total BSF uncertainty of 6%. Thirdly, there is an uncertainty in the PDDs resulting from the Spokas chamber of 3%. Assuming a negligible uncertainty in the f-factor, the overall relative uncertainty (Ɛ) in the dose estimation at depth in soft-tissue—in as much as soft-tissue is water equivalent—is:

$$\mathcal{E} = \sqrt{(0.04)^2 + (0.06)^2 + (0.03)^2} = 0.078 = 7.8\%$$

4.5 Conclusion

The primary purposes of this study were to characterize a set of X-ray beam qualities and quantify associated PDDs that have not been previously investigated. The intended applications for the results are threefold; first for use in performing radiation dose estimations to soft tissue, for which an approach was offered; second, to assist in determining fetal dose estimates; third, to provide reference data for Monte Carlo or other X-ray simulation software. The equipment and processes used to achieve this goal were validated by the results acquired for X-ray beam qualities without Cu filtration, which compared well to previous published research. X-ray beam characteristics for beam qualities incorporating Cu filtration were successfully acquired and are provided herein. However, limitations exist in the applicability of our data to other fluoroscopes or other X-ray modalities. Before using the data provided, individuals must ensure that the X-ray beam characteristics, geometry, and X-ray beam field sizes match those of the data reported or must take care in accounting for any differences. Additionally, the results of this study and the methodology for determining the dose at depth in soft tissue described above are only applicable to water equivalent homogenous soft tissue; the presence of bone or other inhomogeneities is not considered.

CHAPTER 5 X-RAY BEAM PROFILES AT DEPTH FROM FLUOROSCOPIC BEAM QUALITIES INCORPORATING COPPER FILTRATION

5.1 Introduction

There are instances in which radiation dose estimation for tissue outside of the primary fluoroscopic X-ray beam may be necessary. For instance, this is a consideration for FGI procedures in pregnant patients when the target of the intervention is in close proximity to the fetus (eg, for renal mass embolizations). In these cases, it is necessary to understand the X-ray beam qualities encountered and how the X-ray beam intensity varies with distance from the margins of the X-ray field and depth in tissue.[38] However, the X-ray beam qualities commonly used in state-of-the-art fluoroscopes are not well characterized, nor have X-ray beam profiles for these beam qualities been investigated and reported; this is the aim of the research presented.

5.2 Materials and Methods

A Siemens (Erlangen, Germany) Artis ZeeGo C-arm fluoroscope was used to generate X-ray beams for all measurements associated with this study. The fluoroscope was operated in the service mode to allow manual control of the kVp and Cu filtration thicknesses, which predominately define the X-ray beam spectra. The fluoroscope was rotated 180 degrees from the typical frontal projection to provide an X-ray beam originating from above the procedure table. A PTW (Freiburg, Germany) MP3 automatic scanning water tank was set up within the C-arm gantry such that the water level was located at 60 cm from the focal spot of the X-ray tube. This distance from the focal spot corresponds to the interventional reference plane (IRP) of the fluoroscope.

For validation purposes, PDDs were acquired at 60 kVp and 120 kVp without additional Cu filtration using a Standard Imaging (Middleton, WI) Exradin Model P11 Spokas parallel-plate ionization chamber and a PTW type 60016 silicon diode detector. Fluoroscopic X-ray beam profiles were then acquired parallel (in-plane) and perpendicular (cross-plane) to the anode-cathode axis. Profile measurements were repeated at nominal X-ray field sizes of 42 cm and 22 cm; at kVps of 60, 80, 100, and 120; at Cu filtration thicknesses of 0, 0.1, 0.3, 0.6, and 0.9 mm; and at depths in water of 10 mm, 50 mm, and 100 mm.

The fluoroscopic X-ray beam qualities used in this investigation were characterized by their first HVLs, second HVLs, and homogeneity coefficients. The methodology and results for determining the beam quality characteristics are reported in Chapter 4.

5.3 Results

Figure 5-1 illustrates the PDDs acquired using the Spokas chamber and the diode detector to validate the use of the diode detector over the range of kVps to be used for the X-ray beam profiles.

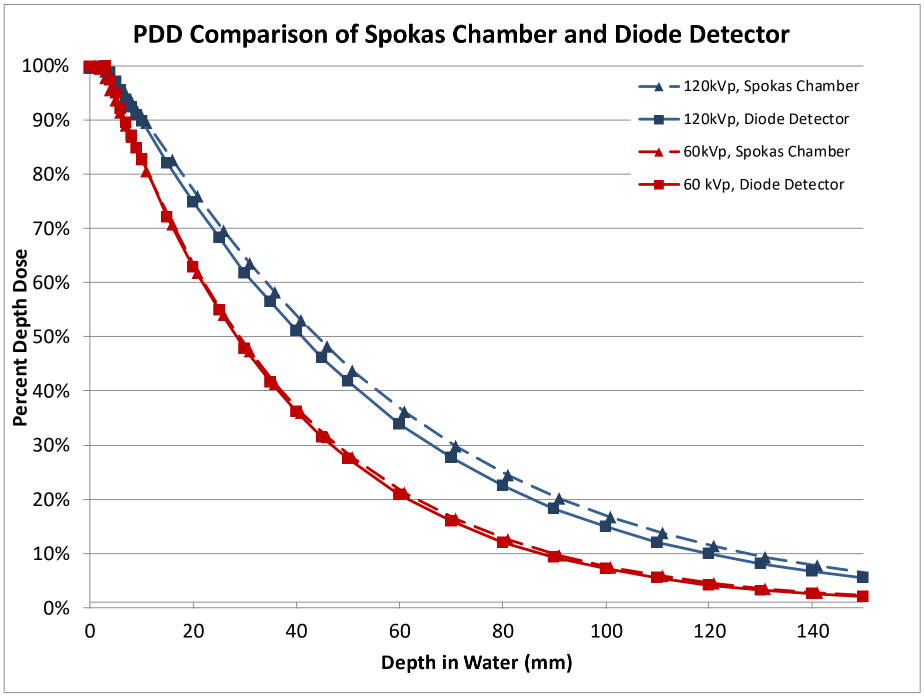

Figure 5-1. Comparison of PDDs acquired with a Spokas parallel plate ionization chamber and a diode detector.

All profiles are normalized to the central-axis maximum (surface) measurement by using the PDD curves previously reported (Chapter 4). Figures 5-2 through 5-11 illustrate the X-ray beam profiles for the 60 kVp X-ray beam spectra and field sizes. Figures 5-12 through 5-21 illustrate the X-ray beam profiles for the 80 kVp X-ray beam spectra and field sizes. Figures 5-22 through 5-31 illustrate the X-ray beam profiles for the 100 kVp X-ray beam spectra and field sizes. Figures 5-32 through 5-41 illustrate the X-ray beam profiles for the 120 kVp X-ray beam spectra and field sizes.

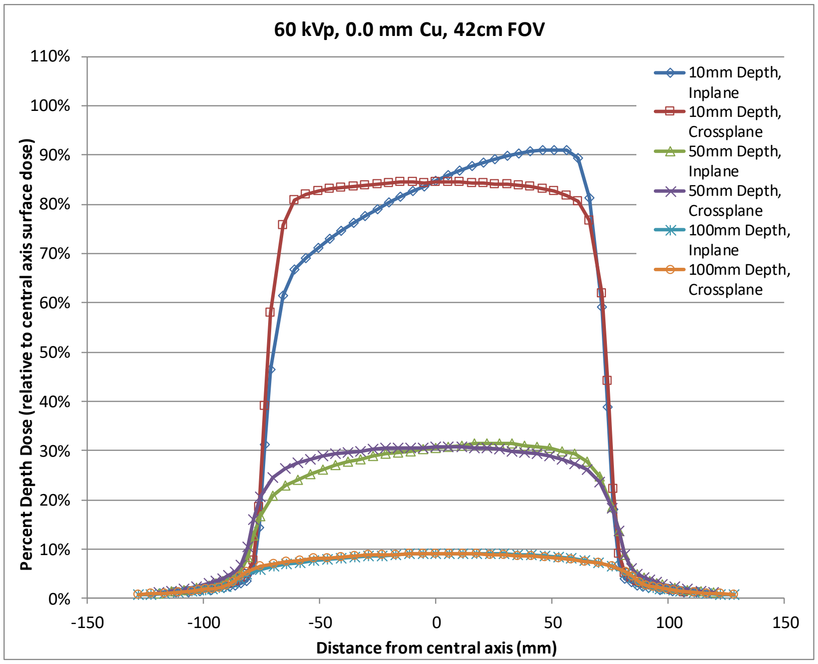

Figure 5-2. Fluoroscopic X-ray beam profiles for 60 kVp, no filtration, in the 42 cm FOV.

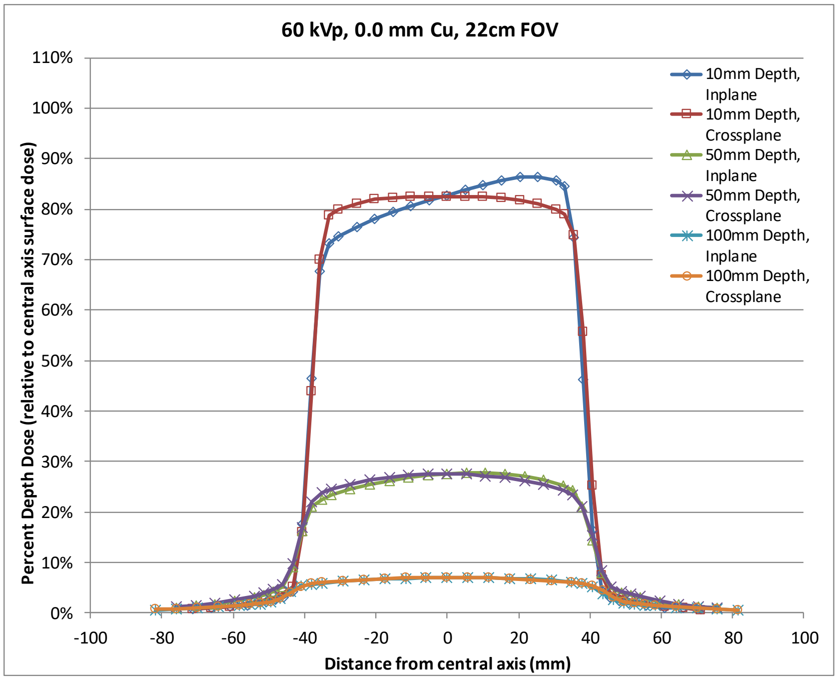

Figure 5-3. Fluoroscopic X-ray beam profiles for 60 kVp, no filtration, in the 22 cm FOV.

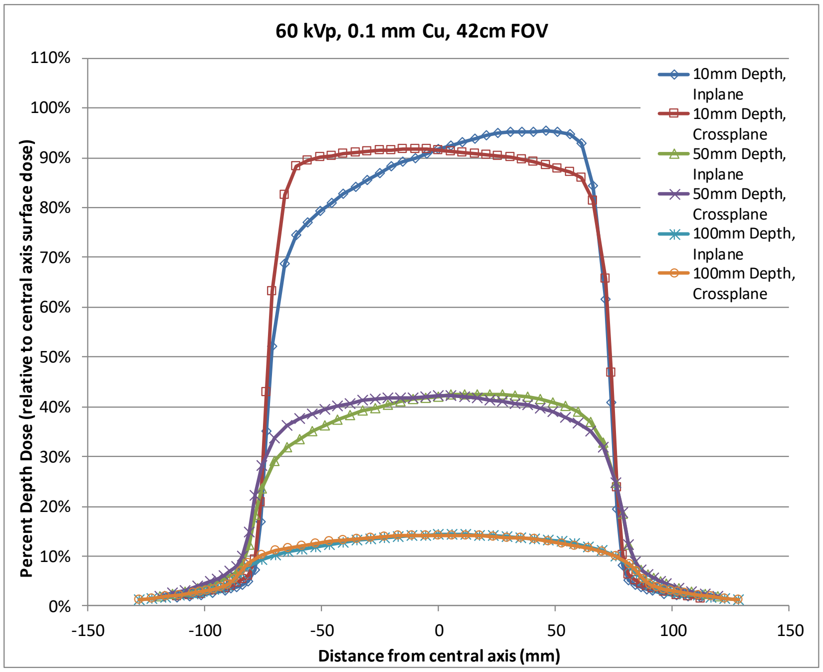

Figure 5-4. Fluoroscopic X-ray beam profiles for 60 kVp, 0.1 mm Cu filtration, in the 42 cm FOV.

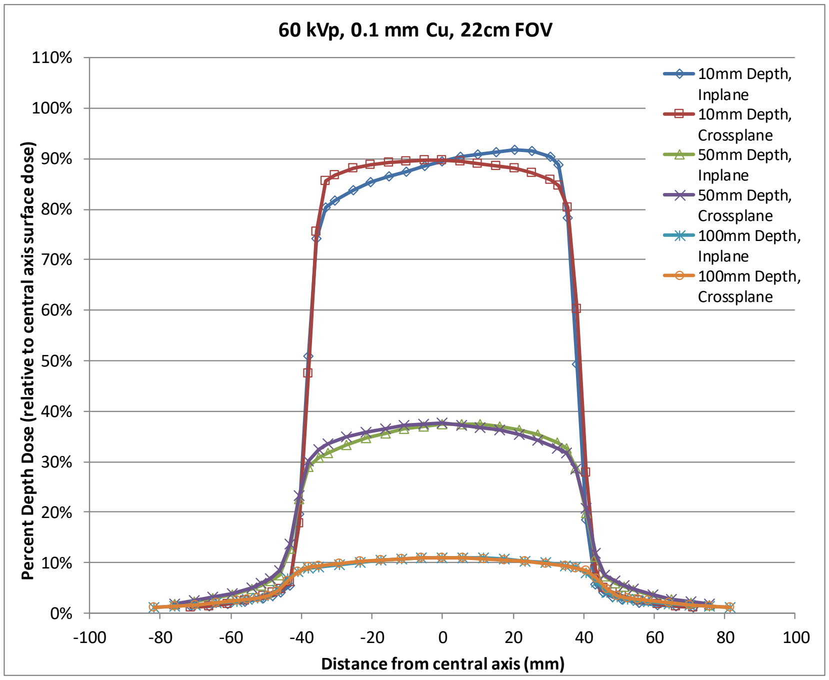

Figure 5-5. Fluoroscopic X-ray beam profiles for 60 kVp, 0.1 mm Cu filtration, in the 22 cm FOV.

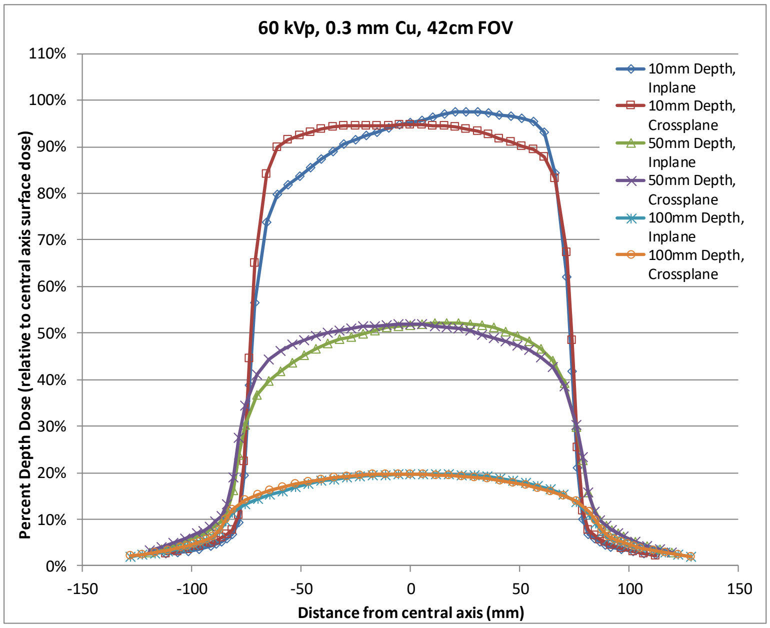

Figure 5-6. Fluoroscopic X-ray beam profiles for 60 kVp, 0.3 mm Cu filtration, in the 42 cm FOV.

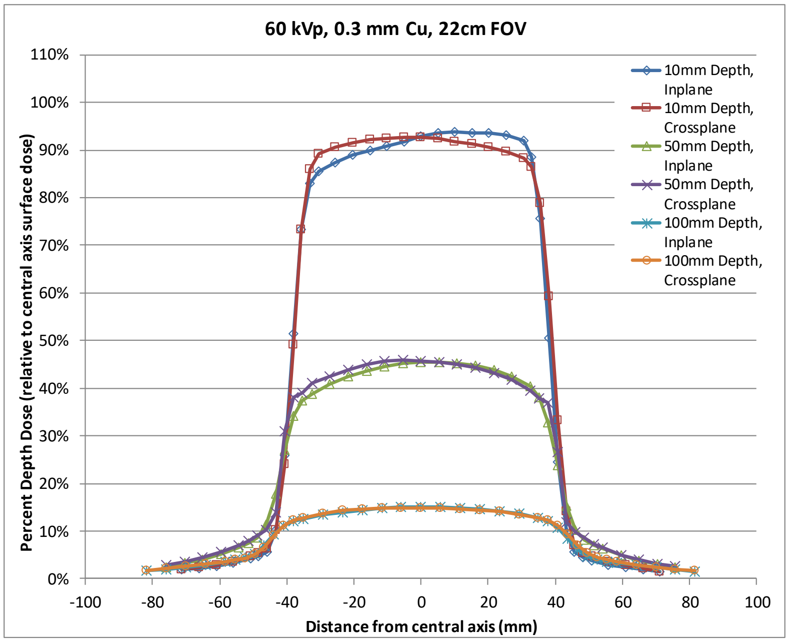

Figure 5-7. Fluoroscopic X-ray beam profiles for 60 kVp, 0.3 mm Cu filtration, in the 22 cm FOV.

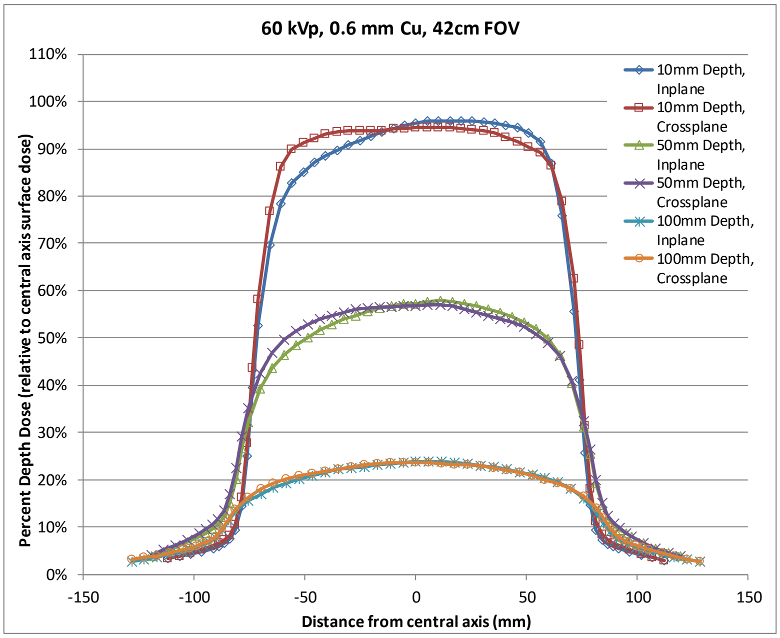

Figure 5-8. Fluoroscopic X-ray beam profiles for 60 kVp, 0.6 mm Cu filtration, in the 42 cm FOV.

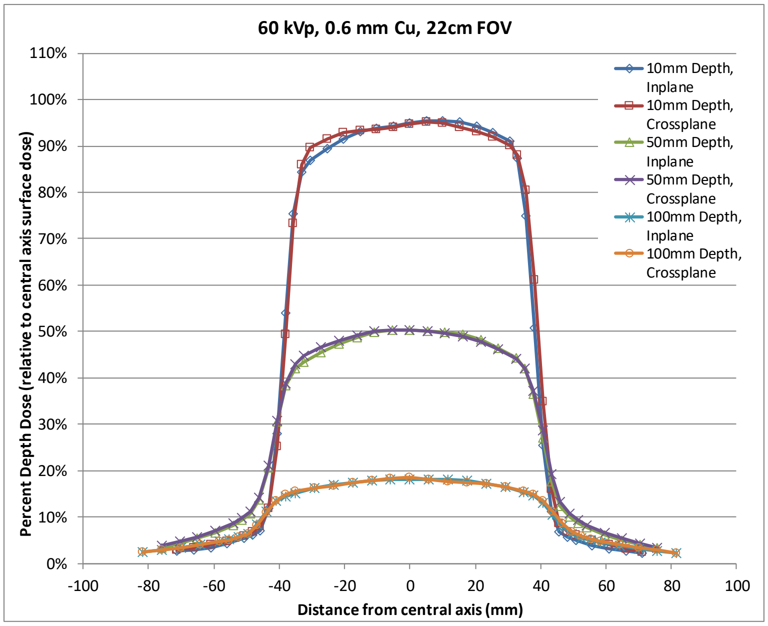

Figure 5-9. Fluoroscopic X-ray beam profiles for 60 kVp, 0.6 mm Cu filtration, in the 22 cm FOV.

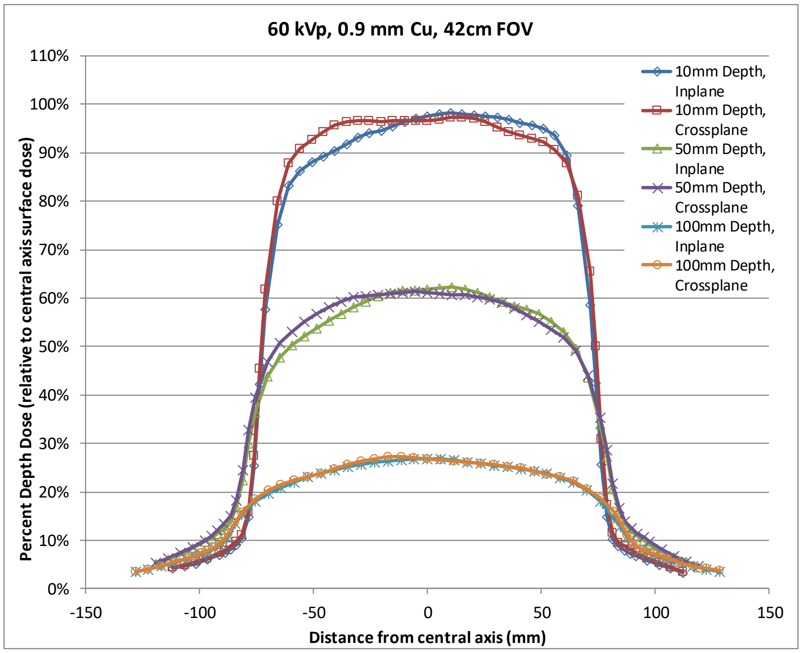

Figure 5-10. Fluoroscopic X-ray beam profiles for 60 kVp, 0.9 mm Cu filtration, in the 42 cm FOV.

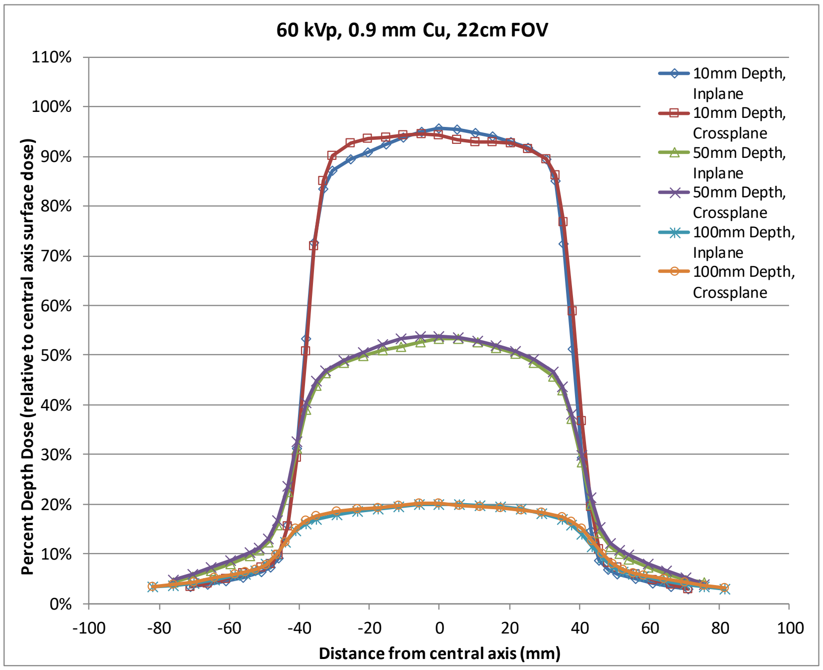

Figure 5-11. Fluoroscopic X-ray beam profiles for 60 kVp, 0.9 mm Cu filtration, in the 22 cm FOV.

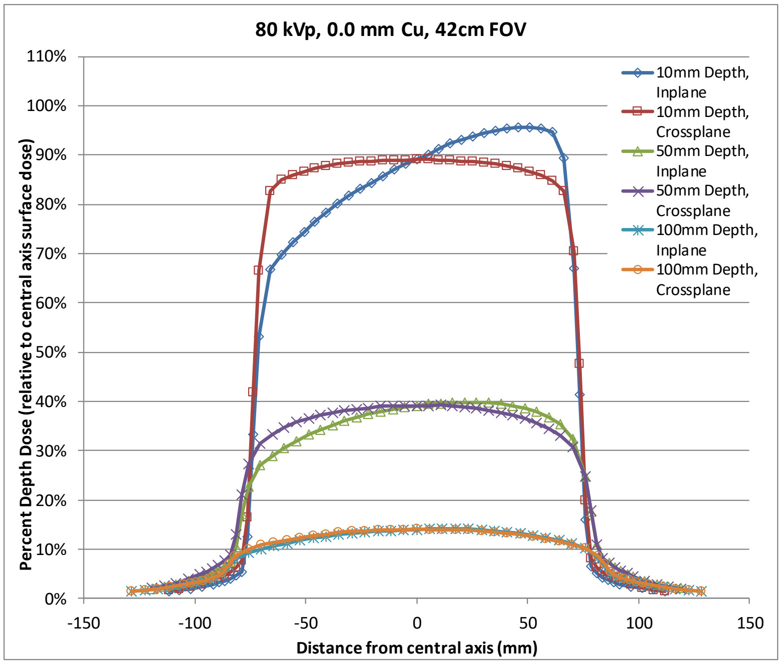

Figure 5-12. Fluoroscopic X-ray beam profiles for 80 kVp, no filtration, in the 42 cm FOV.

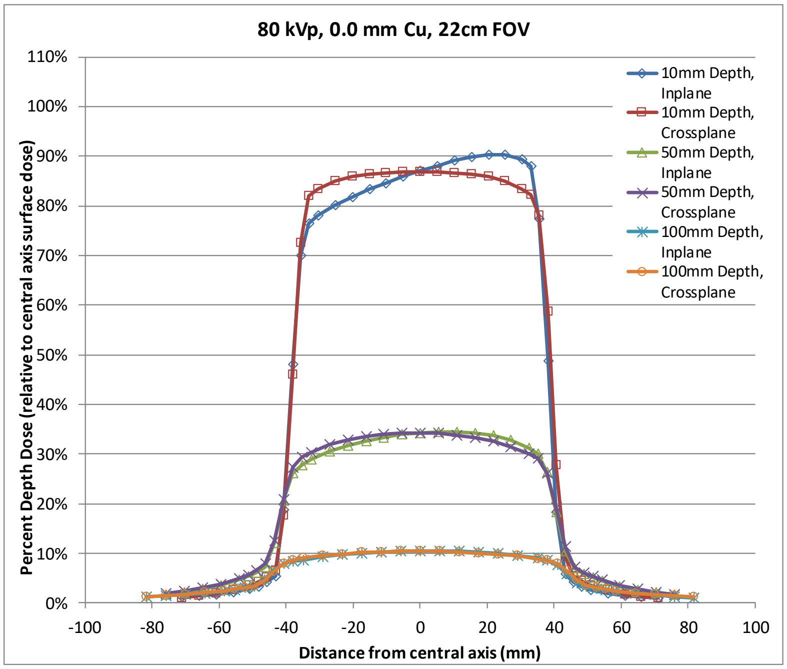

Figure 5-13. Fluoroscopic X-ray beam profiles for 80 kVp, no filtration, in the 22 cm FOV.

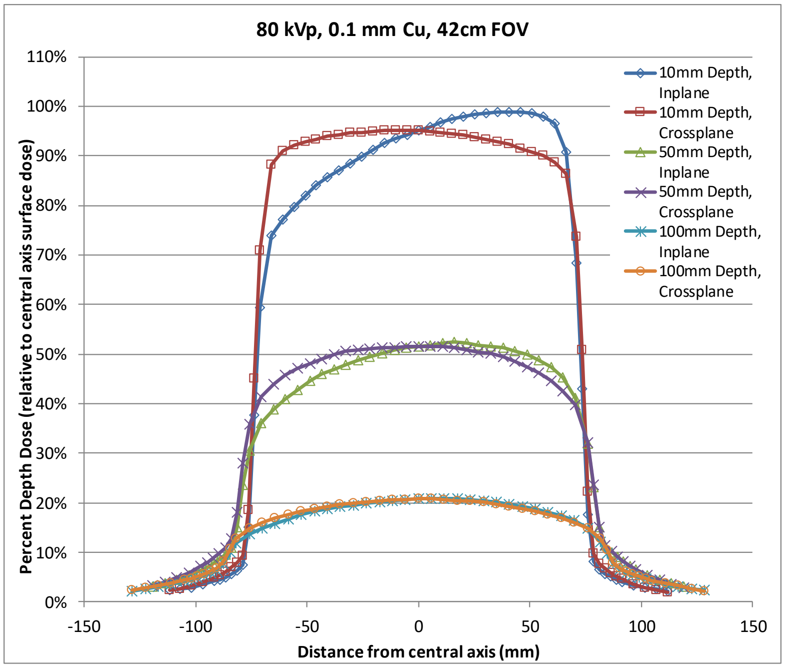

Figure 5-14. Fluoroscopic X-ray beam profiles for 80 kVp, 0.1 mm Cu filtration, in the 42 cm FOV.

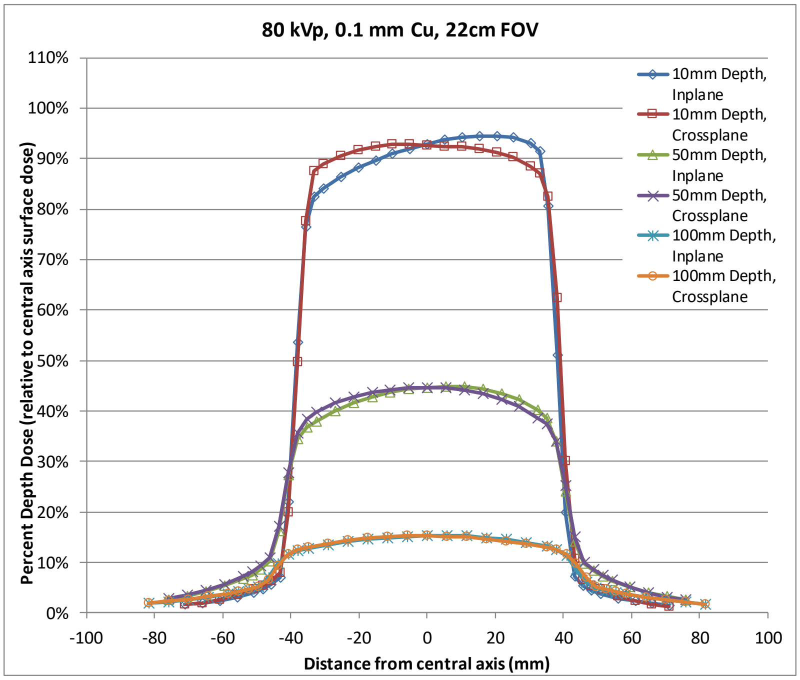

Figure 5-15. Fluoroscopic X-ray beam profiles for 80 kVp, 0.1 mm Cu filtration, in the 22 cm FOV.

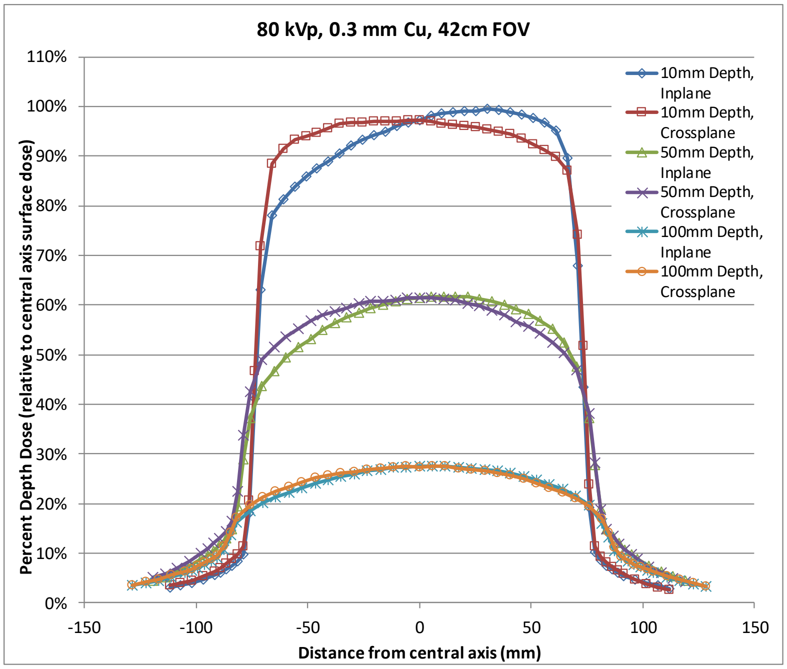

Figure 5-16. Fluoroscopic X-ray beam profiles for 80 kVp, 0.3 mm Cu filtration, in the 42 cm FOV.

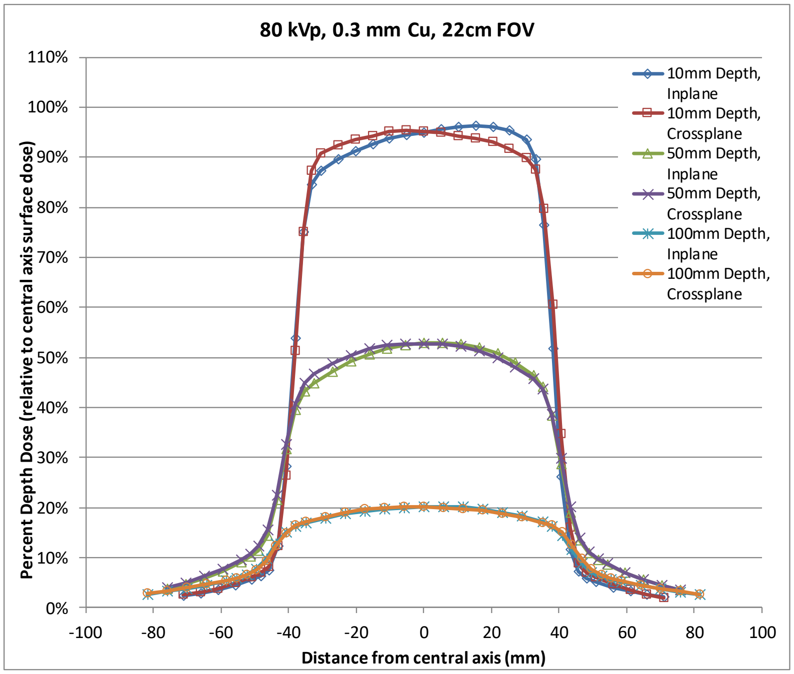

Figure 5-17. Fluoroscopic X-ray beam profiles for 80 kVp, 0.3 mm Cu filtration, in the 22 cm FOV.

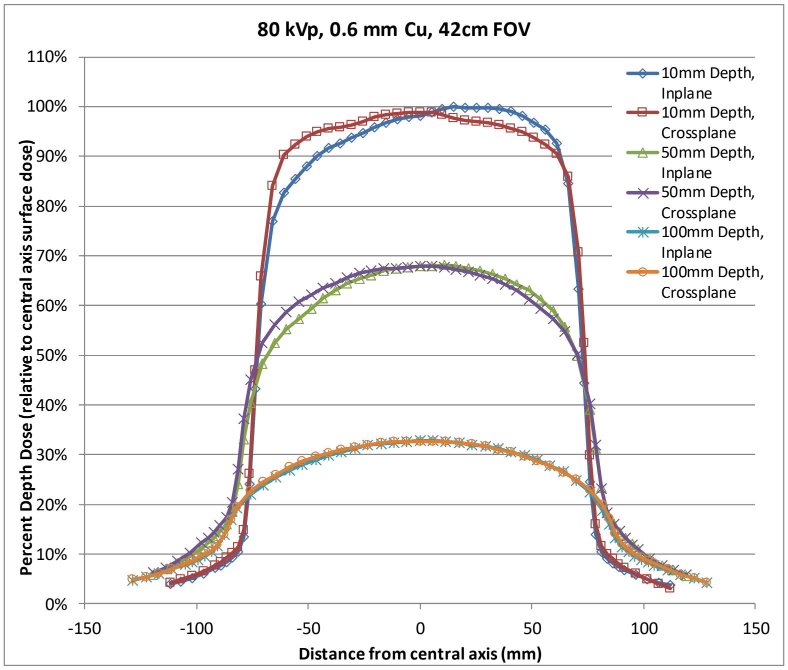

Figure 5-18. Fluoroscopic X-ray beam profiles for 80 kVp, 0.6 mm Cu filtration, in the 42 cm FOV.

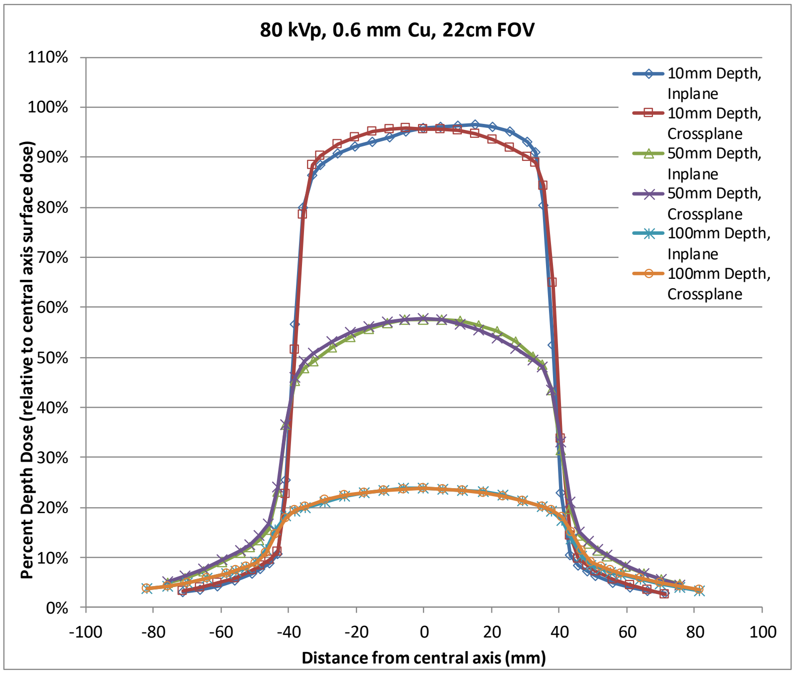

Figure 5-19. Fluoroscopic X-ray beam profiles for 80 kVp, 0.6 mm Cu filtration, in the 22 cm FOV.

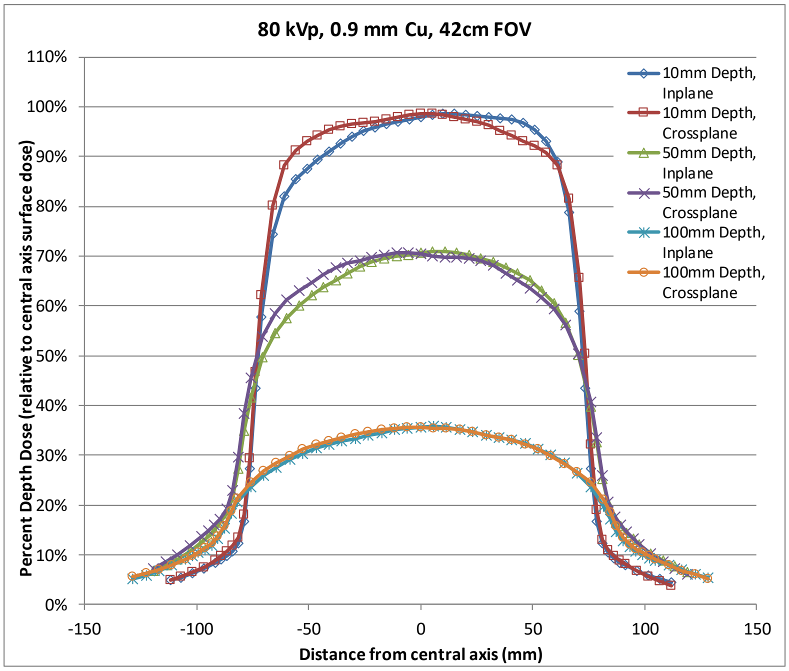

Figure 5-20. Fluoroscopic X-ray beam profiles for 80 kVp, 0.9 mm Cu filtration, in the 42 cm FOV.

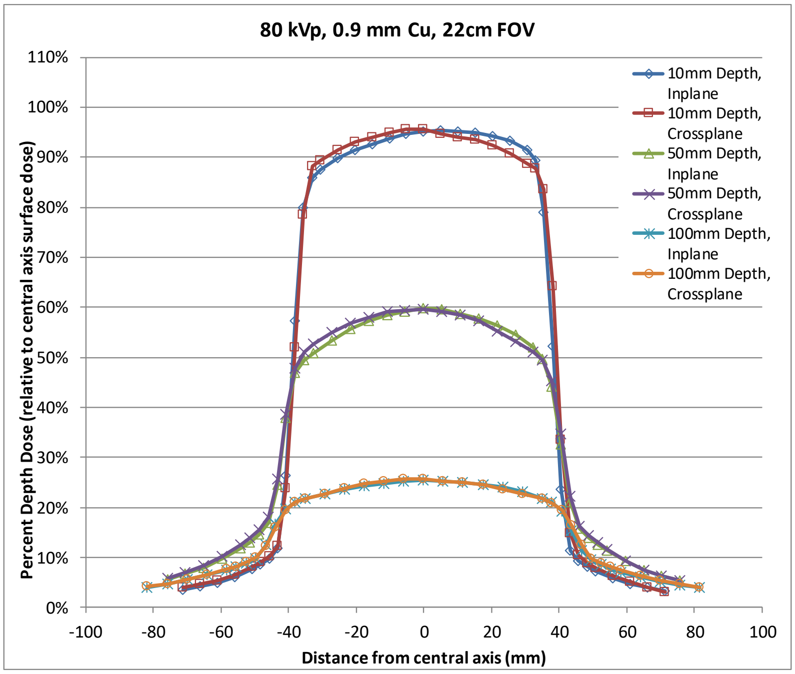

Figure 5-21. Fluoroscopic X-ray beam profiles for 80 kVp, 0.9 mm Cu filtration, in the 22 cm FOV.

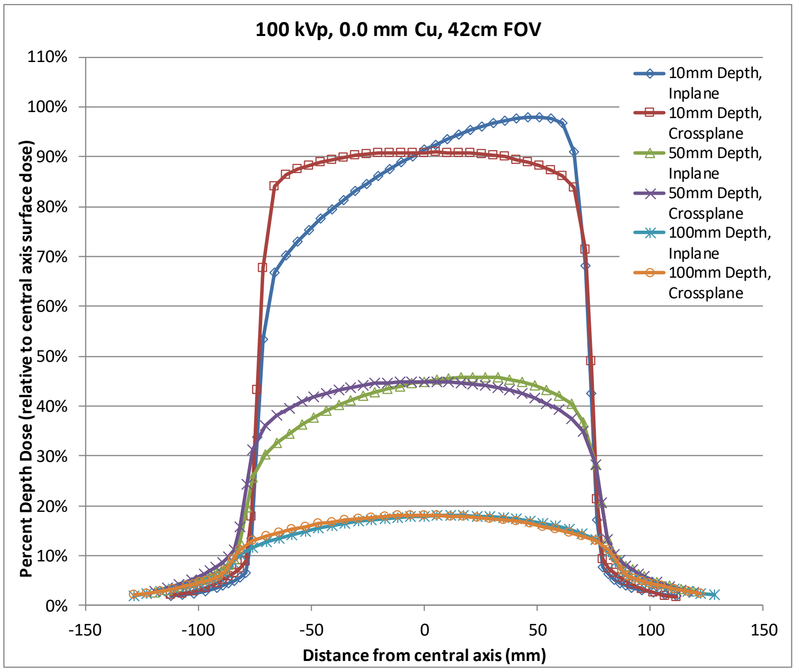

Figure 5-22. Fluoroscopic X-ray beam profiles for 100 kVp, no filtration, in the 42 cm FOV.

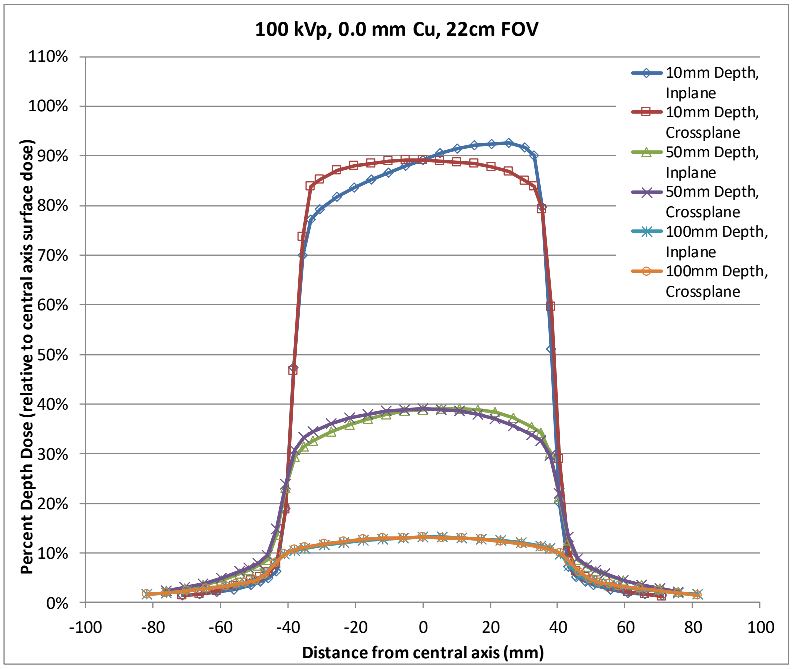

Figure 5-23. Fluoroscopic X-ray beam profiles for 100 kVp, no filtration, in the 22 cm FOV.

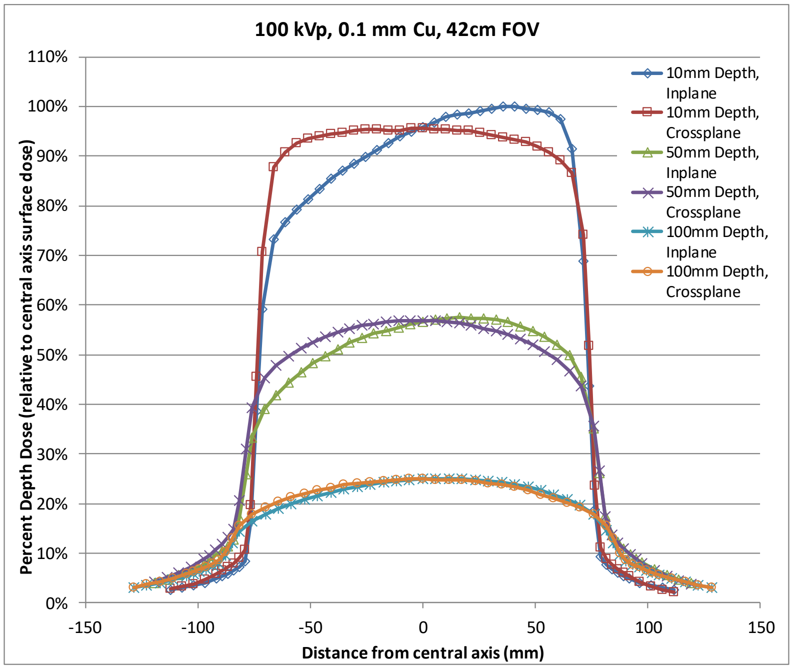

Figure 5-24. Fluoroscopic X-ray beam profiles for 100 kVp, 0.1 mm Cu filtration, in the 42 cm FOV.

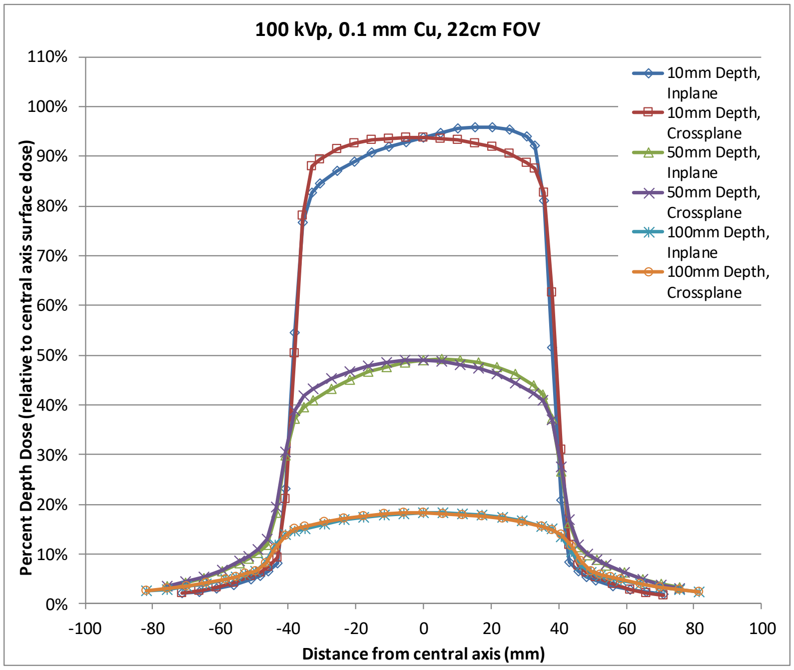

Figure 5-25. Fluoroscopic X-ray beam profiles for 100 kVp, 0.1 mm Cu filtration, in the 22 cm FOV.

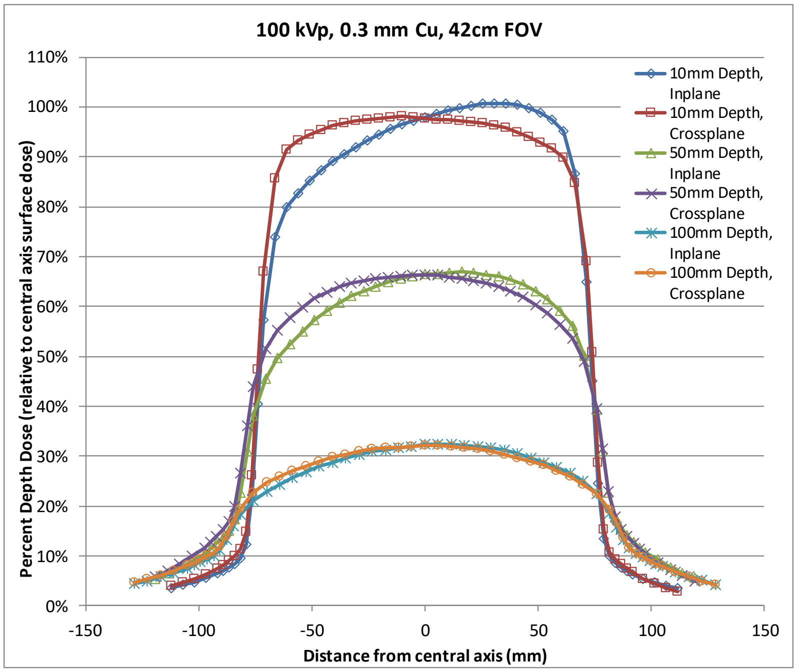

Figure 5-26. Fluoroscopic X-ray beam profiles for 100 kVp, 0.3 mm Cu filtration, in the 42 cm FOV.

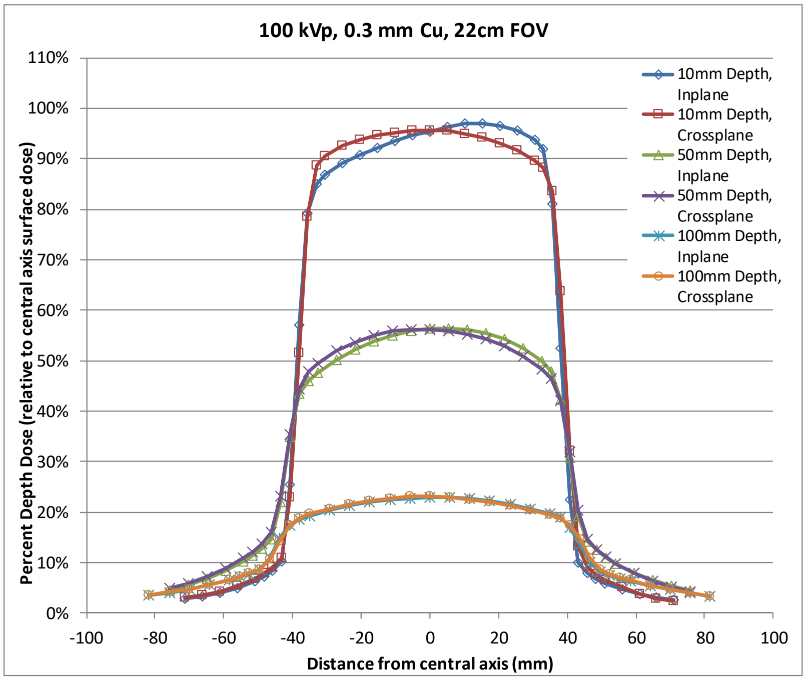

Figure 5-27. Fluoroscopic X-ray beam profiles for 100 kVp, 0.3 mm Cu filtration, in the 22 cm FOV.

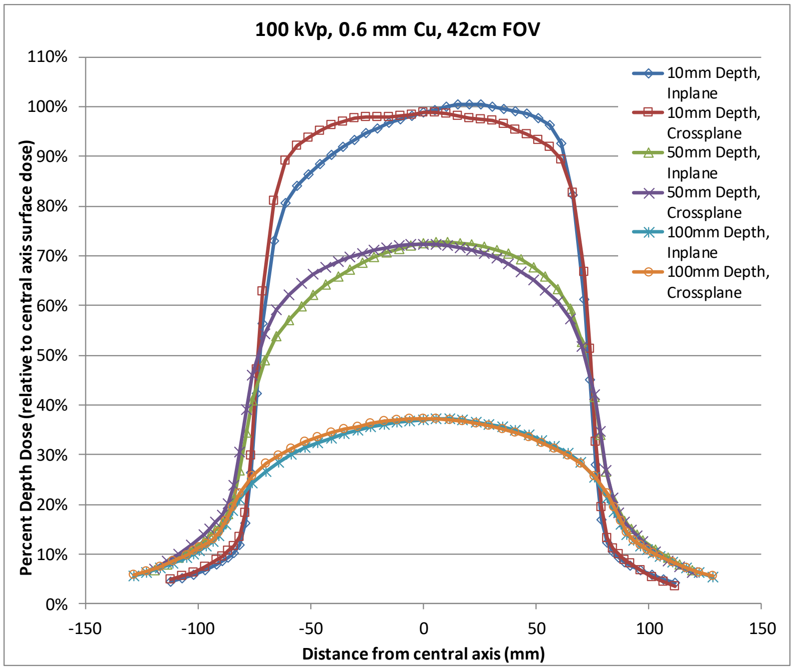

Figure 5-28. Fluoroscopic X-ray beam profiles for 100 kVp, 0.6 mm Cu filtration, in the 42 cm FOV.

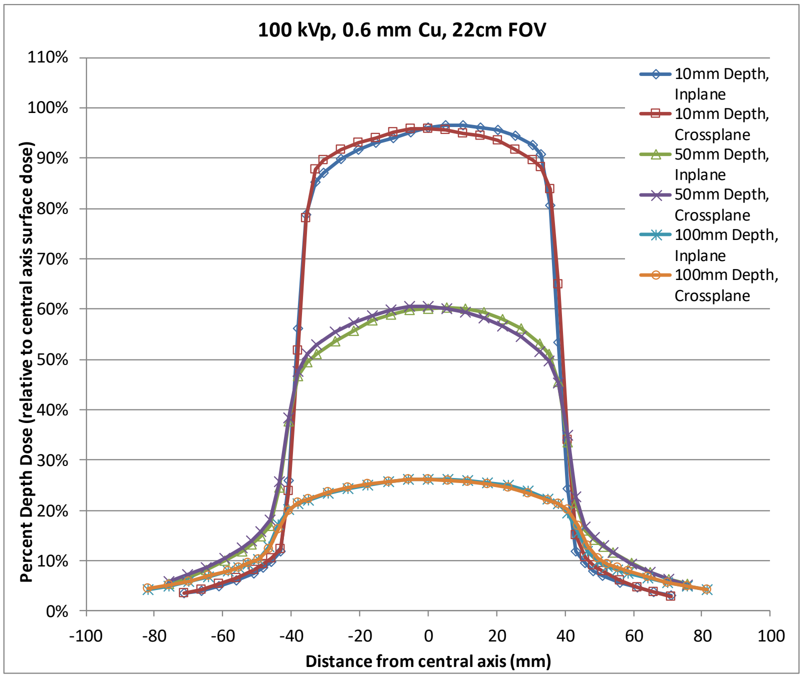

Figure 5-29. Fluoroscopic X-ray beam profiles for 100 kVp, 0.6 mm Cu filtration, in the 22 cm FOV.

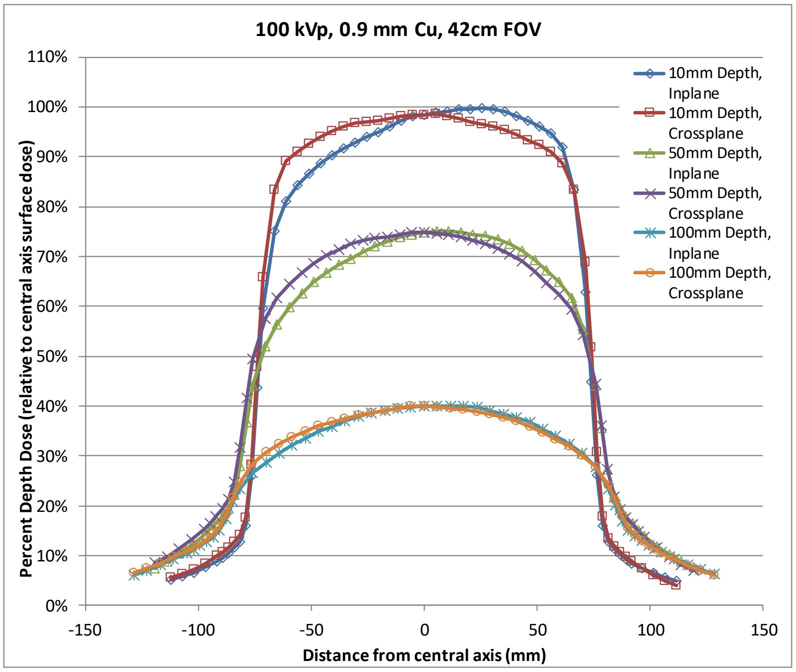

Figure 5-30. Fluoroscopic X-ray beam profiles for 100 kVp, 0.9 mm Cu filtration, in the 42 cm FOV.

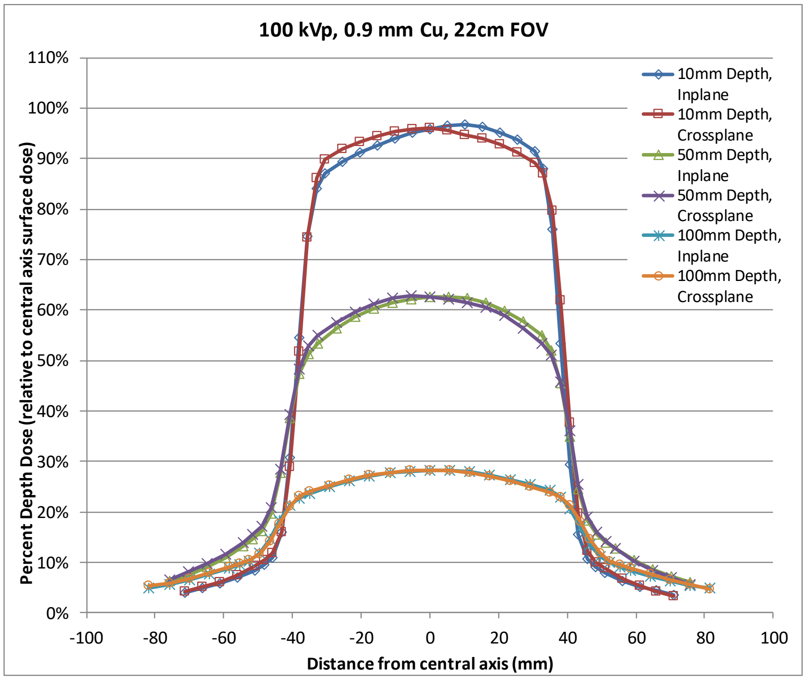

Figure 5-31. Fluoroscopic X-ray beam profiles for 100 kVp, 0.9 mm Cu filtration, in the 22 cm FOV.

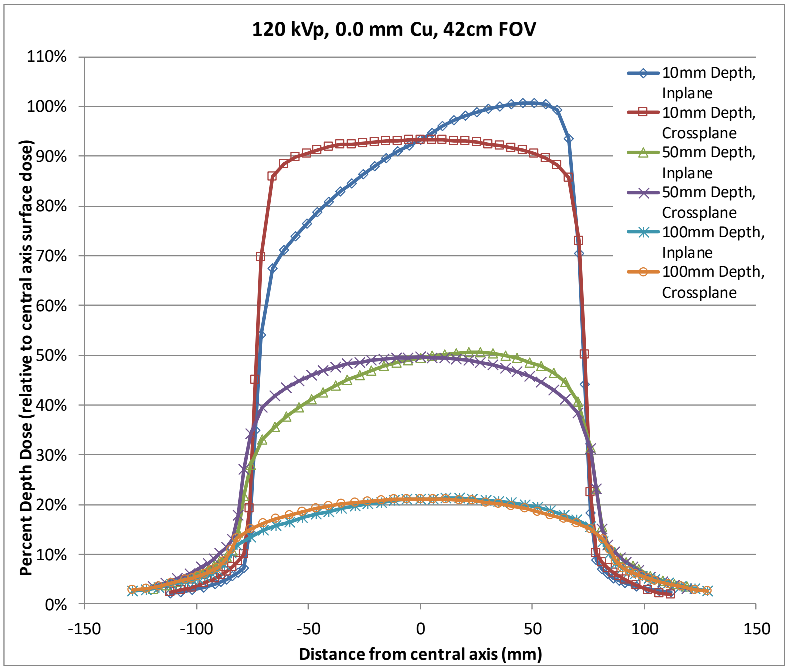

Figure 5-32. Fluoroscopic X-ray beam profiles for 120 kVp, no filtration, in the 42 cm FOV.

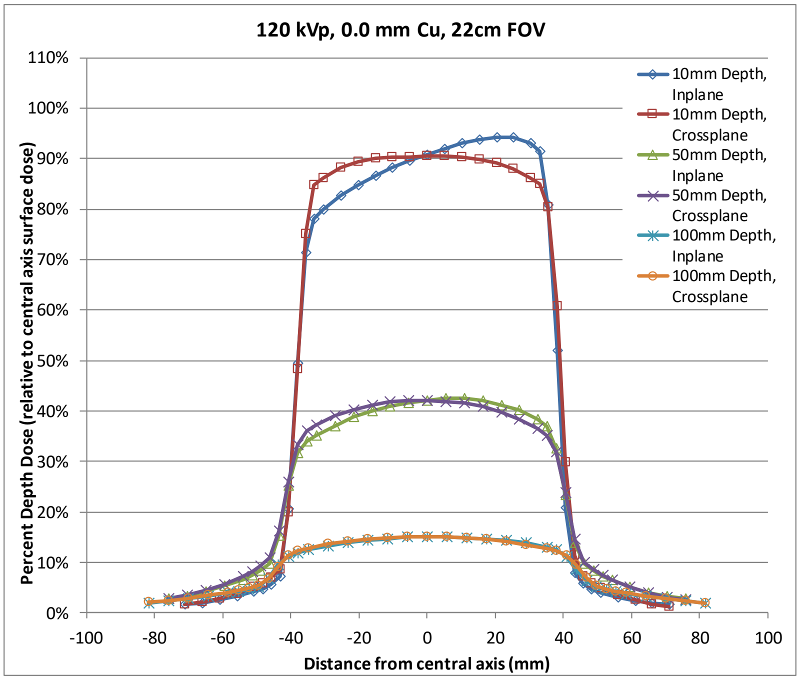

Figure 5-33. Fluoroscopic X-ray beam profiles for 120 kVp, no filtration, in the 22 cm FOV.

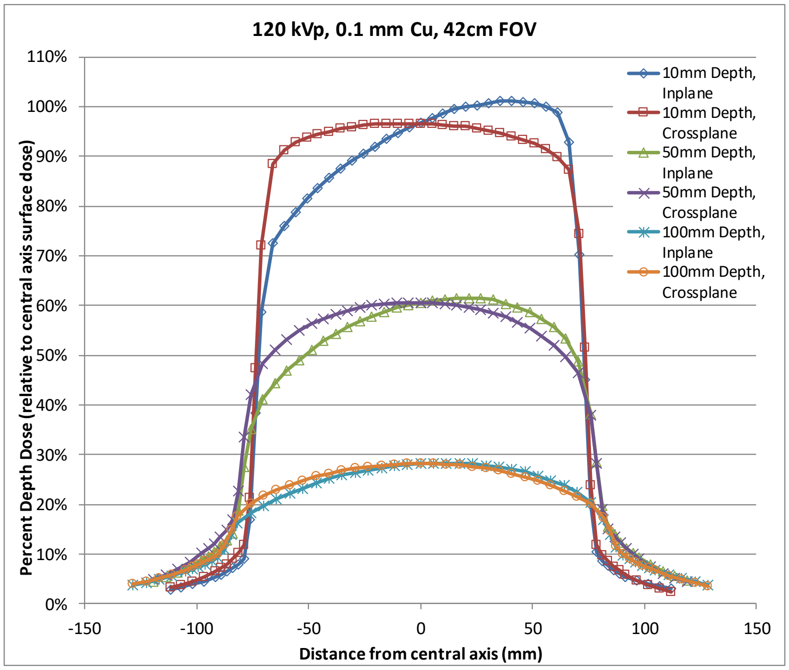

Figure 5-34. Fluoroscopic X-ray beam profiles for 120 kVp, 0.1 mm Cu filtration, in the 42 cm FOV.

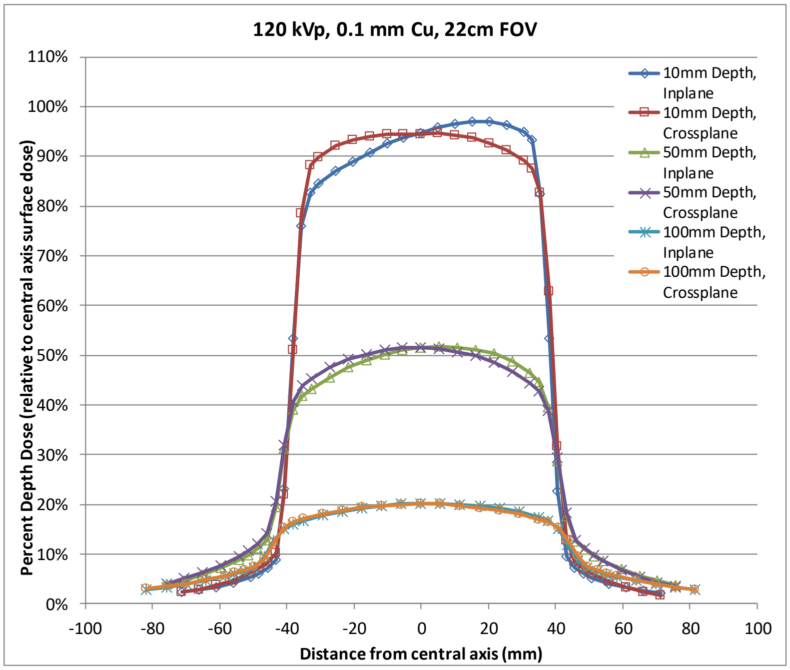

Figure 5-35. Fluoroscopic X-ray beam profiles for 120 kVp, 0.1 mm Cu filtration, in the 22 cm FOV.

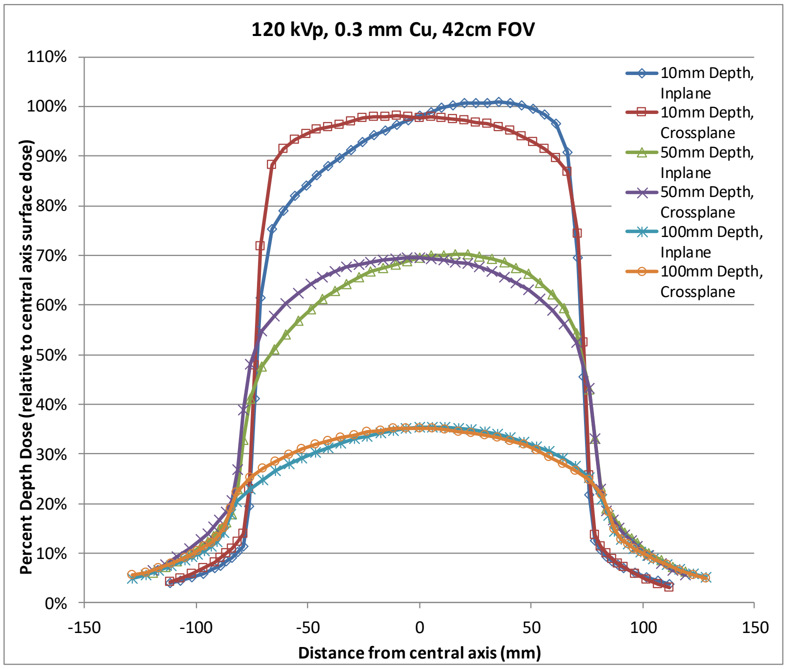

Figure 5-36. Fluoroscopic X-ray beam profiles for 120 kVp, 0.3 mm Cu filtration, in the 42 cm FOV.

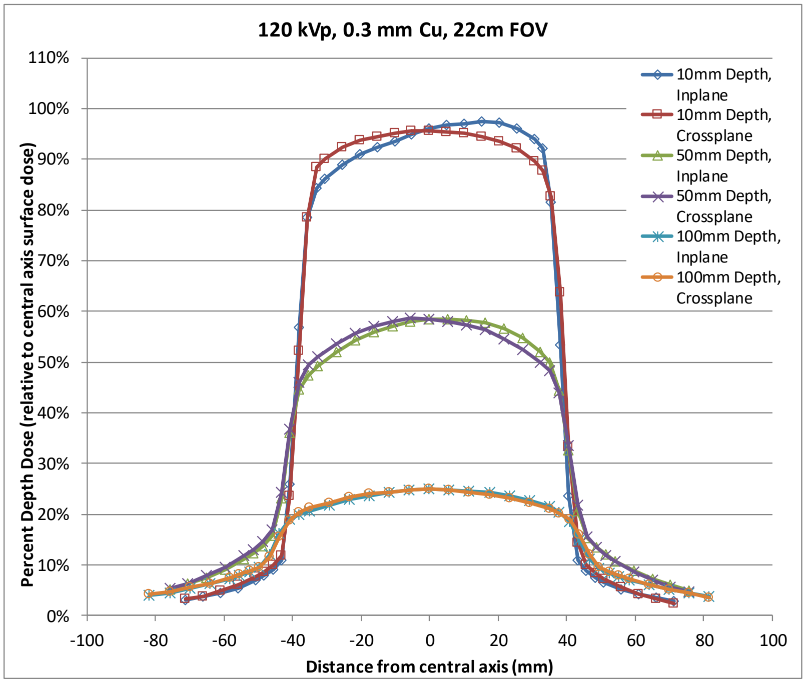

Figure 5-37. Fluoroscopic X-ray beam profiles for 120 kVp, 0.3 mm Cu filtration, in the 22 cm FOV.

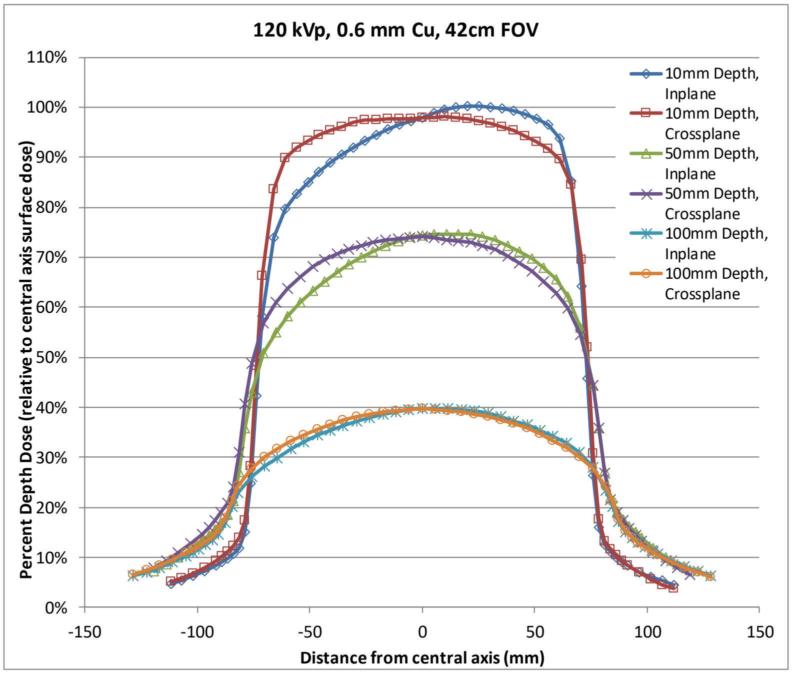

Figure 5-38. Fluoroscopic X-ray beam profiles for 120 kVp, 0.6 mm Cu filtration, in the 42 cm FOV.

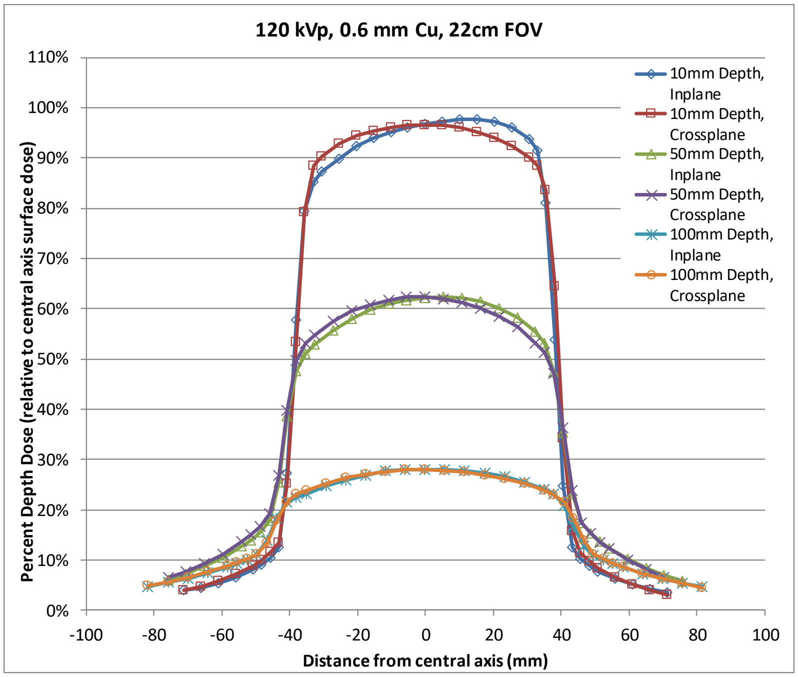

Figure 5-39. Fluoroscopic X-ray beam profiles for 120 kVp, 0.6 mm Cu filtration, in the 22 cm FOV.

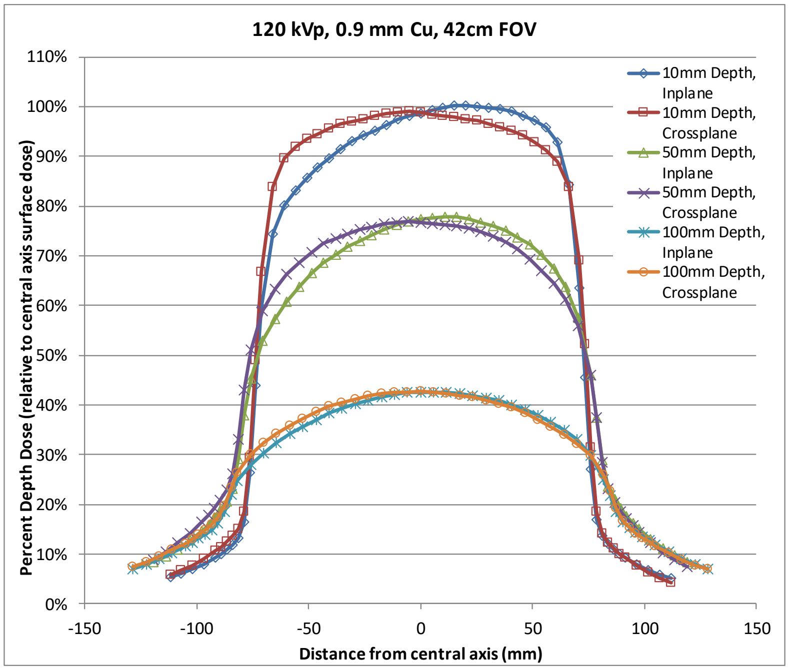

Figure 5-40. Fluoroscopic X-ray beam profiles for 120 kVp, 0.9 mm Cu filtration, in the 42 cm FOV.

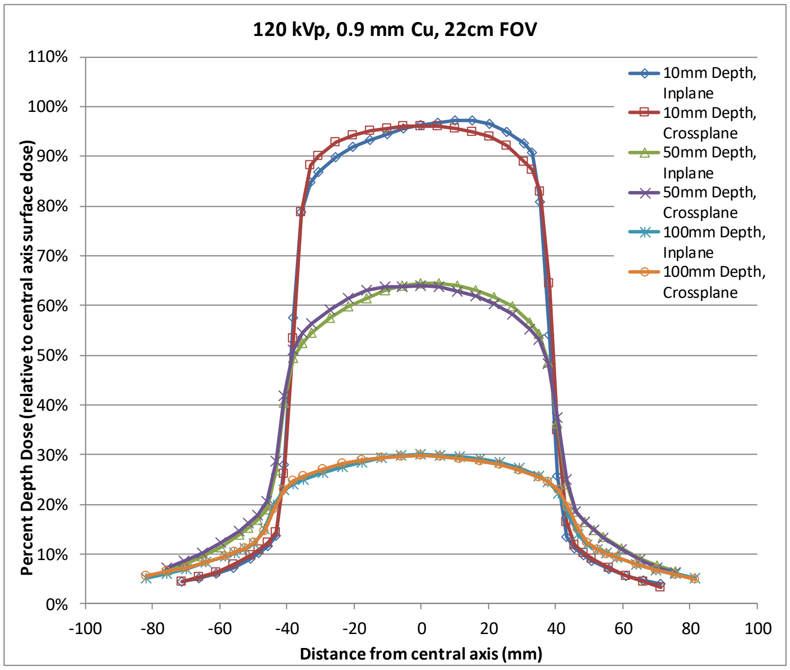

Figure 5-41. Fluoroscopic X-ray beam profiles for 120 kVp, 0.9 mm Cu filtration, in the 22 cm FOV.

5.4 Discussion

Because of the potential for large energy dependencies of solid state detectors, PDDs for the diode detector used for the profile measurements were compared to PDDs from a Spokas ionization chamber, a chamber known to yield reliable results in the diagnostic energy range.[43] The comparison indicated very good agreement at the lowest and highest kVps with PDD differences of less than 2.5%.

An interesting phenomenon was observed with respect to the heel effect, whereby the magnitude of the heel effect varied substantially with depth in water. In the figures for the large FOV and beam qualities without Cu filtration (Figures 5-2, 5-12, 5-22, and 5-32), the heel effect is well pronounced at 10-mm depth, substantially reduced at 50-mm depth, and nearly eliminated by 100-mm depth. This phenomenon can likely be attributed to two different effects. First, the heel effect represents a 2-dimensional distribution of X-ray energies and dose. The cathode side of the in-plane measurements results in a higher dose magnitude, partially because of the higher number of low-energy photons in that region of the X-ray beam. As the X-ray beam passes through the water, those lower-energy photons are preferentially absorbed, diminishing the magnitude of the heel effect with depth in water. Second, the natural increase in the X-ray scatter-to-primary ratio with depth in water likely overwhelms the diminished heel effect.

The X-ray beam profiles illustrate radiation dose as a percentage of the central-axis maximum dose. The out-of-field percent doses vary substantially with respect to beam energy and X-ray field size, as would be anticipated. Ongoing work related to this investigation includes

1. The generation of clinically useful tables for out-of-field dose fractions based on beam quality and field size. The likely configuration of these tables will provide distances from edges of the X-ray beam (using either full-width-half-maximum or -tenth-maximum values) and percent of central-axis maximum value.
2. Assessment of how (or if) the fluoroscope manufacturers are performing “flat field” gain corrections for images and to what extent the heel effect is present when those calibrations are performed.
3. Investigation of the potential use of thin wedge filters to curb the contribution of the heel effect to the surface dose.

CHAPTER 6 SUMMARY OF WORK AND FUTURE DIRECTIONS

The work presented in chapters 2 through 5 provides a base of research that has been lacking regarding dosimetry and characterizations of X-ray beam qualities used by current-generation interventional fluoroscopes. The work is necessary to refine and enhance dosimetry from these X-ray beam qualities, providing a substantial improvement in the accuracy of radiation dose estimates at the surface of the patient (from corrections to the reported $K_{a,r}$) and the deposition of that dose through the patient.

Future work expanding on this foundation will focus on mapping the dose reported by the system using the DICOM Radiation Dose Structured Report for C-arm positional and radiation output information in conjunction with external imaging or hybrid patient models such as those created by researchers at the University of Florida.[49] This will provide a better estimate of the 2-dimensional dose distribution at the surface of the patient. With the use of the PDDs determined in the present work, the dose distribution through the patient can then be mapped. Additional work will be needed to address inhomogeneities within soft tissue and other tissue types within the patient. Additional work is also needed to address the use of multiple procedures, which often occurs in complex interventional procedures, and the combined radiation dose distribution in such cases.

APPENDIX A

DEVIATION DUE TO DIFFERENCES IN FLOOR-TO-TABLE HEIGHT

The approximately 5% geometric deviation indicated in the text was calculated using the data from the unit with the largest floor-to-table height distance; these data were then adjusted to represent that system at the same table height as the shortest floor-to-table distance (90 cm, from Table 2-2):

$$\boldsymbol{Dev} = \left(\frac{\frac{SID_{table\ new\ height}}{SSD_{table\ new\ height}}}{\frac{SID_{table\ initial\ height}}{SSD_{table\ initial\ height}}}\right)^{2} = \left(\frac{\frac{(New\ table\ height - floor\ to\ focal\ spot\ dis) + phantom\ thickness}{New\ table\ height - floor\ to\ focal\ spot\ dis}}{\frac{(Initial\ table\ height - floor\ to\ focal\ spot\ dis) + phantom\ thickness}{Initial\ table\ height - floor\ to\ focal\ spot\ dis}}\right)^{2} =$$

$$\left(\frac{\frac{(90-31)+35.6}{(90-31)}}{\frac{63.5+35.6}{63.5}}\right)^{2} = \left(\frac{1.603}{1.561}\right)^{2} = \mathbf{1.05}$$

APPENDIX B

PDD DATA TABLES

Table B-1. PDDs for 60 kVp, 16 cm × 16 cm at SSD (42 cm nominal FOV).

Effective depth of measurement in water (mm)	0.0 mm Cu	0.1 mm Cu	0.3 mm Cu	0.6 mm Cu	0.9 mm Cu*
1	1.000	1.000	1.000	0.981	0.989
2	0.998	0.999	0.997	0.981	1.000
3	0.983	0.991	0.995	0.984	0.998
4	0.964	0.986	0.998	1.000	0.993
5	0.946	0.975	0.992	0.981	0.994
6	0.926	0.965	0.984	0.988	0.996
7	0.904	0.953	0.978	0.976	0.989
8	0.886	0.941	0.970	0.972	0.981
9	0.866	0.929	0.961	0.951	0.980
10	0.848	0.916	0.953	0.955	0.976
11	0.826	0.901	0.947	0.953	0.967
16	0.733	0.831	0.891	0.908	0.925
21	0.651	0.766	0.839	0.860	0.881
26	0.575	0.697	0.773	0.805	0.832
31	0.510	0.631	0.723	0.756	0.781
36	0.451	0.576	0.665	0.701	0.733
41	0.400	0.520	0.612	0.659	0.685
46	0.354	0.471	0.561	0.603	0.639
51	0.316	0.424	0.512	0.556	0.598
61	0.248	0.345	0.430	0.473	0.515
71	0.195	0.279	0.355	0.397	0.438
81	0.154	0.225	0.293	0.335	0.376
91	0.122	0.182	0.241	0.280	0.319
101	0.097	0.147	0.197	0.230	0.266
111	0.077	0.118	0.162	0.195	0.222
121	0.061	0.095	0.132	0.162	0.188
131	0.048	0.076	0.109	0.135	0.159
141	0.039	0.062	0.089	0.110	0.135
151	0.031	0.050	0.073	0.093	0.116

*Smoothed using PTW 3-point smoothing algorithm integrated into the PTW MEDPHYSTO software.

Table B-2. PDDs for 60 kVp, 8 cm × 8 cm at SSD (22 cm nominal FOV).

Effective depth of measurement in water (mm)	**0.0 mm Cu**	**0.1 mm Cu**	**0.3 mm Cu**	**0.6 mm Cu**	**0.9 mm Cu***
1	1.000	1.000	1.000	1.000	0.990
2	0.994	0.998	0.990	0.997	0.994
3	0.978	0.989	0.994	0.997	0.997
4	0.955	0.976	0.979	0.995	1.000
5	0.936	0.967	0.975	0.992	0.999
6	0.913	0.951	0.967	0.981	0.991
7	0.890	0.943	0.962	0.967	0.978
8	0.870	0.925	0.952	0.965	0.964
9	0.850	0.909	0.943	0.957	0.953
10	0.828	0.895	0.929	0.949	0.943
11	0.806	0.877	0.916	0.936	0.932
16	0.707	0.803	0.854	0.885	0.876
21	0.618	0.725	0.795	0.811	0.819
26	0.541	0.654	0.718	0.759	0.762
31	0.473	0.587	0.661	0.701	0.707
36	0.413	0.524	0.601	0.647	0.653
41	0.359	0.467	0.546	0.601	0.601
46	0.314	0.416	0.492	0.544	0.551
51	0.276	0.371	0.446	0.489	0.506
61	0.211	0.294	0.357	0.404	0.424
71	0.162	0.231	0.292	0.327	0.353
81	0.125	0.182	0.236	0.273	0.292
91	0.096	0.144	0.189	0.222	0.241
101	0.074	0.113	0.152	0.182	0.198
111	0.057	0.089	0.121	0.152	0.163
121	0.044	0.070	0.098	0.120	0.133
131	0.035	0.055	0.079	0.099	0.108
141	0.027	0.044	0.064	0.083	0.086
151	0.021	0.035	0.051	0.067	0.068

*Smoothed using PTW 3-point smoothing algorithm integrated into the PTW MEDPHYSTO software.

Table B-3. PDDs for 60 kVp, 4 cm × 4 cm at SSD (11 cm nominal FOV).

Effective depth of measurement in water (mm)	**0.0 mm Cu**	**0.1 mm Cu**	**0.3 mm Cu**	**0.6 mm Cu***	**0.9 mm Cu***
1	1.000	1.000	1.000	1.000	1.000
2	0.983	0.989	0.997	0.987	0.992
3	0.952	0.977	0.973	0.973	0.984
4	0.928	0.960	0.967	0.962	0.976
5	0.908	0.942	0.946	0.953	0.966
6	0.881	0.925	0.942	0.941	0.956
7	0.857	0.908	0.923	0.927	0.946
8	0.833	0.891	0.909	0.912	0.939
9	0.808	0.873	0.892	0.898	0.932
10	0.786	0.854	0.874	0.883	0.925
11	0.764	0.834	0.873	0.868	0.913
16	0.651	0.745	0.793	0.795	0.844
21	0.560	0.660	0.710	0.723	0.773
26	0.478	0.582	0.639	0.657	0.704
31	0.411	0.513	0.570	0.601	0.638
36	0.352	0.450	0.504	0.554	0.577
41	0.303	0.395	0.451	0.508	0.522
46	0.260	0.345	0.401	0.457	0.472
51	0.223	0.304	0.357	0.408	0.430
61	0.166	0.235	0.279	0.324	0.357
71	0.124	0.181	0.220	0.257	0.293
81	0.093	0.139	0.174	0.205	0.239
91	0.070	0.107	0.136	0.163	0.194
101	0.053	0.082	0.107	0.129	0.157
111	0.040	0.064	0.083	0.103	0.127
121	0.031	0.049	0.066	0.082	0.102
131	0.024	0.038	0.052	0.066	0.081
141	0.018	0.030	0.042	0.053	0.062
151	0.014	0.023	0.033	0.042	0.047

*Smoothed using PTW 3-point smoothing algorithm integrated into the PTW MEDPHYSTO software.

Table B-4. PDDs for 70 kVp, 8 cm × 8 cm at SSD (22 cm nominal FOV).

Effective depth of measurement in water (mm)	0.0 mm Cu	0.3 mm Cu	0.9 mm Cu*
1	1.000	0.999	1.000
2	0.990	1.000	0.998
3	0.972	0.992	0.995
4	0.959	0.990	0.992
5	0.939	0.984	0.989
6	0.925	0.973	0.984
7	0.907	0.972	0.977
8	0.888	0.959	0.971
9	0.865	0.958	0.965
10	0.851	0.935	0.959
11	0.828	0.926	0.950
16	0.740	0.875	0.897
21	0.660	0.808	0.845
26	0.585	0.750	0.792
31	0.520	0.692	0.737
36	0.459	0.641	0.682
41	0.407	0.578	0.631
46	0.362	0.531	0.583
51	0.320	0.482	0.538
61	0.251	0.401	0.455
71	0.198	0.328	0.381
81	0.156	0.268	0.318
91	0.123	0.218	0.266
101	0.097	0.179	0.221
111	0.077	0.146	0.183
121	0.061	0.118	0.151
131	0.049	0.097	0.126
141	0.039	0.078	0.103
151	0.031	0.064	0.082

*Smoothed using PTW 3-point smoothing algorithm integrated into the PTW MEDPHYSTO software.

Table B-5. PDDs for 80 kVp, 16 cm × 16 cm at SSD (42 cm nominal FOV).

Effective depth of measurement in water (mm)	0.0 mm Cu	0.1 mm Cu	0.3 mm Cu	0.6 mm Cu	0.9 mm Cu
1	1.000	0.997	0.994	0.985	1.000
2	0.997	1.000	0.999	0.987	0.990
3	0.986	0.997	0.995	0.996	0.991
4	0.977	0.993	1.000	1.000	0.996
5	0.964	0.987	0.999	0.999	0.995
6	0.951	0.984	0.993	0.991	0.982
7	0.935	0.974	0.986	0.991	0.996
8	0.921	0.967	0.985	0.986	0.988
9	0.906	0.958	0.975	0.984	0.983
10	0.893	0.951	0.973	0.982	0.980
11	0.877	0.936	0.970	0.974	0.975
16	0.801	0.884	0.924	0.936	0.944
21	0.729	0.828	0.876	0.901	0.899
26	0.663	0.769	0.830	0.856	0.869
31	0.602	0.712	0.781	0.805	0.818
36	0.546	0.660	0.729	0.756	0.774
41	0.495	0.608	0.683	0.715	0.729
46	0.449	0.560	0.633	0.670	0.684
51	0.408	0.514	0.589	0.624	0.638
61	0.334	0.434	0.505	0.542	0.561
71	0.275	0.363	0.430	0.468	0.487
81	0.226	0.304	0.367	0.401	0.418
91	0.185	0.253	0.309	0.343	0.360
101	0.152	0.211	0.261	0.294	0.309
111	0.125	0.175	0.219	0.248	0.262
121	0.103	0.146	0.185	0.209	0.224
131	0.085	0.121	0.155	0.179	0.192
141	0.070	0.101	0.130	0.152	0.163
151	0.057	0.083	0.110	0.127	0.139

Table B-6. PDDs for 80 kVp, 8 cm × 8 cm at SSD (22 cm nominal FOV).

Effective depth of measurement in water (mm)	**0.0 mm Cu**	**0.1 mm Cu**	**0.3 mm Cu**	**0.6 mm Cu**	**0.9 mm Cu**
1	1.000	1.000	0.998	0.994	0.988
2	0.995	0.999	1.000	0.992	1.000
3	0.981	0.996	0.996	1.000	0.996
4	0.970	0.988	0.997	0.991	0.996
5	0.956	0.981	0.990	0.996	0.990
6	0.936	0.971	0.984	0.992	0.996
7	0.920	0.962	0.974	0.978	0.984
8	0.907	0.952	0.969	0.977	0.978
9	0.884	0.938	0.956	0.966	0.974
10	0.871	0.929	0.950	0.958	0.951
11	0.851	0.914	0.944	0.956	0.957
16	0.766	0.853	0.893	0.903	0.912
21	0.687	0.784	0.838	0.859	0.862
26	0.616	0.717	0.775	0.798	0.810
31	0.552	0.657	0.718	0.750	0.750
36	0.494	0.597	0.661	0.688	0.703
41	0.441	0.543	0.608	0.635	0.647
46	0.393	0.491	0.555	0.589	0.603
51	0.350	0.444	0.507	0.539	0.553
61	0.279	0.363	0.425	0.453	0.471
71	0.223	0.296	0.353	0.380	0.397
81	0.178	0.240	0.293	0.321	0.337
91	0.142	0.197	0.239	0.266	0.278
101	0.114	0.159	0.198	0.222	0.236
111	0.092	0.129	0.163	0.185	0.197
121	0.073	0.105	0.134	0.152	0.163
131	0.059	0.085	0.110	0.127	0.137
141	0.047	0.069	0.091	0.106	0.114
151	0.038	0.056	0.074	0.087	0.095

Table B-7. PDDs for 80 kVp, 4 cm × 4 cm at SSD (11 cm nominal FOV).

Effective depth of measurement in water (mm)	**0.0 mm Cu**	**0.1 mm Cu**	**0.3 mm Cu**	**0.6 mm Cu**	**0.9 mm Cu***
1	1.000	1.000	0.999	1.000	1.000
2	0.984	0.994	1.000	0.991	1.000
3	0.967	0.978	0.994	0.989	0.996
4	0.945	0.968	0.981	0.971	0.989
5	0.927	0.953	0.985	0.973	0.981
6	0.908	0.938	0.963	0.964	0.972
7	0.888	0.926	0.954	0.953	0.962
8	0.867	0.912	0.941	0.942	0.950
9	0.846	0.891	0.931	0.929	0.936
10	0.825	0.885	0.916	0.913	0.926
11	0.806	0.863	0.901	0.900	0.915
16	0.709	0.785	0.829	0.839	0.852
21	0.623	0.706	0.759	0.767	0.789
26	0.548	0.635	0.688	0.702	0.726
31	0.480	0.568	0.626	0.640	0.664
36	0.421	0.506	0.566	0.591	0.604
41	0.369	0.452	0.509	0.530	0.550
46	0.324	0.404	0.461	0.481	0.501
51	0.286	0.357	0.416	0.435	0.456
61	0.221	0.283	0.337	0.356	0.379
71	0.171	0.226	0.270	0.288	0.312
81	0.133	0.180	0.219	0.237	0.255
91	0.104	0.142	0.175	0.190	0.208
101	0.082	0.113	0.142	0.156	0.170
111	0.064	0.090	0.113	0.128	0.139
121	0.050	0.072	0.092	0.103	0.115
131	0.040	0.057	0.074	0.086	0.094
141	0.032	0.046	0.060	0.068	0.076
151	0.025	0.036	0.048	0.055	0.060

*Smoothed using PTW 3-point smoothing algorithm integrated into the PTW MEDPHYSTO software.

Table B-8. PDDs for 100 kVp, 16 cm × 16 cm at SSD (42 cm nominal FOV).

Effective depth of measurement in water (mm)	0.0 mm Cu	0.1 mm Cu	0.3 mm Cu	0.6 mm Cu	0.9 mm Cu
1	1.000	0.993	1.000	0.997	0.990
2	0.999	1.000	0.998	0.996	0.994
3	0.991	0.997	1.000	0.999	0.995
4	0.984	0.993	0.999	0.997	0.995
5	0.973	0.990	0.997	1.000	0.998
6	0.962	0.987	1.000	1.000	1.000
7	0.953	0.982	0.997	0.997	0.999
8	0.939	0.973	0.993	0.986	0.991
9	0.926	0.965	0.990	0.987	0.982
10	0.914	0.959	0.980	0.987	0.985
11	0.901	0.950	0.972	0.975	0.983
16	0.840	0.904	0.939	0.947	0.956
21	0.775	0.855	0.893	0.908	0.912
26	0.716	0.801	0.852	0.869	0.876
31	0.657	0.749	0.807	0.827	0.836
36	0.606	0.702	0.760	0.779	0.790
41	0.556	0.651	0.715	0.733	0.747
46	0.511	0.605	0.666	0.691	0.706
51	0.466	0.561	0.624	0.653	0.660
61	0.393	0.479	0.542	0.569	0.584
71	0.330	0.409	0.468	0.494	0.510
81	0.276	0.348	0.402	0.429	0.445
91	0.231	0.294	0.346	0.370	0.385
101	0.193	0.249	0.295	0.319	0.334
111	0.161	0.209	0.250	0.274	0.287
121	0.135	0.177	0.214	0.234	0.247
131	0.113	0.148	0.181	0.200	0.210
141	0.094	0.125	0.154	0.169	0.181
151	0.079	0.106	0.129	0.146	0.155

Table B-9. PDDs for 100 kVp, 8 cm × 8 cm at SSD (22 cm nominal FOV).

Effective depth of measurement in water (mm)	0.0 mm Cu	0.1 mm Cu	0.3 mm Cu	0.6 mm Cu	0.9 mm Cu
1	1.000	1.000	1.000	0.996	0.992
2	0.995	1.000	0.998	0.997	0.999
3	0.985	0.995	0.999	1.000	1.000
4	0.975	0.992	0.996	0.997	0.994
5	0.961	0.982	0.989	0.989	0.989
6	0.949	0.975	0.987	0.988	0.983
7	0.936	0.971	0.975	0.977	0.980
8	0.922	0.959	0.974	0.973	0.973
9	0.906	0.951	0.967	0.966	0.970
10	0.892	0.938	0.955	0.960	0.959
11	0.877	0.927	0.947	0.953	0.951
16	0.801	0.870	0.897	0.911	0.910
21	0.731	0.810	0.849	0.856	0.862
26	0.663	0.748	0.793	0.807	0.819
31	0.602	0.689	0.738	0.756	0.766
36	0.544	0.634	0.682	0.700	0.707
41	0.492	0.580	0.631	0.649	0.658
46	0.443	0.530	0.583	0.604	0.618
51	0.401	0.485	0.534	0.558	0.572
61	0.327	0.402	0.453	0.476	0.487
71	0.266	0.332	0.380	0.402	0.412
81	0.216	0.275	0.318	0.340	0.349
91	0.176	0.226	0.265	0.284	0.295
101	0.144	0.187	0.221	0.241	0.248
111	0.117	0.154	0.184	0.201	0.210
121	0.096	0.127	0.153	0.168	0.177
131	0.078	0.104	0.127	0.140	0.148
141	0.064	0.086	0.105	0.117	0.124
151	0.053	0.071	0.088	0.098	0.105

Table B-10. PDDs for 100 kVp, 4 cm × 4 cm at SSD (11 cm nominal FOV).

Effective depth of measurement in water (mm)	**0.0 mm Cu**	**0.1 mm Cu**	**0.3 mm Cu**	**0.6 mm Cu**	**0.9 mm Cu**
1	1.000	1.000	1.000	1.000	1.000
2	0.995	0.993	0.996	0.994	0.997
3	0.976	0.982	0.991	0.994	0.989
4	0.961	0.975	0.983	0.989	0.981
5	0.945	0.965	0.970	0.984	0.975
6	0.929	0.954	0.962	0.963	0.962
7	0.910	0.938	0.949	0.953	0.956
8	0.893	0.924	0.938	0.947	0.946
9	0.874	0.910	0.924	0.931	0.935
10	0.856	0.894	0.913	0.916	0.919
11	0.837	0.880	0.905	0.911	0.906
16	0.749	0.808	0.837	0.848	0.847
21	0.668	0.733	0.768	0.784	0.785
26	0.595	0.667	0.702	0.719	0.729
31	0.527	0.599	0.641	0.656	0.668
36	0.469	0.540	0.582	0.602	0.616
41	0.415	0.486	0.530	0.544	0.556
46	0.369	0.438	0.480	0.498	0.506
51	0.329	0.391	0.432	0.456	0.462
61	0.259	0.316	0.357	0.375	0.384
71	0.205	0.255	0.290	0.309	0.317
81	0.163	0.205	0.237	0.252	0.262
91	0.130	0.166	0.192	0.208	0.216
101	0.104	0.134	0.157	0.170	0.180
111	0.083	0.108	0.128	0.141	0.146
121	0.066	0.088	0.105	0.115	0.121
131	0.053	0.071	0.085	0.094	0.100
141	0.043	0.057	0.070	0.077	0.083
151	0.034	0.046	0.057	0.064	0.067

Table B-11. PDDs for 120 kVp, 16 cm × 16 cm at SSD (42 cm nominal FOV).

Effective depth of measurement in water (mm)	**0.0 mm Cu**	**0.1 mm Cu**	**0.3 mm Cu**	**0.6 mm Cu**	**0.9 mm Cu**
1	1.000	0.997	0.991	0.986	0.993
2	1.000	0.999	0.992	0.990	0.997
3	0.995	1.000	0.999	0.995	0.997
4	0.987	0.999	1.000	0.997	1.000
5	0.981	0.997	0.996	0.996	0.996
6	0.972	0.990	0.994	1.000	0.996
7	0.966	0.988	0.992	0.993	0.999
8	0.955	0.981	0.985	0.992	0.990
9	0.945	0.974	0.985	0.987	0.990
10	0.934	0.967	0.981	0.979	0.987
11	0.925	0.962	0.975	0.978	0.977
16	0.866	0.921	0.940	0.948	0.955
21	0.811	0.875	0.902	0.911	0.909
26	0.753	0.824	0.860	0.872	0.881
31	0.702	0.777	0.814	0.827	0.841
36	0.650	0.729	0.767	0.783	0.793
41	0.602	0.681	0.726	0.742	0.750
46	0.557	0.638	0.681	0.700	0.710
51	0.515	0.593	0.639	0.660	0.668
61	0.438	0.513	0.560	0.580	0.595
71	0.373	0.442	0.488	0.510	0.521
81	0.317	0.378	0.422	0.443	0.459
91	0.267	0.324	0.363	0.386	0.398
101	0.227	0.277	0.312	0.333	0.346
111	0.192	0.235	0.268	0.288	0.300
121	0.161	0.200	0.231	0.248	0.256
131	0.136	0.170	0.196	0.213	0.222
141	0.115	0.144	0.168	0.183	0.191
151	0.097	0.122	0.143	0.158	0.166

Table B-12. PDDs for 120 kVp, 8 cm × 8 cm at SSD (22 cm nominal FOV).

Effective depth of measurement in water (mm)	**0.0 mm Cu**	**0.1 mm Cu**	**0.3 mm Cu**	**0.6 mm Cu**	**0.9 mm Cu**
1	1.000	1.000	1.000	1.000	0.997
2	0.998	1.000	0.998	0.998	1.000
3	0.989	0.995	0.999	0.999	0.996
4	0.979	0.995	0.995	0.997	0.995
5	0.970	0.991	0.991	0.994	0.997
6	0.957	0.982	0.985	0.987	0.990
7	0.948	0.974	0.980	0.982	0.979
8	0.934	0.964	0.974	0.975	0.977
9	0.921	0.956	0.966	0.969	0.974
10	0.907	0.947	0.961	0.967	0.963
11	0.896	0.938	0.952	0.959	0.960
16	0.827	0.887	0.908	0.911	0.915
21	0.758	0.828	0.853	0.868	0.866
26	0.696	0.768	0.801	0.816	0.824
31	0.635	0.713	0.747	0.764	0.770
36	0.581	0.659	0.695	0.715	0.717
41	0.529	0.605	0.646	0.664	0.670
46	0.482	0.555	0.597	0.617	0.626
51	0.438	0.511	0.552	0.572	0.584
61	0.361	0.427	0.468	0.489	0.499
71	0.297	0.357	0.397	0.415	0.425
81	0.245	0.298	0.335	0.353	0.362
91	0.201	0.248	0.279	0.297	0.307
101	0.166	0.205	0.234	0.252	0.261
111	0.137	0.171	0.196	0.213	0.220
121	0.113	0.142	0.165	0.179	0.185
131	0.093	0.118	0.137	0.150	0.157
141	0.077	0.098	0.115	0.126	0.132
151	0.064	0.082	0.096	0.107	0.112

Table B-13. PDDs for 120 kVp, 4 cm × 4 cm at SSD (11 cm nominal FOV).

Effective depth of measurement in water (mm)	**0.0 mm Cu**	**0.1 mm Cu**	**0.3 mm Cu**	**0.6 mm Cu**	**0.9 mm Cu**
1	1.000	1.000	1.000	1.000	1.000
2	0.989	0.999	0.999	0.993	0.995
3	0.976	0.985	0.990	0.992	0.988
4	0.965	0.978	0.992	0.981	0.979
5	0.948	0.968	0.975	0.975	0.973
6	0.935	0.956	0.965	0.968	0.964
7	0.918	0.943	0.957	0.954	0.953
8	0.902	0.933	0.945	0.942	0.941
9	0.882	0.922	0.936	0.931	0.936
10	0.867	0.908	0.920	0.923	0.921
11	0.851	0.895	0.910	0.912	0.911
16	0.769	0.821	0.845	0.848	0.858
21	0.694	0.750	0.781	0.789	0.791
26	0.624	0.686	0.716	0.727	0.731
31	0.558	0.623	0.661	0.665	0.670
36	0.499	0.563	0.599	0.611	0.617
41	0.448	0.509	0.547	0.556	0.562
46	0.399	0.460	0.495	0.508	0.517
51	0.358	0.416	0.451	0.464	0.475
61	0.287	0.337	0.371	0.386	0.394
71	0.230	0.275	0.305	0.320	0.328
81	0.185	0.224	0.251	0.266	0.272
91	0.149	0.182	0.206	0.218	0.226
101	0.120	0.148	0.169	0.181	0.185
111	0.097	0.121	0.139	0.150	0.154
121	0.078	0.099	0.114	0.124	0.128
131	0.064	0.080	0.094	0.102	0.106
141	0.052	0.066	0.078	0.084	0.088
151	0.042	0.054	0.064	0.070	0.074

APPENDIX C

PDDs FOR VALIDATION OF THE DIODE DETECTOR

Table C-1. PDDs for validation of the diode detector.

Depth (mm)	Spokas chamber PDD	Diode PDD	Difference in PDDs
0	100.0%	99.6%	0.4%
1	99.8%	99.9%	0.1%
2	98.9%	99.8%	0.9%
3	97.9%	100.0%	2.1%
4	97.0%	98.8%	1.8%
5	95.7%	97.1%	1.4%
6	94.8%	95.5%	0.7%
7	93.4%	93.8%	0.5%
8	92.1%	92.5%	0.4%
9	90.7%	90.8%	0.1%
10	89.6%	89.8%	0.2%
15	82.7%	82.1%	0.6%
20	75.8%	74.9%	0.9%
25	69.6%	68.2%	1.3%
30	63.5%	61.8%	1.7%
35	58.1%	56.5%	1.6%
40	52.9%	51.0%	1.9%
45	48.2%	46.1%	2.0%
50	43.8%	41.8%	2.0%
60	36.1%	33.9%	2.2%
70	29.7%	27.6%	2.1%
80	24.5%	22.5%	1.9%
90	20.1%	18.2%	1.9%
100	16.6%	14.9%	1.8%
110	13.7%	12.1%	1.7%
120	11.3%	9.9%	1.4%
130	9.3%	8.1%	1.3%
140	7.7%	6.7%	1.1%
150	6.4%	5.5%	0.9%

REFERENCES

1. Heupler, F., Wunderle, K. A., Shkumat, N., Cecil, R., and Kapadia, S., "Radiation safety in the cardiac catheterization laboratory," in *Cardiovascular Intervention: A Companion to Braunwald's Heart Disease*, edited by Bhatt, D. (Elsevier, Philadelphia, 2015).

2. Wunderle, K. and Gill, A., "Radiation-related injuries and their management: an update," Semin Intervent Radiol **32**, 156-162 (2015).

3. Balter, S., "Capturing patient doses from fluoroscopically based diagnostic and interventional systems," Health Phys **95**, 535-540 (2008).

4. Balter, S., *Interventional Fluoroscopy: Physics, Technology, and Safety* (Wiley-Liss, NY, 2001).

5. Joiner, M.C. and van der Kogel, A., *Basic Clinical Radiobiology, Fourth Edition* (CRC Press, Boca Raton, 2009).

6. Hall, E. J. and Giaccia, A. J., *Radiobiology for the Radiologist* (Lippincott Williams & Wilkins, Philadelphia, 2005).

7. "The 2007 recommendations of the International Commission on Radiological Protection," Ann ICRP **37**, 1-333 (2007).

8. Jones, A. K., Ensor, J. E., and Pasciak, A. S., "How accurately can the peak skin dose in fluoroscopy be determined using indirect dose metrics?" Med Phys **41**, 071913 (2014).

9. Miller, D. L., Balter, S., Schueler, B. A., Wagner, L. K., Strauss, K. J., and Vañó, E., "Clinical radiation management for fluoroscopically guided interventional procedures," Radiology **257**, 321-332 (2010).

10. Balter, S., Hopewell, J. W., Miller, D. L., and Wagner, L. K., "Fluoroscopically guided interventional procedures: a review of radiation effects on patients' skin and hair," Radiology **254**, 326-341 (2010).

11. Lopez Aventin D., Gil, I., Lopez González, D. M., and Pujol, R. M., "Chronic scalp ulceration as a late complication of fluoroscopically guided cerebral aneurysm embolization," Dermatology **224**, 198-203 (2012).

12. U. S. Department of Health and Human Services, "Common terminology criteria for adverse events (CTCAE), version 4.0," (June 2010).

13. Hymes, S. R., Strom, E. A., and Fife, C., "Radiation dermatitis: clinical presentation, pathophysiology, and treatment 2006," J Am Acad Dermatol **54**, 28-46 (2006).

14. Herold, D. M., Hanlon, A. L., and Hanks, G. E., "Diabetes mellitus: a predictor for late radiation morbidity," Int J Radiat Oncol Biol Phys **43**, 475-479 (1999).

15. Koenig, T. R., Wolff, D., Mettler, F. A., and Wagner, L.K., "Skin injuries from fluoroscopically guided procedures: part 1, characteristics of radiation injury," AJR Am J Roentgenol **177**, 3-11 (2001).

16. Geleijns, J. and Wondergem, J., "X-ray imaging and the skin: radiation biology, patient dosimetry and observed effects," Radiat Prot Dosimetry **114**, 121-125 (2005).

17. Wunderle, K. A. and Sands, M. J., "Radiation recall after a transarterial hepatic chemoembolization," J Vasc Interv Radiol **25**, 1027-1028 (2014).

18. Wunderle, K. A., Rakowski, J. T., and Dong, F. F., "Approaches to interventional fluoroscopic dose curves," J Appl Clin Med Phys **17**, 5788 (2016).

19. Wunderle, K. A., Rakowski, J. T., and Dong, F. F., "Effect of fluoroscopic X-ray beam spectrum on air-kerma measurement accuracy: implications for establishing correction coefficients on interventional fluoroscopes with KAP meters," J Appl Clin Med Phys **17**, 6092 (2016).

20. Wunderle, K., Godley, A., Shen, Z., Rakowski, J., and Dong, F., "SU-F-I-76: Fluoroscopic X-ray beam profiles for spectra incorporating copper filtration," Med Phys **43**, 3404 (2016).

21. Lin, P. J., "The operation logic of automatic dose control of fluoroscopy system in conjunction with spectral shaping filters," Med Phys **34**, 3169-3172 (2007).

22. Fajadet, J., Marco, J., Bertel, O., and Straumann, E., "Innovations in flat-detector cardiac angiography," Medicamundi **47**, 56-64 (2003).

23. Comparison chart: Angiography systems. Arlington Heights (IL): Diagnostic and Interventional Cardiology, Scranton Gillette Communications; 2014. Available from:

http://utilities.scrantongillette.com/email_images/pulloutchart_digimag_daic0914.pdf. Accessed September 10, 2015.

24. Miller, D. L., "Overview of contemporary interventional fluoroscopy procedures," Health Phys **95**, 638-644 (2008).

25. American Association of Physicists in Medicine, *Functionality and Operation of Fluoroscopic Automatic Brightness Control/Automatic Dose Rate Control Logic in Modern Cardiovascular and Interventional Angiography Systems* (American Association of Physicists in Medicine, College Park, 2012).

26. Rauch, P., Lin, P. J., Balter, S., Fukuda, A., Goode, A. Hartwell, G., LaFrance, T., Nickoloff, E., Shepard, J., and Strauss, K., "Functionality and operation of fluoroscopic automatic brightness control/automatic dose rate control logic in modern cardiovascular and interventional angiography systems: a report of Task Group 125 Radiography/Fluoroscopy Subcommittee, Imaging Physics Committee, Science Council," Med Phys **39**, 2826-2828 (2012).

27. International Electrotechnical Commission, "Medical electrical equipment - Part 2-43: particular requirements for the basic safety and essential performance of X-ray equipment for interventional procedures," IEC 60601-2-43:2010 (2010).

28. Jones, A. K. and Pasciak, A. S., "Calculating the peak skin dose resulting from fluoroscopically guided interventions. Part I: methods," J Appl Clin Med Phys **12**, 3670 (2011).

29. National Council on Radiation Protection and Measurements, *Report No. 168 - Radiation Dose Management for Fluoroscopically-Guided Interventional Medical Procedures* (NCRP, Bethesda, 2011).

30. International Commission on Radiation Units and Measurements, *Patient Dosimetry for X Rays Used in Medical Imaging (Report 74)* (ICRU, Bethesda, 2006).

31. Malusek, A., Larsson, J. P., and Carlsson, G. A., "Monte Carlo study of the dependence of the KAP-meter calibration coefficient on beam aperture, x-ray tube voltage and reference plane," Phys Med Biol **52**, 1157-1170 (2007).

32. Larsson, J. P., Persliden, J., and Carlsson, G. A., "Ionization chambers for measuring air kerma integrated over beam area. Deviations in calibration values using simplified calibration methods," Phys Med Biol **43**, 599-607 (1998).

33. Toroi, P., Komppa, T., and Kosunen, A., "A tandem calibration method for kerma-area product meters," Phys Med Biol **53**, 4941-4958 (2008).

34. Toroi, P., Komppa, T., Kosunen, A., and Tapiovaara, M., "Effects of radiation quality on the calibration of kerma-area product meters in x-ray beams," Phys Med Biol **53**, 5207-5221 (2008).

35. Lin, P. J., Schueler, B. A., Balter, S., Strauss, K. J., Wunderle, K. A., LaFrance, M. T., Kim, D. S., Behrman, R. H., Shepard, S. J., and Bercha, I. H., "Accuracy and calibration of integrated radiation output indicators in diagnostic radiology: a report of the AAPM Imaging Physics Committee Task Group 190," Med Phys **42**, 6815-6829 (2015).

36. Ragozzino, M. W., Gray, J. E., Burke, T. M., and Van Lysel, M. S., "Estimation and minimization of fetal absorbed dose: data from common radiographic examinations," AJR Am J Roentgenol **137**, 667-671 (1981).

37. Johns, H. E. and Cunningham, J. R., *The Physics of Radiology, Fourth Edition* (Charles C Thomas, Springfield, 1983).

38. Wagner, L. K., Lester, R. G., and Saldana, L. R., *Exposure of the Pregnant Patient to Diagnostic Radiations: A Guide to Medical Management* (Medical Physics Publishing, Madison, 1997).

39. Cohen, M., Jones, D. E. A., and Greene, D., eds., "Central axis depth dose data for use in radiotherapy," Br J Radiol supplement 11 (1972).

40. Fetterly, K. A., Gerbi, B. J., Alaei, P., and Geise, R. A., "Measurement of the dose deposition characteristics of x-ray fluoroscopy beams in water," Med Phys **28**, 205-209 (2001).

41. Food and Drug Administration, "Code of Federal Regulations Title 21" (April 2016).

42. Mathieu, K. B., Kappadath, S. C., White, R. A., Atkinson, E. N., and Cody, D. D., "An empirical model of diagnostic x-ray attenuation under narrow-beam geometry," Med Phys **38**, 4546-4555 (2011).

43. Li, X. A., Ma, C. M., and Salhani, D., "Measurement of percentage depth dose and lateral beam profile for kilovoltage x-ray therapy beams," Phys Med Biol **42**, 2561-2568 (1997).

44. Harrison, R. M., "Central-axis depth-dose data for diagnostic radiology," Phys Med Biol **26**, 657-670 (1981).

45. Petoussi-Henss, N., Zankl, M., Drexler, G., Panzer, W., and Regulla, D., "Calculation of backscatter factors for diagnostic radiology using Monte Carlo methods," Phys Med Biol **43**, 2237-2250 (1998).

46. Benmakhlouf, H., Bouchard, H., Fransson, A., and Andreo, P., "Backscatter factors and mass energy-absorption coefficient ratios for diagnostic radiology dosimetry," Phys Med Biol **56**, 7179-7204 (2011).

47. Harrison, R. M., "Backscatter factors for diagnostic radiology (1-4 mm Al HVL)," Phys Med Biol **27**, 1465-1474 (1982).

48. International Commission on Radiation Units and Measurements, *Tissue Substitutes in Radiation Dosimetry and Measurement, ICRU Report 44* (ICRU, Bethesda, 1989).

49. Lee, C., Lodwick, D., Hurtado, J., Pafundi, D., Williams, J. L., and Bolch, W. E., "The UF family of reference hybrid phantoms for computational radiation dosimetry," Phys Med Biol **55**, 339-363 (2010).

ABSTRACT

X-RAY BEAM CHARACTERISTICS AND RADIATION DOSE DEPOSITION TO SOFT TISSUE FROM FLUOROSCOPIC X-RAY BEAMS INCORPORATING COPPER FILTRATION

by

KEVIN A. WUNDERLE

December 2016

Co-Advisor: Dr. Frank F. Dong

Co-Advisor: Dr. Otto Muzic

Major: Medical Physics

Degree: Doctor of Philosophy

Purpose: This work investigated several topics related to dosimetry in soft tissue from fluoroscopic X-ray beams; first, it investigated the X-ray beam spectra and air kerma rates available for clinical use on state-of-the-art fluoroscopes using spectral (copper [Cu]) filtration; second, it investigated the fluoroscopic X-ray beam characteristics of first half-value layer (HVL), second HVL, homogeneity coefficients (HCs), and backscatter factors (BSFs) across the full range of available beam qualities; and third, it investigated the energy dependence of kerma-area-product (KAP)-meters measuring the radiation output of the fluoroscope. **Materials and Methods:** A state-of-the-art Siemens Artis Zee fluoroscope was operated in the service mode to allow for manual control of the technique factors (kVp, mA, ms, and Cu). Free-in-air measurements were made to determine HVLs and KAP-meter accuracy. BSFs were determined across a large range of X-ray field sizes and beam spectra with polymethyl-methacrylate. Percent depth doses (PDDs) and X-ray beam profiles were acquired across a similar range of X-ray beam spectra using a PTW water tank and a Spokas ionization chamber for the PDD measurements and a solid state dosimeter for the beam profile measurements. **Results:** Fluoroscopic dose rate and technique parameter curves are reported for several state-of-the-art fluoroscopes, illustrating differences in approach among vendors and establishing the basis for investigation of the X-ray beam characteristics (HVLs, HCs, BSFs, and PDDs). These X-ray beam characteristics are reported across a large range of clinically available X-ray beam spectra, providing the necessary foundation for dosimetry in soft tissue from these beams. Additionally, the accuracy of the displayed $K_{a,r}$ and correction coefficients determined using the American Association of Physicists in Medicine Task Group 190 methodology is reported across a similar range of X-ray beam spectra. **Conclusion:** The content of this research provides the necessary foundation for determining radiation dose at depth in soft tissue from state-of-the-art fluoroscopes. The results from this research can be used to assess dose at depth in soft tissue from fluoroscopically guided interventions, to determine fetal dosimetry from fluoroscopically guided interventions, and to validate dose modeling software.

AUTOBIOGRAPHICAL STATEMENT

KEVIN A. WUNDERLE

EDUCATION

2006 **MSc Physics, Cleveland State University, Cleveland, OH**
Graduated Magna Cum Laude
2003 **BA Physics, Cleveland State University, Cleveland, OH**
Graduated Cum Laude
1997 **BA Psychology, Cleveland State University, Cleveland, OH**
Graduated Cum Laude

PROFESSIONAL CREDENTIALS

2015 **Licensed Diagnostic Radiological Physicist**
State of Florida, License # DRP 149
2012 **Adjunct Faculty Appointment**
Cleveland State University – Department of Physics
2010 **Diplomat of the American Board of Radiology**
ABR board certification in Diagnostic Radiologic Physics
2007 **Certified Radiation Expert**
State of Ohio, CRE # 243

AWARDS & COMMITTEE APPOINTMENTS

2016 AAPM Committee Vice Chair – AAPM Radiography and Fluoroscopy Sub-Committee; member since 2011
2014 AAPM Committee Member – Medical Physics Education of Physicians
2012 AAPM Task Group 190 Member (report published in Med Phys 2015)

PUBLICATIONS

Wunderle, K. A., Rakowski, J. T., and Dong, F. F., “Effect of fluoroscopic X-ray beam spectrum on air-kerma…,” J Appl Clin Med Phys **17**, 467-474 (2016)

Wunderle, K. A., Rakowski, J. T., and Dong, F. F., “Approaches to interventional fluoroscopic dose curves,” J Appl Clin Med Phys **17**, 5788 (2016)

Lin, P. J., Schueler, B. A., Balter, S., Strauss, K. J., **Wunderle, K. A.**, et al, “Accuracy and calibration of integrated radiation output …,” Med Phys **42**, 6815-6829 (2015)

Wunderle, K. A. and Gill, A. S., “Radiation-related injuries and their management: an update,” Semin Intervent Radiol **32**, 156-162 (2015)

Wunderle, K. A. and Sands, M. J., “Radiation recall after a …,” J Vasc Interv Radiol **25**, 1027-1028 (2014)

Panuccio, G., Greenberg, R. K., **Wunderle, K.**, et al, “Comparison of indirect radiation dose estimates …,” J Vasc Surg **53**, 885-894 (2011)